Investigating future galaxy surveys of cosmological large-scale structure

by

Setareh Foroozan

A thesis
presented to the University of Waterloo
in fulfillment of the
thesis requirement for the degree of
Master of Science
in
Physics

Waterloo, Ontario, Canada, 2022

Author's Declaration

This thesis consists of material all of which I authored or co-authored: see Statement of Contributions included in the thesis. This is a true copy of the thesis, including any required final revisions, as accepted by my examiners.

I understand that my thesis may be made electronically available to the public.

Statement of contributions

This thesis consists in part of two manuscripts written for publication [1, 2]. Exceptions to sole authorship of material are as follows:

Research presented
in Chapters 2:

Dr. Alex Krolowski
Department of Physics and Astronomy, University of Waterloo
Waterloo Centre for Astrophysics, University of Waterloo
Perimeter Institute for Theoretical Physics

Prof. Will Percival
Department of Physics and Astronomy, University of Waterloo
Waterloo Centre for Astrophysics, University of Waterloo
Perimeter Institute for Theoretical Physics

Research presented
in Chapters 3:

Dr. Elena Massara
Department of Physics and Astronomy, University of Waterloo
Waterloo Centre for Astrophysics, University of Waterloo

Prof. Will Percival
Department of Physics and Astronomy, University of Waterloo
Waterloo Centre for Astrophysics, University of Waterloo
Perimeter Institute for Theoretical Physics

Abstract

My thesis consists of the two following projects:

Testing Large-Scale Structure Measurements against Fisher Matrix Analysis [2] **(Chapter 2):** We compare Baryonic Acoustic Oscillation (BAO) and Redshift Space Distortion (RSD) measurements from recent galaxy surveys with their Fisher matrix based predictions. Measurements of the position of the BAO signal lead to constraints on the comoving angular diameter distance D_M and the Hubble distance D_H that agree well with their Fisher matrix based expectations. However, RSD-based measurements of the growth rate $f\sigma_8$ do not agree with the predictions made before the surveys were undertaken, even when repeating those predictions using the actual survey parameters. We show that this is due to a combination of effects including degeneracies with the geometric parameters D_M and D_H, and optimistic assumptions about the scale to which the linear signal can be extracted. We show that measurements using current data and large-scale modelling techniques extract an equivalent amount of signal to that in the linear regime for $k = 0.08\,h\,\mathrm{Mpc}^{-1}$, remarkably independent of the sample properties and redshifts covered.

Correcting for small-displacement interlopers in BAO analyses [1] **(Chapter 3):** Due to the low resolution of slitless spectroscopy, future surveys including those made possible by the Roman and Euclid space telescopes will be prone to line misidentification, leading to interloper galaxies at the wrong redshifts in the large-scale structure catalogues. The most pernicious of these have a small displacement between true and false redshift such that the interloper positions are correlated with the target galaxies. We consider how to correct for such contaminants, focusing on Hβ interlopers in $[O\,ii]$ catalogues as will be observed by Roman, which are misplaced by $\Delta d = 97\,h\,\mathrm{Mpc}^{-1}$ at redshift $z = 1$. Because this displacement is close to the BAO scale, the peak in the interloper-target galaxy cross-correlation function at the displacement scale can change the shape of the BAO peak in the auto-correlation of the contaminated catalog, and lead to incorrect cosmological measurements if not accounted for properly. We consider how to build a model for the monopole and quadrupole moments of the contaminated correlation function, including an additional free parameter for the fraction of interlopers. The key input to this model is the cross-correlation between the population of galaxies forming the interlopers and the main target sample. It will be important to either estimate this using calibration data or to use the contaminated small-scale auto-correlation function to model it, which may be possible if a number of requirements about the galaxy populations are met. We find that this method is successful in measuring the BAO dilation parameters without significant degradation in accuracy provided the cross-correlation function is accurately known.

Acknowledgements

First and foremost, I would like to thank my supervisor, Prof. Will Percival for his continuous invaluable advice and support. Many thanks to the help and collaboration of Dr. Alex Krolewski and Dr. Elena Massara. I also thank Prof. Mike Hudson and Dr. Dustin Lang for agreeing to be on my committee and for their useful discussions.

I would like to thank Mariana Vargas Magana and Richard Neveux for providing the covariance matrices for eBOSS Quasars, and Chris Blake, Hector Gil-Marín, and Yun Wang for thoughtful comments and useful discussions. Special acknowledgment to Yuting Wang who provided code and results for eBOSS Quasar DR14 for comparison to our results. This research made use of the PYTHON packages NUMPY ([3]), SCIPY ([4]), MATPLOTLIB ([5]), COLOSSUS ([6]), and ASTROPY ([7]). This research was enabled in part by support provided by Compute Ontario (www.computeontario.ca) Compute Canada (www.computecanada.ca), and the Digital Research Alliance of Canada (alliancecan.ca). Research at Perimeter Institute is supported in part by the Government of Canada through the Department of Innovation, Science and Economic Development Canada and by the Province of Ontario through the Ministry of Colleges and Universities.

Table of Contents

List of Figures

List of Tables

Chapter 1

Introduction to large-scale structure and galaxy clustering

It was not long ago when Edwin Hubble first discovered that Andromeda did not belong to Milky Way; instead, it was a galaxy on its own – or, as he would call it, an "extragalactic nebula" – residing outside our galaxy. Soon after, he discovered that many other "nebulae" were also galaxies of their own and, even more surprisingly, by detailing the redshift-distance relation he confirmed Vesto Slipher's discovery that nearly all of them appeared to be moving away from us. This discovery led to astronomers believing that the Universe as a whole is expanding. This phenomenon is now known as the Hubble expansion of the Universe.

Subsequently, astronomers started using Doppler shifts to measure the rotational velocity of nearby galaxies. To their surprise, they found that the rotation curves of the spiral galaxies are flat, implying that the matter enclosed within them was an order of magnitude higher than the estimated total mass of the stars. Initially, *Dark Matter* (DM) was introduced to address the flat rotation curve problem. However, eventually, it turned out to address many other problems if it was assigned the right properties. Later on, there was found an increasing number of evidence supporting that the expanding universe is accelerating (i.e., [8, 9, 10]). This was a remarkable discovery since it is not in accordance with what General Relativity (GR) expects. To solve this discrepancy, a number of possibilities have been studied. One of the solutions is to add another substance to the known constituents of the universe, which is named *Dark Energy*.

While with the growing precision of observations, we have been able to constrain some properties of dark matter and energy, to this day, their nature remains a secret. For instance, there is strong evidence that the observed structures in the Universe can not be explained by *hot* dark matter, which rules out the hot dark matter theory ([11, 12]). Therefore, it is now commonly assumed that dark matter is cold (CDM). Moreover, a dark energy model with a constant density, known as cosmological constant, or Λ as first introduced by Einstein to allow a stationary model of the Universe ([13]), would justify several independent measurements, such as supernovae type-Ia observations ([14]) and BAO signal in early and late Universe (will be further described in Section 1.4).

A Universe made of cosmological constant, cold dark matter, baryonic matter, radiation, neutrinos, and curvature is known as a ΛCDM universe. In fact, many well cross-checked observations make ΛCDM a convincing empirical model of our Universe. Based on this, throughout this work, I assume ΛCDM cosmologies with slightly different properties, depending on the observation being referred to. Additionally, our Universe as a whole can be assumed to be homogeneous and isotropic on large scales. Indeed, on smaller scales, solely the existence of galaxies contradicts the validity of this approximation. However, when averaged over large scales, homogeneity and isotropy are valid assumptions and are compatible with the observations.

In the following sections, we study the fundamentals of Large-Scale Structure (LSS) that will be used frequently in Chapter 2 and 3.

1.1 Past and future galaxy surveys

The quest to understand Dark Energy, the physical mechanism behind observations of the accelerating expansion of the Universe, has led to a plethora of ongoing and future experiments, including the Dark Energy Spectroscopic Instrument (DESI, [15]), the Rubin Observatory and LSST survey [16], and the Euclid [17] and WFIRST (now known as Nancy Grace Roman Space Telescope) [18] satellite missions. Many of these are designed to use the Baryon Acoustic Oscillation (BAO), and Redshift-Space Distortion (RSD) signals within the clustering of galaxies to constrain the geometry of the Universe and growth of structure within it.

Over the past two decades, since the early signs of the baryon acoustic oscillations were seen in the 2-degree Field Galaxy Redshift Survey (2dFGRS, [19]) and the BAO signal was refined using the Sloan Digital Sky Survey-II (SDSS, [20]) Luminous Red Galaxy (LRG) sample [21] and the final release of data from the 2dFGRS [22], ground based surveys have been undertaken to make BAO and RSD measurements to ever higher precision. The combination of 2dFGRS and the final SDSS-II LRG data reached a detection threshold of 3.6σ [23], which was rapidly overtaken by early data from the Baryon Oscillation Spectroscopic Survey (BOSS, [24]), which breached the 5σ detection threshold. Since then, the BAO technique has become one of the pillars of modern cosmology, with particularly important surveys undertaken within the SDSS. At low redshift, we have the Main Galaxy Sample (MGS, [25]) using data from SDSS-I&II ([26]), while at higher redshift we have the SDSS-III ([27]) BOSS, [28] and the SDSS-IV ([29]) extended Baryon Oscillation Spectroscopic Survey (eBOSS, [30]). In addition, complementary measurements were made by the 6-degree Field Galaxy Survey (6dFGS, [31]) at low redshift, and the WiggleZ Dark Energy Survey (WiggleZ, [32]) at high redshift. All have released measurements at various stages of survey progress.

The observed BAO and RSD signals from these surveys have been analyzed by different groups with slightly different techniques in both configuration and Fourier space. These measurements constrain the anisotropic distance scales, D_M and D_H, the isotropic distance scale, D_V, and the logarithmic growth rate of structure, f. The Fisher matrix formalism has allowed cosmologists to predict the constraining power of surveys on these parameters and therefore plan for the future [33, 34, 35, 36]. This formalism was first introduced to estimate the error on model parameters in any given dataset [37], by assuming that the inverse of the Fisher matrix can be interpreted as an estimation of the covariance matrix for a Gaussian likelihood. Moreover, the Cramér-Rao inequality states that the diagonal elements of the inverse of the Fisher matrix give a lower bound on the variance of any unbiased estimator of the model parameters, in other words, the best possible errors.

Thus, validating the Fisher matrix predictions made for past surveys is important to test whether survey goals were met and particularly to test the optimality of the analysis techniques used to evaluate the cosmological parameters. For instance, in a recent study by Ruggeri et al. [38], the errors in BAO survey measurements, mocks, and Fisher matrix were compared without applying reconstruction to the density field for six galaxy surveys, finding good agreement. We find similar results in Chapter 2 for the same surveys and datasets analysed in the same way, but extend this analysis to consider further data: BAO with reconstruction and RSD measurements.

Observational instruments make use of different spectroscopy techniques based on their target. For instance, one type of spectroscopy is called long-slit spectroscopy, in which a slit is located at the telescope's focal plane to focus solely on one target and prevent any background light from entering the spectrograph. While this method gives very high S/N, it is not efficient for galaxy redshift surveys, as they aim to observe millions of objects. There is a solution to this issue: removing the slit. By doing so and adding a grism (grating and prism), slitless spectroscopy enables us to measure the spectra of multiple objects simultaneously, at the cost of decreased S/N, and sometimes, overlapped spectra of some objects. Nonetheless, grism slitless spectroscopy will be used for future, and ongoing space-based telescopes, such as James Webb Space Telescope [39], Euclid, and Roman Space Telescope. An example of the output of slitless spectroscopy is illustrated in Figure 1.1. This figure is not from actual observations but is simulated by [40] and shown here to compare a photometry image (on the left) and its corresponding slitless spectroscopy image (on the right). You can see how all objects are dispersed into their spectra, with some of them overlapping.

Another example of a multi-object spectrograph is a fiber-fed spectrograph, in which fibers are directed towards the position of each target. The light from each target enters its assigned fiber at the focal plane, and the spectrograph collects light emitted from the other end of the fibers. For illustration, one petal of the DESI instrument with 502 robotic fibers is shown in Figure 1.2. Fiber-fed systems are able to cover large fields and provide uniform wavelength coverage. Moreover, higher resolution and non-overlapping individual spectroscopy make them less prone to line misidentifications. On the downside, fibers can not move far since they are physically limited between other fibers, limiting the angular separation range they can observe. These systems are typically harder to set up on space-based telescopes compared to a slitless spectrograph. Some examples of the ground-based LSS surveys that make use of fiber-fed instruments are: past SDSS survey with ≈ 600 fibers [41], and future DESI [42].

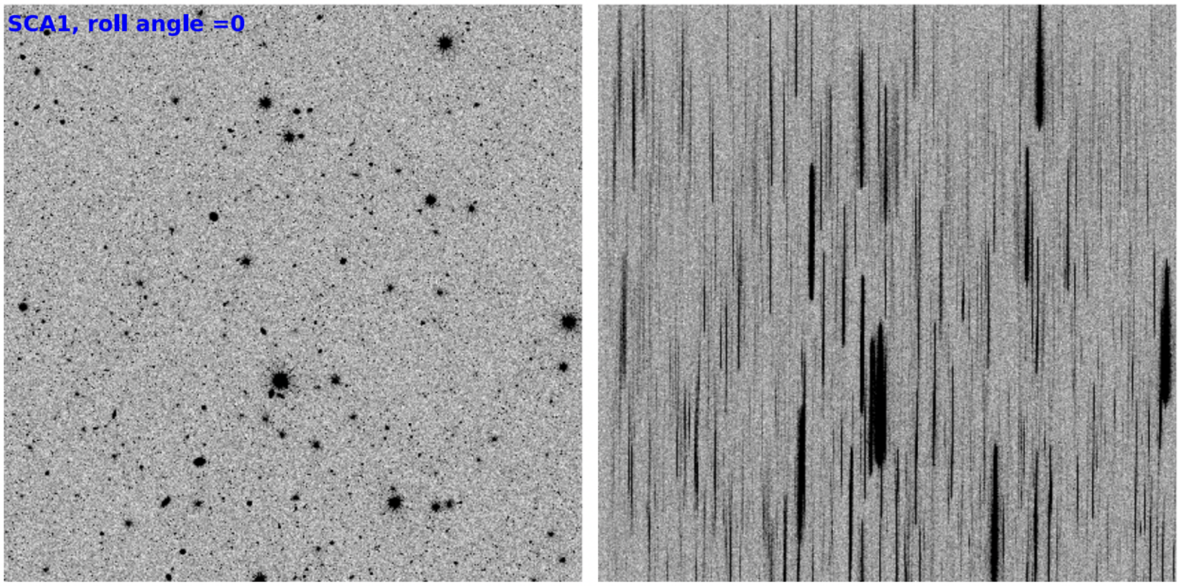

Figure 1.1: This figure is adopted from Fig. 8 of [40]. It displays a simulated example of a direct image on the left and a 2D slitless dispersed image on the right.

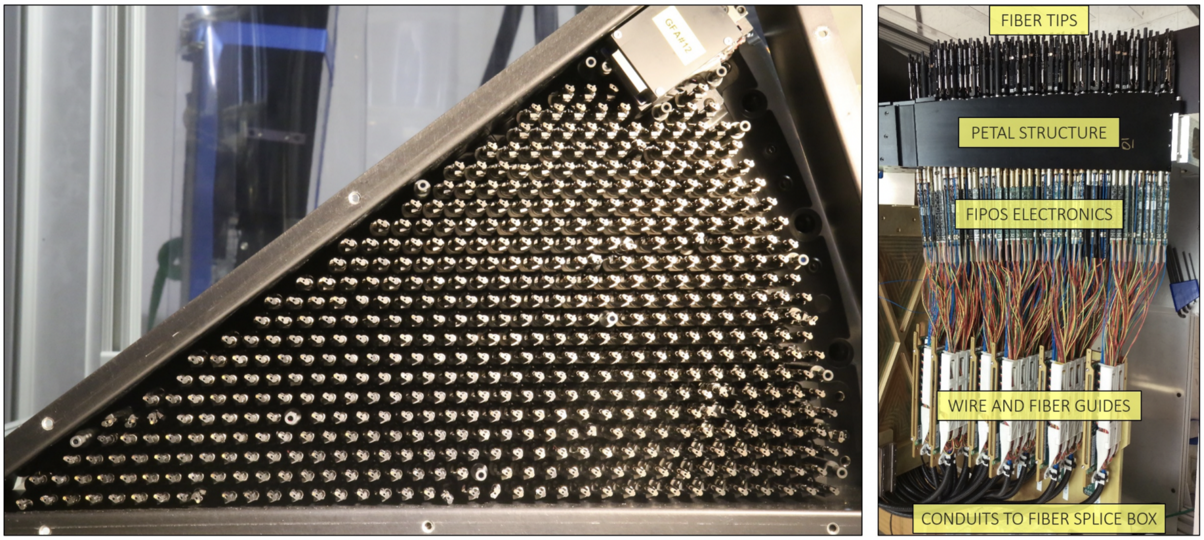

Figure 1.2: Adopted from Figure 1 of [42]. The left panel shows a petal with 502 robotic fibers as viewed from the front, and the right panel shows it as viewed from the side.

1.2 Measuring redshifts and distances

The Hubble expansion of the universe causes galaxies outside our local cluster to move away from us. Hubble empirically discovered that there is a linear relationship between the distance of the galaxies, r, and the radial velocity at which they are receding:

$$v_{\mathrm{H,r}} = cz_{\mathrm{H}} = H_0 r \,, \tag{1.1}$$

where $v_{\mathrm{H,r}}$ is the Hubble radial velocity, z_{H} is redshift due to Hubble expansion, and H_0 is the Hubble constant. We have used the small-speed approximation ($v/c \ll 1$) of the redshift-velocity relation for the first equality. Nowadays, all the early and late time observations have proven that the Hubble constant is around $\approx 70\,\mathrm{km\,s^{-1}\,Mpc^{-1}}$, despite the relatively small Hubble tension discrepancy, which is not the topic of this work. (see [43, 44, 45, 46]). One can find the theoretical relation between the distance and redshift of galaxies by manipulating the Friedmann-Robertson-Walker (FRW) metric,

$$r = \int_0^z \frac{cdz'}{H(z')} \,, \tag{1.2}$$

which simplifies to Eq. 1.1 for small separations and redshifts.

We can build a 3d map of the galaxies by directly measuring their two transverse angular coordinates across the LOS by photometry and indirectly measuring their radial coordinate by translating the measured redshift from spectroscopy to distance using Eq. 1.2. In practice, this translation is not as simple as it looks due to the peculiar velocities of galaxies caused by the gravitational field of DM and other galaxies in their vicinity. The observed redshift of a galaxy measures the super-position of the cosmic Hubble expansion velocity *and* the LOS peculiar velocity of the galaxy: $v_r = v_{H,r} + v_{pec,r}$. Therefore, the final observed redshift can be written as

$$cz = H_0 r + v_{\mathrm{pec,r}} \,. \tag{1.3}$$

For most galaxies, unless there is a different way of measuring distance, only the redshift is measurable, not the true distance r. Thus, cosmologists usually describe the position of an object in the *redshift space* using the following coordinates: s_1 and s_2, the angular positions across the LOS, which are not affected by peculiar velocities, and s_3 the *redshift distance* along the LOS:

$$s_3 = \frac{cz}{H_0} = r + \frac{v_r}{H_0} \,. \tag{1.4}$$

Measuring the LSS coordinates in redshift-space rather than configuration-space causes an anisotropic observational effect called Redshift-Space-Distortion (RSD), which will frequently appear in the text. In Figure 1.3, we demonstrate how configuration space translates into redshift space and how peculiar velocities cause redshift space distortions:

- Top panel: Galaxies G1 and G2 are on the opposite sides but at the same (large-scale) distance from the center of an overdense region. The center of the over-dense region and galaxies are aligned with the LOS. Due to the gravitational attraction, both galaxies move towards the center of the overdensity. This means that G2 will have a redshift distance s_3 that is larger than its true distance r, and G1 has a s_3 smaller than its r. Now consider galaxies that are located to the right and left of the center of overdensity. Since their peculiar velocity is mainly across the LOS, their s_3 would be equal to their r, so unaffected by the redshift space translation. By extending this logic, a sphere in configuration space centered at the center of an overdensity would appear as an oblate ellipsoid, squashed along the LOS in redshift space.

- Middle panel: Galaxies closer to the center have larger peculiar velocities than ones farther away. At the turnaround scale, the peculiar velocity redshift is equal to the Hubble redshift, canceling out so that a sphere in configuration space would appear as a line.

- Bottom panel: Now consider the same scenario, but at such small scales so that the peculiar velocities are large enough to make the galaxies appear on the opposite side of the overdense region. This will, in effect, appear as an elongated ellipsoidal along the LOS.

The large-scale RSD is called the Kaiser effect [48] and is relatively easy to model using the Kaiser equation. The small-scale RSD effect will cause the isotropic sphere shells in configuration space to look like fingerprints in redshift space, therefore known as Finger-of-God (hereafter, FoG) effect, illustrated in Figure 1.4. Unfortunately, FoG is harder to model due to its nonlinear nature, but we will touch on that later when we introduce the two-point statistics in the next section.

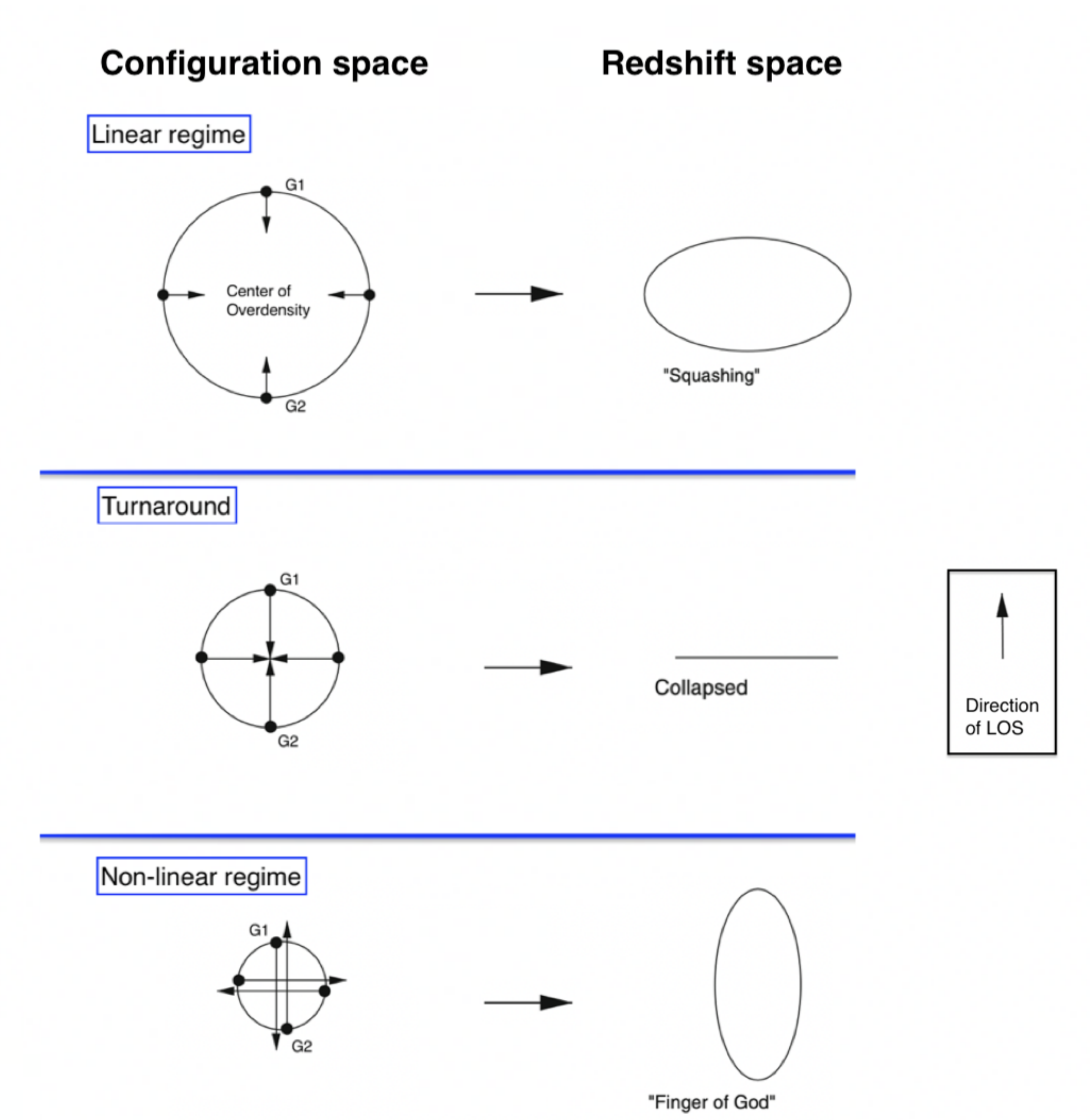

Figure 1.3: Illustrating redshift-space-distortions. On the left, we show imaginary spherical shells with different radii, centered at the overdensity peak. Arrows show the peculiar velocities of the galaxies that would be placed on these spheres. On the right, the interpreted redshift space positions are shown. The distortion is dependent on the scale. Source: Fig. 2 of [47] with some changes.

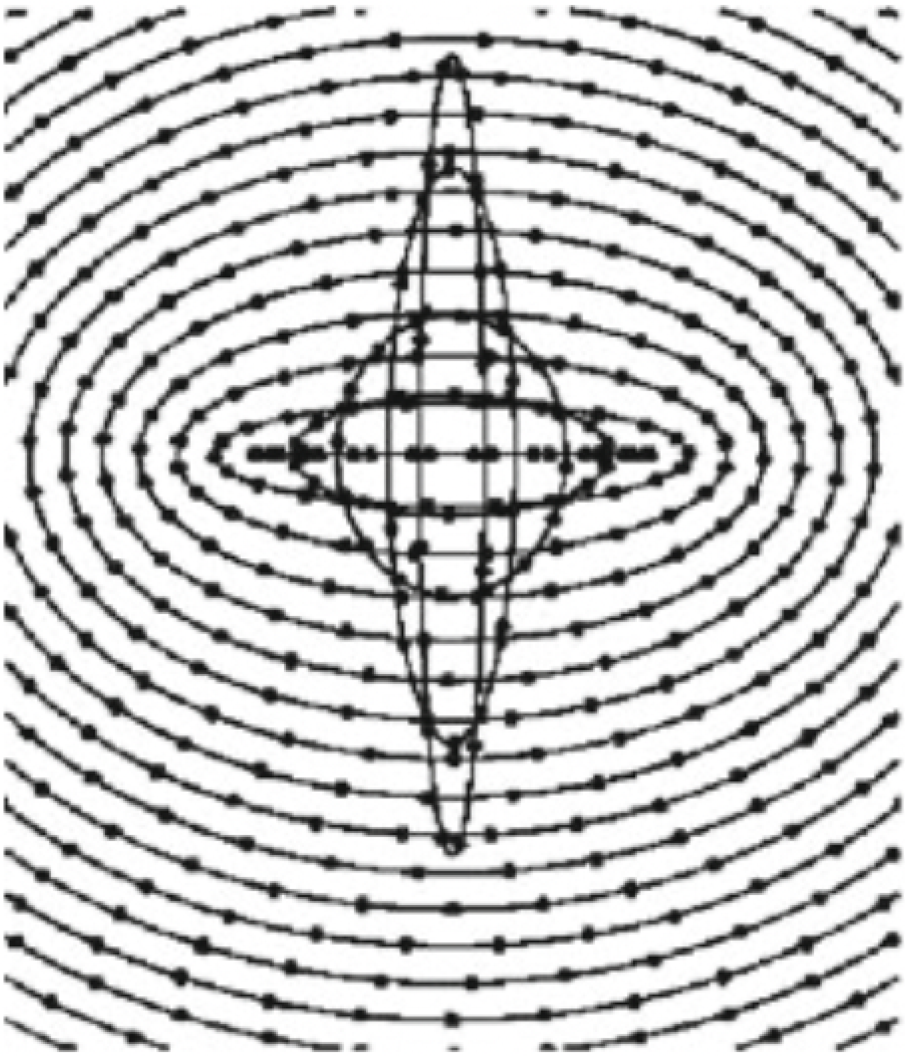

Figure 1.4: This figure depicts the positions of galaxies in redshift space with black points. This effect is called Finger-of-God. In configuration space, galaxies that are connected by ellipsoidal curves have the same distance to the center of the overdensity. Source: Fig. 1 of [47] with minor changes.

1.3 Correlation function and power spectrum

The Universe is isotropic and homogeneous on large scales, and it can be well described by the ΛCDM model. However, it behaves differently on small scales: it becomes anisotropic and inhomogeneous, and the deviations from homogeneity tend to grow over time, or else there would not be any galaxies or stars. The important question is, how did these fluctuations form in the first place? "Inflation" is proven to be a plausible theory that can answer this question. There are several inflationary models that differ in detail, but they all describe possible scenarios in which the random *Gaussian* fluctuations were seeded in the density field during the very early epochs of the Universe. These fluctuations later grew and today are seen as galaxy structures.

We can quantify these fluctuations from perfect homogeneity by defining over-density

$$\delta_{\mathrm{m}}(\vec{x}) = \frac{\bar{\rho} - \rho(\vec{x})}{\bar{\rho}}\,, \tag{1.5}$$

where $\bar{\rho}$ is the mean density, and $\rho(\vec{x})$ is the local density of matter at comoving distance $\vec{x}$. The two-point correlation function of the over-density field is used to describe the correlation between the over-density at co-moving distance $\vec{x}$ and $\vec{y}$

$$\xi_{\mathrm{m}}(\vec{x}, \vec{y}) = \langle \delta_{\mathrm{m}}(\vec{x}) \delta_{\mathrm{m}}(\vec{y}) \rangle\,. \tag{1.6}$$

In general, knowing the two-point statistics is not sufficient to characterize a random field. However, a *Gaussian* random field can be described entirely by its two-point statistics, i.e., correlation function and power spectrum. Fortunately, in cosmology (it is believed that) the density field at early epochs obeyed a Gaussian distribution, which means that two-point statistics *do* suffice to exploit all the available information. Higher n-point statistics may be used in the late-time universe, but they are more challenging to measure, and in the scope of this thesis and the corresponding measurements, 2-point is adequate to describe the clustering.

Under the assumption of isotropy, ξ is simply a function of the separation between these two points, $r = |\vec{x} - \vec{y}|$: thus $\xi = \xi(r)$. Now the question is, how can we measure this correlation function when most of the matter is dark? Even with the baryonic matter, calculating the correlation function with Eq. 1.6 can be extremely time-consuming. The answer is that we can still have an estimation of it by using different "tracers" of the matter field and by using "estimators" of the correlation functions. Unfortunately, galaxies (as well as dark matter halos) are biased tracers of the matter field. But on the bright side, we can model the bias on linear scales, where a linear bias factor relates the over-density of the matter field and the galaxy over-density, $\delta_g = b_g\delta_m$. Thus,

$$\xi_g = b_g^2\xi_m \,. \tag{1.7}$$

There are nonlinear bias analyses based on perturbation theory, but those are outside the scope of this thesis. For more detail see Refs. [49, 50, 51].

Estimating this correlation function from a galaxy survey is a non-trivial task that had been studied for decades (refs [52, 53, 54]). One way to do this is to see the correlation function as the excess probability of finding two galaxies at a given separation compared to a random catalogue in which galaxies are uniformly distributed. There is a number of estimators that use this method to estimate the correlation function. In the following studies in Chapter 2, and 3, we use the Landy-Szalay estimator [54] given by

$$\hat{\xi}(r) = \frac{DD - 2DR + RR}{RR} \,, \tag{1.8}$$

where DD, DR, and RR are the data-data data-random and random-random pair counts.

The correlation function and power spectrum are two sides of the same coin, only the power spectrum describes the clustering in Fourier space rather than the configuration space. The two are related through a Fourier transform:

$$P(k) = \frac{1}{2\pi^2}\int_0^\infty x^2 \frac{\sin kx}{kx}\xi(x)dx \tag{1.9}$$

Even though these two usually have the same statistical properties and are convertible, sometimes it is easier to work with one rather than the other. In chapter 2, we will consider various BAO measurements. Some of these analyses constrained the cosmological parameters using configuration space analysis, whereas others preferred Fourier space. Regardless, we were able to compare the observational precision of these surveys to our Fisher analysis which was performed in the Fourier space. In chapter 3, performing the BAO analysis in real space was preferable since it made it easier to measure the correlation function of the objects directly from the Landy-Szalay estimator and model the measurements with the Fourier transform of the analytical CAMB power spectrum. We will come back to BAO in the next section.

In cosmology, one can project the power spectrum (or correlation function) onto the Legendre polynomials basis – the rest of this section is written for the power spectrum in

Fourier space, but $P(k)$ can be replaced by $\xi(r)$ to yield the same results in real space. Legendre polynomials are a system of complete and orthogonal basis defined as

$$L_l(x) = \frac{1}{2^l l!}\frac{d^l}{dx^l}(x^2-1)^l \,. \tag{1.10}$$

The Legendre moments of the power spectrum are given by the following integral

$$P_l(r) = \frac{(2l+1)}{2}\int_{-1}^{1} d\mu \; P(r,\mu)L_l(\mu)\,, \tag{1.11}$$

where r is the separation between two objects, μ is the cosine of the angle between $\vec{k}$ (or $\vec{r}$ in real space) and the LOS, and l is the order of the polynomial. Given that the Legendre polynomials are a set of complete and orthogonal axes, the two-point statistics can be reconstructed by summing over its moments:

$$P(r,\mu) = \sum_{l=0}^{\infty} P_l(r)L_l(\mu) \tag{1.12}$$

The zeroth moment is called the monopole, demonstrating an average over μ. The two-point statistic's odd moments vanish since their corresponding polynomials are odd functions. Higher even moments bring out the anisotropies and in-homogeneities of the two-point statistic caused by observational effects, i.e., typically Kaiser and FoG effects in redshift space, as well as the potential interloper effect, which we will study more in Chapter 3. The second and fourth moments are called quadrupole and hexadecapole, to which we will refer later in both works. The quadrupole and hexadecapole measurements are specifically essential in redshift-space since the correlation function in redshift-space is anisotropic, as mentioned in Section 1.2. In Figure 1.5, an example of the monopole and the quadrupole of the correlation function for the mean of 1000 Quijote mocks is shown. As seen at the bottom of this figure, quadrupole vanishes in configuration space but not in redshift space due to the anisotropy caused by RSD.

On linear scales, the configuration space power spectrum can be converted to redshift space using the Kaiser formula [48]:

$$P^s_{\rm gg}(\vec{r}) = (1 + \frac{f(z)}{b_g}\mu^2)^2 P^r_{\rm gg}(\vec{r})\,, \tag{1.13}$$

where superscript "r" and "s" indicate configuration and redshift space, respectively. Also, $f(z) = \Omega_m^{0.55}$ is the logarithmic derivative of the linear growth rate with respect to the scale factor, and b_g is the galaxy bias. In this formula, we have neglected the non-linear motion of galaxies at small scales. As far as the Kaiser effect is the main contributor to the anisotropy (large scales, $k\Sigma_s \ll 1$), the highest moment that needs to be taken into account in Eq. 1.12 is $l = 4$ since the Kaiser formula involves only terms up to μ^4, and the higher poles would vanish. This is why in the following chapters, we have not considered higher moments.

In the non-linear regime, however, the non-linear motions give rise to FoG. There have been many studies to model the non-linear RSD motions. Briefly, one can multiply the two-point statistics by a streaming factor for the FoG, some examples of which are

$$F(k, \mu, \Sigma_s) = \begin{cases} \frac{1}{(1+k^2\mu^2\Sigma^2)^2} & \text{Fiducial [55]} \\ \exp\left[-(k^2\mu^2\Sigma_s^2)/2\right] & \text{Gaussian [56]} \\ ... & \text{Other streaming models} \end{cases} \tag{1.14}$$

where Σ_s is the streaming scale. Other streaming models are commonly used too, which we will come back to in Chapter 2.

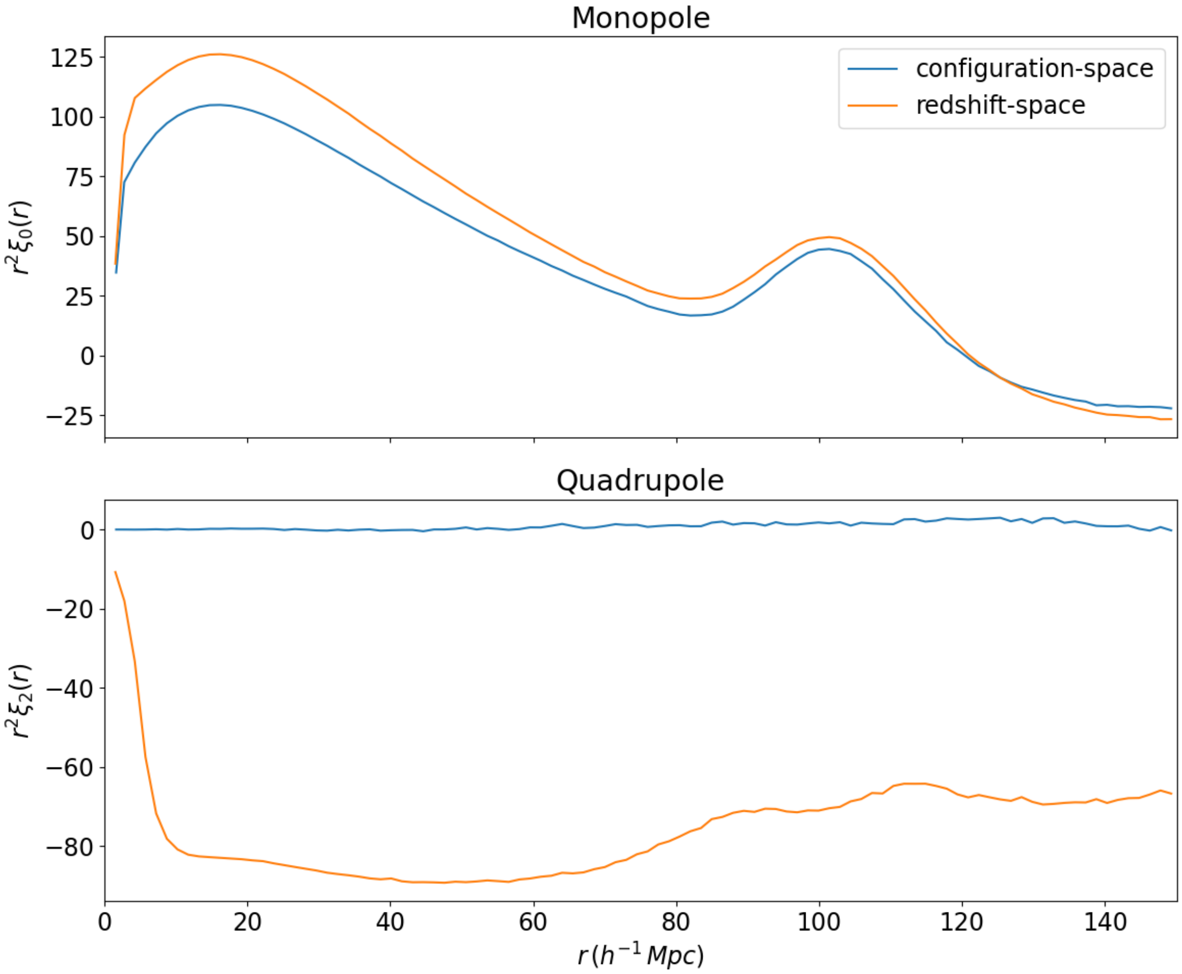

Figure 1.5: Measured monopole (top panel) and quadrupole (bottom panel) of the correlation function from the mean of 1000 Quijote simulations [57]. The configuration-space results are shown in blue and redshift-space are shown in orange. As can be seen, unlike redshift-space, the quadrupole vanished in configuration space, since the correlation function is isotropic in configuration space.

1.4 Measuring galaxy clustering and evolution using BAO and RSD techniques

Galaxy clustering and evolution can be understood by measuring the signal from Baryonic Acoustic Oscillations (BAO) and Redshift Space Distortions (RSD). In the following, we discuss the physics behind BAO and how, in practice, it is possible to extract information from the BAO signal.

The early universe had a density field with random Gaussian density fluctuations. Before the recombination of electrons and protons, baryons and photons had very strong interactions due to photons scattering off the electrons. Thus, they were coupled and made up a single fluid. The presence of photons added this strong pressure to the fluid, preventing it from falling into small potential perturbations caused by the post-inflation distribution of dark matter density. The pressure gradient in the photon-baryon fluid created waves that traveled with the speed of sound at the time, prior to recombination, when photons were still trapped and could not escape the fluid.

Electrons and protons eventually had to combine about $370,000$ years after the Big Bang ($z \approx 1100$) because the universe was expanding rapidly and cooling down to the temperature where forming neutral hydrogen atoms was energetically optimal. Soon after recombination, photons were free from Thompson scattering and could finally escape the baryonic matter fluid and left the baryons pressureless to fall into the gravitational potential wells of the combined gravity of dark matter and baryons. At this moment, the sound waves were frozen since they could no longer propagate. Thus, there was a maximum distance that the sound waves of the baryon-photon fluid could travel in a sphere centered at the initial density peak before they got frozen in, also known as the *comoving sound horizon at recombination* given by

$$r_s = \int_{\infty}^{z_{rec}} \frac{c_s dz}{H(z)}\,, \tag{1.15}$$

where c_s is the sound speed – this can be driven from Eq. 1.2 by changing the integral limits and replacing the speed of light with the speed of sound. This phenomenon is known as Baryonic Acoustic Oscillations (BAOs) and it has a characteristic length scale of r_s. By plugging in the baryon-to-photon and matter-to-radiation density ratios from observations into Eq. 1.15, one can find that $r_s = 100\,h^{-1}\,\mathrm{Mpc}$. Indeed, as we would expect, this scale has been measured in the CMB temperature map by Planck [58], and WMAP [59] collaborations.

Since baryons left an imprint of the BAO on the overall matter correlation function, we should be able to see this characteristic length scale at late times in the distribution of the galaxies as well. Remarkably, the BAO signal in the distribution of galaxies was first observed by 2dFGRS ([60, 22, 19]) and the SDSS ([61], [21]) collaborations. If galaxies were randomly distributed, we would not expect these measurements to detect the BAO signal. Instead, we would expect them to reveal a monotonically decreasing (power-law) trend in their correlation function – if galaxies were not clustered, the farther they were, the less they would be correlated. Indeed, as shown in the top panel of Figure 1.6, the general shape of the correlation function *does* roughly follow a power-law function. Nevertheless, due to this general decaying shape, the BAO feature is not visible in this picture. A better way to bring out and display the BAO scale is by multiplying $\xi(r)$ by r^2. As shown in the bottom panel of Figure 1.6, the BAO signal is evident in this picture. This is why in the following chapters, whenever we want to illustrate the correlation function, we plotted $r^2\xi(r)$ rather than $\xi(r)$ alone.

We talked about measuring the two-point statistics in the redshift space and decomposing it into multipoles. In the rest of this section, we will learn why correctly modeling RSD is not only useful for accurately modeling BAO, but also within RSD itself lies valuable information about the growth rate of structure. As we explained in the previous sections, in redshift space, due to the peculiar velocities of galaxies, the clustering signal is anisotropic and distorted along the LOS. We called this effect "redshift-space distortions". Since these distortions are related to the growth rate of structure, f in Eq. 1.13, the signal from RSD enables us to constrain f, and moreover, provides an important test for the ongoing debate on dark energy vs. modified gravity models. A number of LSS surveys have measured $f\sigma_8$ (σ_8 is the normalization of power spectrum) by measuring the RSD signal in the two point statistics of the galaxy clustering, i.e., 6dFGS [62], SDSS MGS [63], BOSS [64], eBOSS [65, 66], WiggleZ [67]. Each of these studies has made use of a different RSD model, trying to model non-linearities better than before. Regardless, the largest wavenumber from which each model is able to extract information is at best around $0.2\,h\,\mathrm{Mpc}^{-1}$ (see Table 2.2 of Chapter 2).

We will frequently make use of the BAO and RSD techniques in the following chapters:

- In Chapter 2, we use RSD analysis to constrain the growth rate of structure (see Section 2.1.2) and BAO analysis to constrain the dilation parameters (see Section 2.1.1).
- In Chapter 3, we study the effect of interlopers in the shape of the redshift-space correlation function around the BAO peak while also accounting for redshift space distortions in the model (see Section 3.4.3).

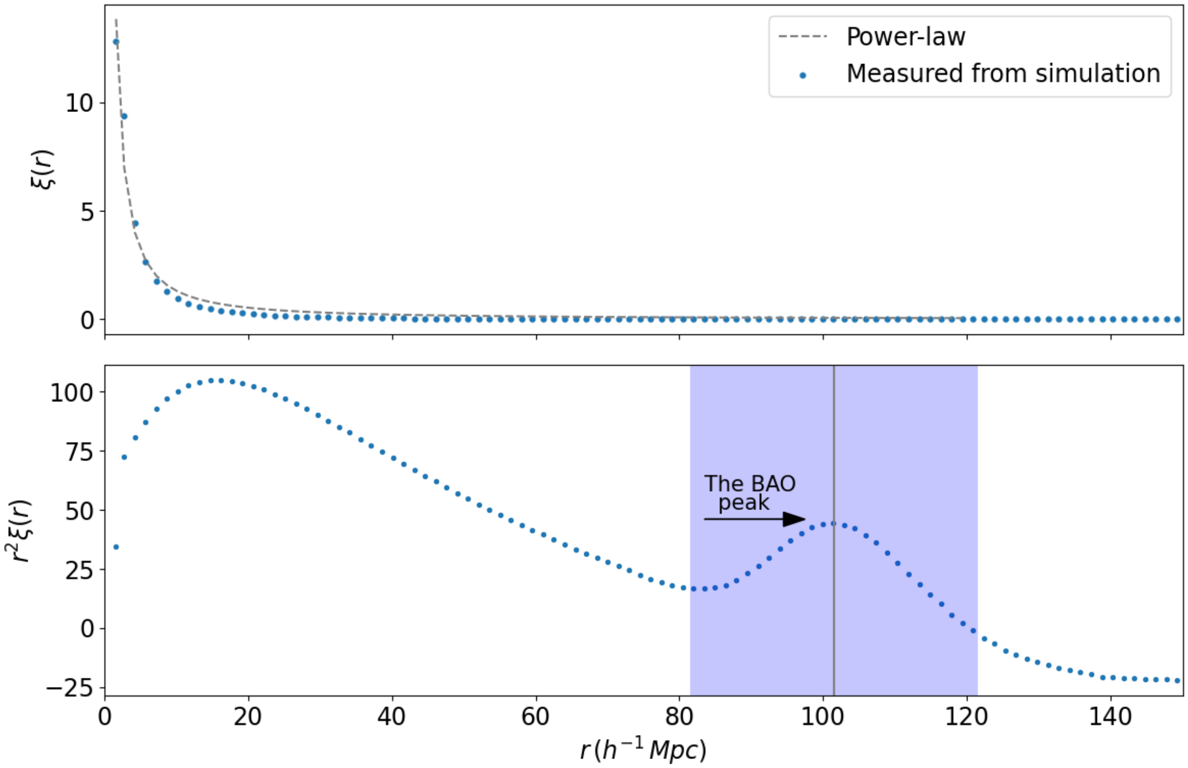

Figure 1.6: Measured correlation function (real space) from the mean of 1000 Quijote simulations shown in blue. Top: correlation function roughly follows a power-law distribution. For the BAO signal to be seen, the correlation function is multiplied by separation squared. Bottom: When the correlation function is multiplied by r^2, the BAO signal can be seen around $100\,h^{-1}$ Mpc.

Chapter 2

Fisher analysis of BAO and RSD

This work was published as [2], co-authored with Alex Krolewski and Will Percival. I undertook the Fisher analysis, wrote the code, and led the writing of the paper with input from them.

The goal of this chapter is to compare the constraints recovered from the BAO and RSD measurements of various surveys with the Fisher matrix predictions for the expected error bars. The inputs to the Fisher calculations match as closely as possible that of each analysis. The outline of this chapter is as follows. In Section 2.1, we briefly describe the Fisher matrix formalism and how it is applied in this chapter. We continue with descriptions of the surveys considered here in Section 2.2 and the numbers used throughout this chapter. In Section 2.3, we present our Fisher code results, and then compare them to the observations. In particular, we evaluate these surveys' performance, comparing the Fisher-predicted errors with the precision recovered from the BAO and RSD measurements. Finally, we discuss the results in Section 2.4.

2.1 Methodology

We now briefly describe how we perform the Fisher-based predictions for a given survey. In order to match the experiments, we separately predict errors for BAO and RSD measurements. Before describing the specifics of these calculations, we introduce the general Fisher matrix methodology that is not exclusive to cosmology, but rather can be used for estimating the errors of any given dataset.

Supposing that $\vec{x}$ is a random variable with the probability distribution $f(\vec{x};\vec{p})$, where $\vec{p}$ is a vector of known parameters, the Fisher information matrix ([68, 33]) corresponding to this set of variables is defined as

$$F_{i,j} \equiv -\left\langle \frac{\partial^2 \ln f}{\partial p_i \partial p_j} \right\rangle . \tag{2.1}$$

Applying this to galaxy surveys, we wish to estimate a set of cosmological parameters $\{p_1, p_2, ...\}$ using the redshift space galaxy power spectrum, $P(k,\mu)$, and the galaxy number density, n, in the survey's volume, V_{sur}. Following Tegmark (1997) [33], if we let the data vector $\vec{x}$ be the galaxy power spectrum for a Gaussian random field, Eq. 2.1 will yield the following expression for the Fisher matrix:

$$F_{ij} = \frac{V_{\text{sur}}}{4\pi^2} \int_{-1}^{1} d\mu \int_{k_{\text{min}}}^{k_{\text{max}}} k^2 dk \mathcal{F}_{ij}(k,\mu) \, , \tag{2.2}$$

where,

$$\begin{aligned} \mathcal{F}_{ij}(k,\mu) &= \frac{1}{2}\left(\frac{V_{\text{eff}}}{V_{\text{sur}}}\right) \frac{\partial \ln P}{\partial p_i} \frac{\partial \ln P}{\partial p_j} \, , \\ V_{\text{eff}} &= \left[\frac{nP(k,\mu)}{nP(k,\mu)+1}\right]^2 V_{\text{sur}} \, , \end{aligned} \tag{2.3}$$

and V_{eff} and μ are the effective volume and the cosine of the angle between $\vec{k}$ and the line of sight. In the linear regime, the power spectrum can be written

$$P = P(k,\mu) = (b + f\mu^2)^2 P_{\text{lin}}(k) \, , \tag{2.4}$$

where b, f, P_{lin} denote the galaxy bias, logarithmic growth rate and linear power spectrum.

We split each survey in N_z slices, and numerically integrate Eq. 2.2 in each redshift slice and eventually add the Fisher matrices to yield the inverse of the total covariance matrix. Moreover, for each survey, we assume the same fiducial cosmology as quoted in their corresponding BAO and RSD measurement chapter. For completeness, we list these in Table 2.1. In Section 2.1.1 and 2.1.2 we describe the constraints recovered from BAO and RSD analyses respectively.

2.1.1 The Fisher matrix for the BAO measurements

To predict the constraints on the parameters recovered from BAO measurements, we adapt the approach described in Seo & Eisenstein [69]. Following their method, we construct the Fisher matrix constraints on angular diameter distance D_M, and the Hubble distance D_H, meaning that the free parameters in Eq. 2.2 are $\{p_1, p_2\} = \{\ln D_M, \ln D_H\}$. These parameters can be related to the BAO dilation parameters as follows

$$\begin{aligned} \alpha_\perp &= \frac{D_M(z_{\text{eff}})/r_{\text{drag}}}{D_M^{\text{fid}}(z_{\text{eff}})/r_{\text{drag}}^{\text{fid}}}\,, \\ \alpha_\parallel &= \frac{D_H(z_{\text{eff}})/r_{\text{drag}}}{D_H^{\text{fid}}(z_{\text{eff}})/r_{\text{drag}}^{\text{fid}}}\,, \end{aligned} \tag{2.5}$$

where r_{drag} is the comoving sound horizon at the end of the baryon drag epoch. From these parameters we can further obtain the isotropic volume-averaged distance, $D_V = [zD_H(z)D_M(z)^2]^{1/3}$. The final expression for the Fisher matrix of the anisotropic distances, as described in Seo & Eisenstein, is

$$F_{i,j} = V_{\text{sur}} A_0^2 \int_0^1 d\mu f_i(\mu) f_j(\mu) \int_0^\infty dk \, \frac{k^2 \exp\left[-2(k\Sigma_s)^{1.4}\right]}{\left(\frac{P(k)}{P_{0.2}} + \frac{1}{nP_{0.2}R(\mu)}\right)^2} \exp\left[-k^2(1-\mu^2)\Sigma_\perp^2 - k^2\mu^2\Sigma_\parallel^2\right], \tag{2.6}$$

where $P_{0.2}$ is the galaxy power at $k = 0.2\,h\,\text{Mpc}^{-1}$, $\Sigma_\perp$ and $\Sigma_\parallel$ are the rms radial displacement across and along the line of sight, Σ_s is the inverse of the Silk-damping scale, and A_0 is the normalization of the baryonic term in the Eisenstein & Hu power spectrum [70]. Depending on which element of the Fisher matrix is being calculated, $f_1(\mu) = \mu^2 - 1$ and $f_2(\mu) = \mu^2$. They assumed redshift distortions of the form

$$R(\mu) = (1 + f\mu^2/b)^2 \exp\left(-k^2\mu^2\Sigma_z^2\right), \tag{2.7}$$

where f is the logarithmic derivative of the linear growth rate with respect to scale factor, $\mathrm{d}D(a)/d\ln(a)$, and b is the galaxy bias. The exponential term corresponds to a Gaussian uncertainty in redshift characterized by Σ_z, which will be discussed more in Section 2.2.

Since the normalisation and baryon damping terms in the power spectrum $P(k)$ in Eq. 2.6 are functions of Ω_b, Ω_m, and h, it is important to recalculate these for the cosmology assumed if it is different from the default in the version of the code publicly released by Seo & Eisenstein. As we adjust our Fisher calculations to match the cosmology assumed by different authors in their analyses, we have extended the code to allow the relevant

Table 2.1: A list of fiducial cosmologies used for each survey in the Fisher analysis.

Survey	Ω_m	Ω_b	h	σ_8	n_s	Ω_ν
6dFGS	0.3	0.0478	0.70	0.82	0.96	0
MGS	0.31	0.048	0.67	0.83	0.96	0
BOSS (DR12)	0.31	0.04814	0.676	0.8	0.97	0
BOSS (DR9-11)	0.274	0.0457	0.70	0.8	0.95	0
eBOSS	0.31	0.04814	0.676	0.8	0.97	0.0014
WiggleZ	0.27	0.04483	0.71	0.8	0.963	0

parameters to change, using the Eisenstein & Hu (1998) fitting function for the power spectrum. Additionally, since the experimental results that we compare against include reconstruction of the density field to better recover the linear power spectrum (dating back to Peebles [71] and Eisenstein et al. [72]), throughout this chapter we need to include it in our Fisher-based analyses as well. Therefore, as an estimation of the reconstruction, we decrease $\Sigma_\parallel$ and $\Sigma_\perp$ by 50% following ref. [69] and [72].

2.1.2 The Fisher matrix for the RSD measurements

In redshift space, the clustering of galaxies is distorted along the line of sight due to peculiar velocities. Measuring these redshift-space distortions (RSD) can provide a estimate of the growth rate of structure. In this Section, we describe how we predict such constraints using the Fisher formalism, following the method described in White et al. [34]. To start with, we consider $\{p_1, p_2\} = \{\ln b\sigma_8, \ln f\sigma_8\}$ as the set of our free parameters. The parameter of interest constraining the structure growth is $f\sigma_8$, where f is the logarithmic growth rate, and σ_8 is the amplitude of fluctuations in an $8\,h^{-1}\,\mathrm{Mpc}$ radius. For the purpose of this chapter the galaxy bias, b, is a nuisance parameter over which we marginalize.

We can rewrite Eq. 2.4 as

$$P = \left(b\sigma_8(z) + f\sigma_8(z)\mu^2\right)^2 \frac{P_m(k,z)}{\sigma_8(z)^2}\,. \tag{2.8}$$

Then after taking the partial derivatives we obtain

$$\begin{aligned} \frac{\partial \ln P}{\partial \ln p_1} &= \frac{2b\sigma_8(z)}{b\sigma_8(z) + f\sigma_8(z)\mu^2}\,, \\ \frac{\partial \ln P}{\partial \ln p_2} &= \frac{2\mu^2 f\sigma_8(z)}{b\sigma_8(z) + f\sigma_8(z)\mu^2}\,. \end{aligned} \tag{2.9}$$

By inserting Eq. 2.9 into Eq. 2.3, we can derive the constraints on $f\sigma_8$. In order to provide consistent predictions for all surveys for our baseline RSD-based Fisher predictions we assume that the dilation parameters $\alpha_\parallel$ and $\alpha_\perp$ are held fixed, rather than marginalizing over them. This limits the dependence on the BAO detection, which in turn controls how well the dilation parameters are constrained. Therefore, our results should not be directly compared to those from measurements where they marginalize over these parameters after performing a joint fit to data.

For many of the surveys, the authors provide errors for both fixed BAO dilation parameters ("αs") and results after marginalizing over them, which we refer to as $f\sigma_8^{\mathrm{fx.}\,\alpha\mathrm{s}}$, and $f\sigma_8^{\mathrm{mg.}\,\alpha\mathrm{s}}$, respectively. Other analyses provided the covariance matrices for the four parameters, from which we can calculate both. When marginalizing over dilation parameters, we simply take the square root of the $f\sigma_8$ diagonal element in the covariance matrix, $f\sigma_8^{\mathrm{mg.}\,\alpha\mathrm{s}} = \sqrt{C_{f\sigma_8,f\sigma_8}}$. To find $f\sigma_8^{\mathrm{fx.}\,\alpha\mathrm{s}}$, we calculate the $f\sigma_8$ error from the $f\sigma_8$ diagonal element of the inverse covariance matrix (the survey's Fisher matrix), $f\sigma_8^{\mathrm{fx.}\,\alpha\mathrm{s}} = [C^{-1}]^{-1/2}_{f\sigma_8,f\sigma_8}$. In Section 2.2, we briefly describe which method is used to set the correct values in Table 2.2 and Table 2.3.

2.1.3 Integration Limits (k_{min} and k_{max})

To forecast the Fisher-based analysis parameters, we need to make assumptions about the upper and lower limits of the integral in Eq. 2.2. Each survey is able to extract information up to scales comparable to its size. Formally, the integral constraint affects the power spectrum such that a copy of the window function centred at $k = 0$ is subtracted from the convolved power, leaving zero power at $k = 0$ (e.g. [73]). Thus, information on scales the size of the survey window is not present. To match this behaviour, we choose the lower limit of our integral over scales to be $k_{\mathrm{min}} = 2\pi V_{\mathrm{sur}}^{-1/3}$ ([33, 36]) mimicking the effect of the window with a sharp cut in scales included. The choice of k_{max}, on the other hand, depends on the scales to which we can extract linear information. The non-linear evolution primarily affects the BAO through well controlled damping terms $\Sigma_\perp$ and $\Sigma_\parallel$, and thus Seo & Eisenstein [69] suggested that when extracting the BAO parameters, we can set $k_{\max} = 0.5\,h\,\mathrm{Mpc}^{-1}$. Indeed, we find that $\sigma_{\ln D_V}$ is not sensitive to the choice of $k_{\max}$ for $k \gtrsim 0.3\,h\,\mathrm{Mpc}^{-1}$; the BAO provide a large-scale signal localized in configuration space, such that in k-space the signal rapidly diminishes to small scales (See the left panel of Fig. 2.1). This finding agrees very well with results from N-body simulations [69], which also found that the error is stable for $k_{\max} = 0.3, 0.4$, and $0.5\,h\,\mathrm{Mpc}^{-1}$.

For the RSD measurements, we found that $\sigma_{\ln f\sigma_8}$ is highly dependent on the choice of $k_{\max}$. On small scales, the density field becomes highly non-Gaussian and hence the inverse of the linear Fisher matrix gives a more optimistic estimation of the error bars than the measurements. The reduction in linear information available is gradual: in models, this results in an increased dependence on non-linear parameters, often allowed to be free given unknown non-linear effects including beyond-linear galaxy bias. The exact scale at which we stop being able to recover linear information is expected to depend on the details of the galaxy population, and on the accuracy and number of free parameters included in the model used. This problem leads us to test the Fisher error bars' sensitivity to the change of $k_{\max}$. Our default prediction is to calculate the expected error on $f\sigma_8$ up to a fiducial $k_{\max} = 0.1/D(z = z_i)\,h\,\mathrm{Mpc}^{-1}$ at each redshift slice. This is based on arguments made by Okumura et al. [74], where they showed that after this scale the power spectrum turns strongly non-linear to the extent that a Taylor series cannot adequately describe the redshift-space density field anymore [35].

We also consider inverting the problem and using the data measurements to determine what $k_{\max}$ we should use. To do so, we vary $k_{\max}$ from $0.01/D(z_i)$ up to $0.5/D(z_i)$ and we plot $f\sigma_8$ error against $k_{\max}(z_{\text{eff}})$ in Figure 2.1. This allows us to translate the constraining power of RSD measurements to an effective $k_{\max}$ at which an equivalent amount of information can be extracted from the linear power spectrum.

2.2 Data and modelling

In this section, we introduce the surveys on which we perform our Fisher analysis: SDSS-I&II Main Galaxy Sample (MGS), SDSS-III Baryon Oscillation Spectroscopic Survey (BOSS), SDSS-IV extended Baryon Oscillation Spectroscopic Survey (eBOSS), and WiggleZ Dark Energy Survey (WiggleZ). To test our code, we compare to the predictions in Zhao et al. [36] for eBOSS, and find that both codes match in giving very similar results for the same input parameters. In our paper, we are only interested in understanding and matching to the statistical errors and so, where appropriate, we have removed the quoted systematic errors from any combined constraints by subtracting them in quadrature.

Uncertainty in redshift estimation can increase uncertainty in the BAO and RSD features by damping the radial component of the power spectrum (as explained in Section 2.1). The observations require that $\sigma_v \equiv c\sigma_z/(1+z) \leq 10^{-3}c$ for galaxies at all redshifts. However, the quasar clustering measurements suggest that while this requirement holds true for low redshifts, higher redshifts are prone to higher velocity errors. Therefore, when performing our Fisher analysis on the surveys described in Section 2.2, we assume that the velocity error for quasars has the following form (Zarrouk et al. [75]):

$$\frac{\sigma_v}{c} = \left\{ \begin{array}{ll} 10^{-3}, & \text{if } z \leq 1.5 \\ \frac{4}{3} \times 10^{-3}(z-1.5) + 10^{-3}, & \text{if } z > 1.5 \end{array} \right\} . \tag{2.10}$$

We use $\sigma_v = 10^{-3}c$ for all other tracers, and we include the redshift error in both the RSD and BAO Fisher predictions.

Many of the papers introduced in the following sections use mock catalogues for the following reasons: to estimate systematic errors, to test the model of power spectrum or the correlation function, and to better estimate the covariance matrices from the measurements. Noise in the data may lead to error bars that are larger or smaller than the true constraining power of the survey just by chance. To examine this possibility, we also compare the $f\sigma_8$ constraints on mocks to our Fisher-based errors, where available. In general, the results from the fits to mocks provide error bars similar to those obtained from the data (results are shown in left panel of Figure 2.4).

2.2.1 Reconstruction Technique

As already described, the BAO feature can be estimated either by measuring the peak in the correlation function or by the harmonic sequence of oscillations in the power spectrum. As gravitational forces make structure grow through time, this signature blurs, meaning that the precision at which we can measure the BAO signal decreases. In order to sharpen the broadened BAO signal, various reconstruction methods have been proposed based on the idea of rewinding the motion of galaxies to move them into their original positions. The strong impact of using even simple methods to do this on BAO measurements was first described by Eisenstein et al. ([72, 76]), who proposed a method to shift the galaxies' position by the linear-theory estimated Lagrangian displacement field and showed that this process can increase the precision of the BAO signal. In this section, we discuss some reconstruction methods that have been applied to the data papers that we consider throughout this chapter.

A significant difficulty in implementing reconstruction arises because of the RSD, and particularly that the RSD direction changes across a survey. This problem has been solved in recent analyses using two different methods. Padmanabhan et al. [77] implemented a finite-difference routine based solving for the potential on a grid covering the survey's volume. The direction of the RSD signal is allowed to vary for different grid points. Burden et al. [78, 79] instead showed how the simple linear theory based reconstruction method can be undertaken in the Fourier space. To allow for RSD without forcing a global plane-parallel approximation, the code is iterative, removing the estimated RSD signal based on the potential field found in a previous step where no RSD was assumed to be present. The authors also tested their method on CMASS DR11 mocks and found that it converges rapidly, requiring only two iterations.

The way in which reconstruction works is described in more detail in Padmanabhan et al. [80] and one important aspect is that the field be smoothed, with a smoothing scale of between 10 and 15 $h^{-1}\,$Mpc [79]. Note that while many techniques also leave a field in which the RSD have approximately been removed, this is not a necessary part of the code and the BAO positions and signal strength do not depend on this. The power spectrum (or correlation function) after reconstruction has a complicated form: ref. [80] suggested that the power spectrum be modeled using three nonlinear damping terms and over three wavelength ranges. Thus, while modelling the full post-reconstruction clustering signal is difficult and may change the shape of the clustering in a hard-to-model way, what is clear is that these reconstruction techniques can decrease $\Sigma_\parallel$ and $\Sigma_\perp$ by 50% for the BAO. Thus if one is only concerned with the BAO signal, allowing for smooth changes in the shape of the power to isolate only this signal removes the pernicious effects of reconstruction. Applying this method to the SDSS DR7 sample showed that it reduces the BAO distance error by a factor of 1.8 [80]. The improvement is not universal, with samples reacting differently to reconstruction [24], but it clearly works to improve the average recovered signal for a set of volumes of the Universe.

The methods described above are relatively simple, relying only on linear physics. More sophisticated techniques offer the promise of increased improvements in the future (e.g. [81, 82, 83, 84]). All of the analyses we consider in this chapter, except for quasars, used simple methods for reconstruction, and we assume a 50% improvement on $\Sigma_\parallel$ and $\Sigma_\perp$ from this.

2.2.2 RSD modelling

The amount of information that RSD surveys can extract is limited by modelling the power spectrum or correlation function: the data, at least in 2-point form, does not itself provide information about which scales are linear. Even if the data match a linear model, this does not mean that all of the linear information is present, as cancellation of multiple effects is possible (e.g. Fingers-of-God and non-linear growth in the monopole). Therefore, the fidelity of the RSD modelling will limit the amount of information extracted. In this section we briefly describe the models used in the data papers that we consider.

Fourier space: The simplest RSD model for the power spectrum was first introduced by Kaiser in 1987 [48]. As it does not include nonlinearities in the halo power spectrum, it is therefore only applicable on large scales. Scoccimarro later constructed a fitting model for RSD in 2004 (Sc.; [85]), as a nonlinear extension to the linear Kaiser model (1987) [48] with two free parameters. Scoccimarro's extension can include Gaussian and non-Gaussian contributions to the velocity dispersion of large-scale flows. Later in 2010, the matter power spectrum in redshift space was developed by Taruya, Nishimichi, and Saito (TNS; [86]). They added various coefficients to the Scoccimarro's model to account for nonlinearities between the density field and the velocity field and presented a new power spectrum in redshift space for modeling BAO, including nonlinear gravitational clustering and RSD. The TNS model is amongst the most popular RSD models in Fourier space, of which many of the most recent surveys described in this section make use. Since all of these fitting formulae break down on small scales, they limit their analyses to a maximum k, which is reported as $k_{\max}$(O.) in Table 2.2 and 2.3.

Configuration space: One model that includes nonlinearities in the correlation function in redshift space at quasi-linear scales is the streaming model by Reid & White [56]. They modelled the nonlinear mapping between the real and redshift space with the Gaussian streaming model, in which they included the dependence of halo pairwise velocities on their separation and angle with respect to the line-of-sight. We refer to this RSD model as R+11.

A more realistic way to model RSD in configuration space is to model the intrinsic galaxy clustering and the velocity field with Convolved Lagrangian Perturbation Theory

(CLPT; [87]) and then model the convolution of the velocity field along the line-of-sight with the Gaussian Streaming model (GS; [56]). Throughout, we refer to this method as CLPT+GS RSD model. On the other hand, Jennings et al. (J+11; [88]) proposed a cosmology-independent relationship between the velocity field and the density field, from which they found an RSD fitting model based on the nonlinear velocity divergence matter power spectrum. In addition, Sanchez et al. [89] described a simple recipe for modelling the full shape of the clustering wedges that we refer to as S+13. The nonlinear power spectrum in this model is motivated by RPT [90]. A variation of this method, gRPT [91, 92] has also been used by ref. [93].

The maximum wavenumber used in Fourier analyses, as stated before, is given by the so-called $k_{\rm max}$. The analogous scale in real space is the smallest scale in the correlation function from which authors can extract information, and is usually referred to as $s_{\rm min}$. In our paper, we are interested in comparing the Fisher-based $k_{\rm max}$ with that of the measurements. For the purposes of Table 2.2 and Table 2.3, whenever the analysis is done in configuration space, we approximate $k_{\rm max}$ with $\sim 1.15\pi/s_{\rm min}$, based on arguments made by [56]. This allows us to compare the smallest scales used in both real and Fourier space RSD analyses with the effective $k_{\rm max}$ corresponding to the total amount of linear information available.

2.2.3 6-degree Field Galaxy Survey

The 6dFGS survey was undertaken from 2001 to 2006 using the Six-Degree Field multi-fibre instrument of the UK Schmidt Telescope (UKST) [94]. This survey covered more than $125,000$ galaxies over $\sim 17,000\ {\rm deg}^2$ of the southern sky in the redshift range $z < 0.3$ with a median redshift of $z_{\rm med} = 0.053$.

For the BAO analysis, we use the same catalogue as Carter et al. [95], which contains $75,117$ galaxies after applying cuts to the magnitude and the completeness. This catalogue has an effective redshift of $z_{\rm eff} = 0.097$ and an effective bias of $b_{\rm eff} = 1.65$. The early analysis of Beutler et al. [62] was recently supplanted by an analysis that used more modern techniques, including reconstruction from Burden et al. (2014, 2015) with a smoothing scale of $15\,h^{-1}$ Mpc and a covariance matrix based on more sophisticated simulations (i.e. [95]). They found that the 6dFGS likelihood is bimodal, with a 4.6% error on D_V for the best fit model. The authors combined the post-reconstruction 6dFGS with the SDSS MGS sample and reported the lowest fractional error to date on D_V, 3.2%, at low redshift. This favoured the second most likely peak seen when fitting the post-reconstruction BAO signal in the 6dFGS. The 6dFGS sample only adds enough information to provide an improvement of $\sim 16\%$ on the MGS BAO measurements at low redshift. For our analysis we include results from the 6dFGS separately from the MGS as we are interested in the surveys independently.

Beutler et al. in 2012 [96], used a slightly different catalogue containing $81,971$ galaxies to make RSD-based measurements. They made use of two RSD models for the 2D correlation function in configuration space, namely, the Simple Streaming model down to $r = 10\,h^{-1}\,\mathrm{Mpc}$ and the Scoccimarro model down to $r = 16\,h^{-1}\,\mathrm{Mpc}$ or $k_{\max} \sim 0.23\,h\,\mathrm{Mpc}^{-1}$ (Sc. in Table 2.2). We only report the results with the Scoccimarro model as it only fits for the two parameters of interest, $f\sigma_8$ and $b\sigma_8$, and it gives a fractional error on their measurement of $f\sigma_8^{\mathrm{fx.}\,\alpha\mathrm{s}}$ of 13.0%. Since they do not fit the dilation parameters in their model, we consider their result as if dilation parameters were fixed, i.e, the error on $f\sigma_8^{\mathrm{fx.}\,\alpha\mathrm{s}}$ is 13.0%, and in Table 2.2 we do not report the $f\sigma_8^{\mathrm{mg.}\,\alpha\mathrm{s}}$ for this survey. They also varied their fiducial cosmology without their results changing. This is because the degeneracy between RSD parameters and dilation parameters is very small at low redshift.

2.2.4 Main Galaxy Sample SDSS-I&II

The Main Galaxy Sample (MGS) is a part of the seventh data release (DR7; [26]) of SDSS I&II ([20]), using observations from the 2.5-meter Sloan telescope located at Apache Point Observatory (APO; Gunn et al. [97]). In this chapter, we consider the subsample of $63,163$ galaxies covering $6,318$ deg^2 of the sky, with a redshift range of $0.07 < z < 0.2$ and an effective bias of 1.5 created by Ross et al. [98]. The MGS sample contains significantly more galaxies than this but, because it was volume limited, a high bias subsample was selected for analysis in order to facilitate the creation of mock catalogues from simulations (which then only required halos to a higher halo mass limit). Ross et al. followed the standard linear reconstruction prescription using the Fourier based method, and found that reconstruction improved the BAO signal by a factor of 2. The post-reconstruction D_V was measured to an accuracy of 3.8%, and there was no evidence of systematic errors. In addition, based on the post-reconstruction BAO measurements and using the CLPT RSD model in range $25 < s < 160\,h^{-1}\,\mathrm{Mpc}$ ($k_{\max} = 0.14\,h\,\mathrm{Mpc}^{-1}$), Howlett et al. [63] measured $f\sigma_8^{\mathrm{fx.}\,\alpha\mathrm{s}}$ and $f\sigma_8^{\mathrm{mg.}\,\alpha\mathrm{s}}$ to an accuracy of 31.8% and 40.5% respectively (Table 2, eighth and second case).[1] Moreover, in order to estimate the covariance matrix precisely, 1000 mock catalogues from PICOLA code have been analysed for the MGS sample by Howlett et al. [63]. They found that the best fit value from the average of these mocks gives $f\sigma_8^{\mathrm{fx.}\,\alpha\mathrm{s}} = 0.5^{+0.13}_{-0.12}$. (Table 1, 8th case).

---

[1] Since the error bars in this analysis are asymmetric, we average the upper and lower error bars.

2.2.5 Baryon Oscillation Spectroscopic Survey SDSS-III

The Baryon Oscillation Spectroscopic Survey (BOSS) [28] is a part of the SDSS-III [27] that was undertaken by the 2.5-meter Sloan Telescope from 2008 to 2014. Covering an area of 10,000 $\deg^2$, BOSS contains more than 1.5 million galaxies with redshifts up to $z = 0.7$. Two target selection algorithms were used to create the BOSS galaxy sample: LOWZ (at lower redshift) is a selection of luminous red galaxies to $z \approx 0.4$, and CMASS (for constant stellar Mass) covers LRGs up to a higher redshift range $z \lesssim 0.7$ [99]. We review the catalogue selection and the BAO and RSD measurements in three early data releases of BOSS, DR9, DR10, and DR11 in Section 2.2.5, and the final data release DR12, in Section 2.2.5.

Intermediate Data Releases DR9-11

The BOSS DR9 CMASS sample contains $264,283$ galaxies in a region of $3,275\text{deg}^2$ of the sky. Galaxies used in this catalogue cover a redshift range of $0.43 < z < 0.7$ with an effective redshift of $z_{\text{eff}} = 0.57$. BAO measurements of were presented by Anderson et al. [24] and showed that $\sigma \ln D_V = 1.6\%$. Anderson et al. used the finite difference reconstruction method with a smoothing scale of $15\,h^{-1}\,\text{Mpc}$, and found that applying reconstruction to this particular data does not improve the precision of the BAO feature. They suggested that this is because the pre-reconstruction errors of this sample were already at the lower end of the expected range (from mocks)—hence there was little for reconstruction to improve. RSD measurements for this survey were presented in Reid et al. [100] providing fractional error bars on the growth rate $f\sigma_8^{\text{mg.}\,\alpha\text{s}} = 14.6\%$ and $f\sigma_8^{\text{fx.}\,\alpha\text{s}} = 8.1\%$. For both of these analyses, the systematic errors were negligible compared to the statistical errors. Their findings show that $b\sigma_8(z_{\text{eff}}) = 1.2$, where $\sigma_8(z_{\text{eff}}) = 0.61$, which gives an effective bias of 2.0. They fit the monopole and quadrupole moments of the correlation function down to scales of $s_{\text{min}} = 25\,h^{-1}\,\text{Mpc}$ (or $k_{\text{max}} \sim 0.14\,h\,\text{Mpc}^{-1}$) with Reid & White's RSD model [56].

BOSS Data Release 10 (DR10) contains $218,905$ galaxies in LOWZ ($0.15 < z < 0.43$) and $501,844$ galaxies in CMASS ($0.43 < z < 0.7$). Using these catalogues, D_V was constrained to 2.8% and 1.4% for LOWZ and CMASS, respectively, by Anderson et al. [101]. They also measured the anisotropy distances for CMASS in this catalogue and found a consensus ($P(k) + \xi(s)$) error of 1.9% and 5.0% on D_M and D_H, respectively. Anderson et al. [101] also analyzed the 11th data release of BOSS, which consists of $313,780$ galaxies in LOWZ and $690,826$ galaxies in CMASS. This gave a statistical consensus ($P(k) + \xi(s)$) error of of 2.0% and 0.9% on D_V for LOWZ and CMASS, respectively (after subtracting

0.3% systematic error in quadrature). They also found errors of 1.4% and 3.5% for the anisotropic distances, D_M and D_H, respectively. For both DR10 and DR11 data, the reconstruction method by Padmanabhan et al. was applied to NGC and SGC separately.

Sanchez et al. [102] constrained the logarithmic growth of structure using the 10th and 11th BOSS data releases, using the S+13 model described earlier, within the range of $40\,h^{-1}\,\mathrm{Mpc} < s < 160\,h^{-1}\,\mathrm{Mpc}$ or a $k_{\max}$ of $0.09\,h\,\mathrm{Mpc}^{-1}$. They found fractional errors of 23.3%, 12.8%, 20.8%, and 10.8% on $f\sigma_8^{\mathrm{mg.}\,\alpha s}$, for LOWZ DR10, CMASS DR10, LOWZ DR11, and CMASS DR11, respectively.

Since Sanchez et al. did not publish either the $f\sigma_8^{\mathrm{fx.}\,\alpha s}$, nor the covariance matrix including growth rate and dilation constraints for BOSS DR10 and DR11 samples, we are limited in how well we can replicate these results. Therefore, we use the CMASS DR11 RSD measurements from Samushia et al. [103] instead. These used the RSD streaming model described in Reid & White (R+11, [56]) with $s_{\min} = 25\,h^{-1}\,\mathrm{Mpc}$ or $k_{\max} \sim 0.14\,h\,\mathrm{Mpc}^{-1}$, finding errors of 9.9% and 6.0% on $f\sigma_8^{\mathrm{mg.}\,\alpha s}$ and $f\sigma_8^{\mathrm{fx.}\,\alpha s}$ respectively, which we include in Table 2.3. Systematic errors have been ignored in this analysis since they have been checked with mocks and they had less than a 1% effect. When fitted to growth of structure separate from the dilation parameters, they found $b\sigma_8 = 1.26$, which gives an effective bias of $b(z_{\mathrm{eff}}) = 2.05$ given that $\sigma_8(z = 0.57) = 0.615$.

Final Data Release DR12

To determine the Fisher-based predictions for the final data release of BOSS, DR12, we follow the data selection method of two studies. First, Alam et al. [64] who split this sample by redshift range (Near and Mid in Table 2.2) and second, Gil-Marín et al. [104], who studied the LOWZ and CMASS catalogues separately (LZ and CM in Table 2.3). In the following, we discuss the recovered errors for BAO and RSD measurements for both selection methods.

Alam et al. combined LOWZ with CMASS, and after applying redshift cuts to the combined sample, they created three partially overlapping redshift samples that cover 9329 deg^2 area of the sky. In this chapter, we refer to the first redshift bin, at $0.2 < z < 0.5$, which mainly consists of the LOWZ galaxy sample, as the near redshift bin, and the second redshift bin at $0.4 < z < 0.6$, mainly consisting of the CMASS sample, as the mid redshift bin, with effective redshifts $z_{\mathrm{eff},1} = 0.38$ and $z_{\mathrm{eff},2} = 0.51$ respectively. In our work, we do not consider the higher redshift bin at $0.5 < z < 0.75$ of the BOSS survey, as it is combined with the eBOSS LRG samples (refer to Section 2.2.6). According to Table 3 in Beutler et al., BOSS has an effective bias of 2.03, and 2.13 in the LOWZ and CMASS samples. Note that the Luminous Red Galaxy (LRG) samples in this chapter are assumed to have a galaxy bias of $b_{\mathrm{LRG}}(z) = 1.7/D(z)$, where D(z) is the linear growth factor. This assumption is consistent with the fiducial bias assumed in Zhao et al. [105] and Prakash et al. [106], as well as the effective biases measured for the LOWZ and CMASS samples.

The post-reconstruction BAO-only analysis by Alam et al. yields a 1.5%, 2.7%, and 1.0% statistical uncertainty in D_M, D_H, D_V for the BOSS Near sample. For the BOSS Mid sample, these uncertainties are lower: 1.4%, 2.3% and 0.9% for D_M, D_H, and D_V respectively. They used the reconstruction method described in Padmanabhan et al. For the constraint on the growth rate, Alam et al. incorporated results from 4 different papers, using different methods: real-space multipoles (Satpathy et al. [107]; CLPT+GS, $s_{\min} = 25\,h^{-1}\,\mathrm{Mpc}$), real-space wedges (Sanchez et al. [91]; similar to TNS, $s_{\min} = 20\,h^{-1}\,\mathrm{Mpc}$), Fourier-space multpoles (Beutler et al. [73]; TNS, $k_{\max} = 0.15\,h\,\mathrm{Mpc}^{-1}$), and Fourier-space wedges (Grieb et al. [93]; gRPT+RSD, $k_{\max} = 0.2\,h\,\mathrm{Mpc}^{-1}$). The BAO+FS consensus measurements from all of these works yield a 7.8% statistical error on $f\sigma_8^{\mathrm{mg.}\,\alpha\mathrm{s}}$ for the near redshift bin, and 7.6% for the mid redshift bin. We utilized the covariance matrix to obtain the constraint on $f\sigma_8^{\mathrm{fx.}\,\alpha\mathrm{s}}$, which is 7.0% for the near redshift slice and 6.4% for the mid redshift slice.

In addition, BOSS DR12 measured BAO ([108]) and RSD ([104]) using LOWZ and CMASS samples, consisting of $361,762$, and $777,202$ galaxies within the redshift ranges $0.15 < z < 0.43$, and $0.43 < z < 0.70$, and with effective redshifts of 0.32, and 0.57. They found that $b\sigma_8$ for these two samples are 1.29 and 1.24, resulting in an effective bias of 1.9 and 2.1, respectively. Throughout their study, they have made use of the finite-difference reconstruction method by Padmanabhan et al.

The BAO-only consensus analysis in real space and Fourier space have shown errors of 2.2%, 5.9%, and 1.7% on D_M, D_H, and D_V in the LOWZ sample, and 1.3%, 2.9%, and 0.9% on D_M, D_H, and D_V in the CMASS sample (Table 4 in [108]). Moreover, after modelling the RSD with the TNS model with a $k_{\max}$ of $0.24\,h\,\mathrm{Mpc}^{-1}$, Gil-Marín et al. [104] measured $f\sigma_8^{\mathrm{mg.}\,\alpha\mathrm{s}}$ with an error of 15.7% and 8.6%, and when assuming no AP effect, they measured $f\sigma_8^{\mathrm{fx.}\,\alpha\mathrm{s}}$ with an error of 9.1% and 5.0% in LOWZ and CMASS samples respectively (Table 3 in [104]).

2.2.6 Extended Baryon Oscillation Spectroscopic Survey SDSS-IV

The extended Baryon Oscillation Spectroscopic Survey (eBOSS; Dawson et al.) [30] is a part of SDSS-IV (Blanton et al. [29]), and used the Sloan Telescope at Apache Point

Observatory (APO; Gunn et al. [97]) to conduct a redshift survey at higher redshifts than BOSS from 2014 to 2019. From this survey's 16th data release, we use the DR16 Luminous Red Galaxy (LRG [109]; Section 2.2.6), Emission Line Galaxy (ELG [110]; Section 2.2.6), and Quasar samples ([111]; Section 2.2.6), which are reported in Table 2.2. We have also used the LRG and Quasar samples from an earlier data release, DR14 (Pâris et al. [112]), which are reported in Table 2.3. Since for eBOSS the systematic errors are estimated using mock catalogues, in this section we only quote the statistical error bars.

LRGs

There are $174,816$ LRGs in eBOSS DR16 sample that cover $9,493\,\mathrm{deg}^2$ of the night sky, with an effective redshift of $z_{\mathrm{eff}} = 0.698$. For LRGs in the redshift range $0.6 < z < 1.0$, we combine the eBOSS LRG sample with $202,642$ CMASS BOSS DR12 galaxies, to be consistent with the Bautista et al. [65] contraints. We want the Fisher forecast to have the same effective bias as the full MCMC fit to the TNS model, which is $b_1 = 2.2$. Therefore, we assume that the linear bias has the form of $1.5/D(z)$.

The estimated covariance matrix reported by Bautista et al. [65], for the BAO-only analysis, after applying the reconstruction technique of Burden et al. [78, 79], showed that the fractional statistical errors on D_M, D_H, and D_V, are 1.6%, 2.5%, and 1.6% respectively.

For obtaining the growth rate, they used CLPT+GS RSD to model correlation function in real space and combined their results with the Fourier-space analysis of Gil-Marín et al. [113], which used the TNS model. In this chapter we use their consensus results. They tested for different fitting ranges of scales, and found that the optimal minimum scales that should be covered in the CLPT+GS and TNS model are $25\,h^{-1}\,\mathrm{Mpc}$ ($k_{\max} \sim 0.14\,h\,\mathrm{Mpc}^{-1}$) and $20\,h^{-1}\,\mathrm{Mpc}$ ($k_{\max} \sim 0.18\,h\,\mathrm{Mpc}^{-1}$), respectively.

The consensus BAO + Full Shape RSD fit indicated that the error on $f\sigma_8^{\mathrm{mg.}\,\alpha\mathrm{s}}$ and $f\sigma_8^{\mathrm{fx.}\,\alpha\mathrm{s}}$ are 9.4% and 9.1% (from eq. 56 in ref. [65]). In Table 10 of Bautista et al. they evaluated the systematic errors using mocks, and showed that the systematic error of $f\sigma_8$ for CLPT and TNS is 0.024 and 0.023 respectively. If we subtract ~ 0.0235 from the total error obtained from Eq. 56, in quadrature, then we obtain an error of 7.9% and 7.6% on $f\sigma_8^{\mathrm{mg.}\,\alpha\mathrm{s}}$ and $f\sigma_8^{\mathrm{fx.}\,\alpha\mathrm{s}}$. Furthermore, for this catalogue, they constructed 1000 EZmock realisations for the LRG eBOSS+CMASS survey geometry and obtained 9.9% error on $f\sigma_8^{\mathrm{fx.}\,\alpha\mathrm{s}}$ in the mocks, which is shown in Figure 2.4.

An earlier data release of the eBOSS LRG sample, DR14, when combined with CMASS, is comprised of $126,557$ galaxies in redshift range $0.6 < z < 1.0$, with an effective redshift $z_{\mathrm{eff}} = 0.720$. Bautista et al. [114] followed the reconstruction technique presented by

Burden et al. [78, 79], and the post-reconstruction BAO measurement analysed by them showed a 2.5% fractional error on D_V. The anisotropic fits on this data shows very different upper and lower error bars: $D_M = 2689^{+158}_{-79}$, and $D_H = 2593^{+177}_{-589}$. Hence we do not report these errors in Table 2.3. But the isotropic fit shows that $D_V = 2377^{+61}_{-59}$ which translates into 2.5% fractional error. The RSD measurement for this sample has been modeled with CLPT+GS model by Icaza-Lizaola et al. [115] on scales $28 < s < 124$ $h\,\mathrm{Mpc}^{-1}$ ($k_{\max} = 0.13\,h\,\mathrm{Mpc}^{-1}$) and they found a fractional error of 29.2% on $f\sigma_8^{\mathrm{mg.}\,\alpha\mathrm{s}}$. Using the covariance matrix of their analysis, we found a fractional error of 10.4% for $f\sigma_8^{\mathrm{fx.}\,\alpha\mathrm{s}}$. Their fit showed that $b\sigma_8 = 1.11$ (Table B1 in ref. [115]), which means assuming $D(z_{\mathrm{eff}} = 0.72) = 0.691$, the effective bias would be $b_{\mathrm{eff}} = 2.0$. We therefore use the functional form of $1.4/D(z)$ for bias evolution in our Fisher analysis.

ELGs

The 16^{th} data release of SDSS-IV contains 173,736 Emission Line Galaxies (ELGs) covering an effective area of 727 deg^2 at effective redshift $z_{\mathrm{eff}} = 0.845$ in the redshift range $0.6 < z < 1.1$ (de Mattia et al. [116] & Tamone et al. [117]). Tamone et al. fitted for galaxy bias and found that $b = 1.52$. Therefore, for this sample, we assume a galaxy bias function of $b_{\mathrm{ELG}}(z) = 0.99/D(z)$, as $D(z_{\mathrm{eff}} = 0.85) = 0.651$.

De Mattia et al. applied the iterative FFT reconstruction method introduced by Burden et al. and assumed a Gaussian smoothing scale of 15 $h^{-1}\,\mathrm{Mpc}$. The isotropic BAO measurements in Fourier space for this sample gave statistical upper error of 2.5% and lower error of 2.8% for D_V, which is a factor of 1.2 smaller than the total errors. We averaged the upper and lower error bars for reporting in Table 2.2 (refer to Table 9 of ref. [116] for statistical-only errors).

They also performed the Fourier space BAO+RSD measurements using the TNS model in the fitting range $0.03 < k < 0.2$ $h\,\mathrm{Mpc}^{-1}$ for the monopole. However, at the end they combined their results with the configuration space result from Tamone et al. [117], which used the CLPT+GS RSD model with $s_{\min} = 32\,h^{-1}\,\mathrm{Mpc}$ or equivalently, $k_{\max} \sim 0.11\,h\,\mathrm{Mpc}^{-1}$. Statistical only errors on $f\sigma_8^{\mathrm{mg.}\,\alpha\mathrm{s}}$, D_H, and D_M as calculated by de Mattia et al., are 23.4%, 9.0%, and 3.9% , whereas Tamone et al. obtained 23.9%, 9.1%, and 4.6%, respectively. Combining these two measurements we find statistical fractional errors of 23.6%, 9.0% and 4.3% on $f\sigma_8^{\mathrm{mg.}\,\alpha\mathrm{s}}$, D_H, and D_M. Since the ELG likelihood in the BOSS DR16 sample cannot be adequately approximated with a Gaussian, instead of using the covariance matrix to fix the dilation parameters, we use the supplied probability grid in D_M and D_H, measuring the error on $f\sigma_8$ when D_M and D_H are constrained within a small range around their best-fit values. By doing so, we find a 15.2% error on $f\sigma_8^{\mathrm{fx.}\,\alpha\mathrm{s}}$.

De Mattia et al. tested their analysis using different mock catalogues and found that the baseline Global Integral Constraint model (baseline, GIC) gives an 11.5% error on $f\sigma_8^{\mathrm{fx.}\,\alpha\mathrm{s}}$, which is shown in Figure 2.1.

Quasars

Quasar samples are of significant interest when it comes to constraining parameters at high redshift. In this study, we include the eBOSS DR16 sample containing $343,708$ Quasars covering $4,699$ deg^2 in the redshift range $0.8 < z < 2.2$, with an effective redshift of $z_{\mathrm{eff}} = 1.48$ (Neveux et al. [66]). According to Croom et al. [118], the quasar bias can be approximated as $b(z)_{\mathrm{QSO}} = 0.53 + 0.29(1+z)^2$, which gives an effective bias of 2.31. Taking the average of best fits on $b_{1,\mathrm{NGC}}\sigma_8$ and $b_{1,\mathrm{SGC}}\sigma_8$ from their Table 10, and dividing by $\sigma_8(z_{\mathrm{eff}} = 1.48) = 0.41$, implies that the best fit effective bias is 2.33, which is very similar to the Croom formula. Note that BAO reconstruction is not applied to quasars, as their density is too low to provide us with an adequate estimate of the matter density field.

BAO-only measurements by Neveux et al. [66] in Fourier space, combined with those from configuration space by Hou et al. [119], gives the consensus errors of 2.6%, 4.1%, and 1.6% for D_M, D_H, and D_V (Table 6 in [66]). By subtracting the systematic errors in quadrature, according to their Table 5, we find that these numbers change only slightly, and become 2.5%, 4.0%, and 1.5% for D_M, D_H, and D_V.

Neveux et al. [66] used the TNS model for RSD measurements within the range $0.02 < k < 0.3\ h\,\mathrm{Mpc}^{-1}$, and obtained a 9.9% error on $f\sigma_8^{\mathrm{mg.}\,\alpha\mathrm{s}}$. Whereas Hou et al. [119] introduced a new method similar to TNS in order to model the correlation function within the scale range of $20 < s_{\min} < 160\,h^{-1}\,\mathrm{Mpc}$) ($k_{\max} \sim 0.18$), and found a 10.9% error on $f\sigma_8^{\mathrm{mg.}\,\alpha\mathrm{s}}$. When combining the two to find a consensus result, this reduced to 9.7%. Considering that both of these papers estimated that the systematic error is about 30% of the statistical error, that gives a final only-statistical error of 9.3% on $f\sigma_8^{\mathrm{mg.}\,\alpha\mathrm{s}}$. After fixing the dilation parameters using the covariance matrix for the full shape analysis, and subtracting the 30% systematic error in quadrature, we found that $f\sigma_8^{\mathrm{fx.}\,\alpha\mathrm{s}}$ should have an error of 6.3%. Neveux et al. made use of 1000 EZmocks to estimate the covariance matrix and the observational systematic errors that we reported above. From these mocks catalogues, they recovered $f\sigma_8 = 0.467$, with an average fractional error of 0.059, which is shown with a brown cross in Figure 2.4.

In addition, we also run our Fisher-code for the eBOSS DR14 Quasar sample, consisting of $148,659$ galaxies with redshifts $0.8 < z < 2.2$ and an effective redshift of $z_{\mathrm{eff}} = 1.52$, and a footprint of $2,113\text{deg}^2$. The BAO measurement for this sample showed a 3.8% fractional error on D_V, considering that the systematic errors are negligible for this sample (Ata et al. [120]). The RSD measurement fitting the CLPT+GS model for scales larger than $s_{\rm min} = 20\,h^{-1}\,\text{Mpc}$ ($k_{\rm max} \sim 0.18\,h\,\text{Mpc}^{-1}$) showed a 16.4% fractional statistical error on $f\sigma_8^{\rm mg.\,\alpha s}$. After taking systematic effects into account, the combined error rose to 18.5%. From the covariance matrix provided, this translates to a 15.4% error on $f\sigma_8^{\rm fx.\,\alpha s}$ (Table 9 of Zarrouk et al. [75], stat. error). Zarrouk et al. also fitted for the galaxy bias and found that $b\sigma_8 = 1.038$, or $b(z_{\rm eff} = 1.52) = 2.6$. In our Fisher code, we re-scaled the Croom formula by a factor of 1.1 to match this bias.

2.2.7 WiggleZ Dark Energy Survey

The WiggleZ Dark Energy Survey was undertaken using the 3.9-meter Anglo-Australian Telescope (AAT; Drinkwater et al. [121]). This survey observed approximately $240,000$ ELGs over the redshift range $0.2 < z < 1.0$ from 2006 to 2011. We consider the final data release that covers $816\ \text{deg}^2$ in the sky in six regions, and contains $158,741$ ELGs. Following the analyses of Blake et al. [67] and Kazin et al. [122], we first combine these six regions together and divide the galaxies into three partially overlapping redshift bins $0.2 < z_{\rm near} < 0.6$, $0.4 < z_{\rm mid} < 0.8$, and $0.6 < z_{\rm far} < 1.0$, and then analyze each catalogue separately. Throughout our Fisher analysis, we assume that the galaxy bias is $b_{\rm ELG} = 0.8/D(z)$, to match the effective biases as assumed when performing reconstruction as in Kazin et al., in each redshift bin ($b_{\rm eff} = 1.0$, 1.1, and 1.2 in Near, Mid, and Far, respectively)

Kazin et al. [122], found that after applying the reconstruction method by Padmanabhan et al., D_V has an uncertainty of 4.8%, 4.5% and 3.4% at effective redshifts $z_{\rm eff}^{\rm Near} = 0.44$, $z_{\rm eff}^{\rm Mid} = 0.60$, and $z_{\rm eff}^{\rm Far} = 0.730$, respectively. Additionally, Blake et al. [67], fitted with the RSD model introduced by Jennings et al. [88] (J+11), and for $k < 0.2\,h\,\text{Mpc}^{-1}$ found a fractional error on $f\sigma_8^{\rm mg.\,\alpha s}$ of 19.4%, 16.1%, and 16.4% for the near, middle, and far redshift slices, respectively. When fixing the dilation parameters, the fractional error bars reduce to $f\sigma_8^{\rm fx.\,\alpha s} = 13.2\%$, 10.9%, and 8.7%.

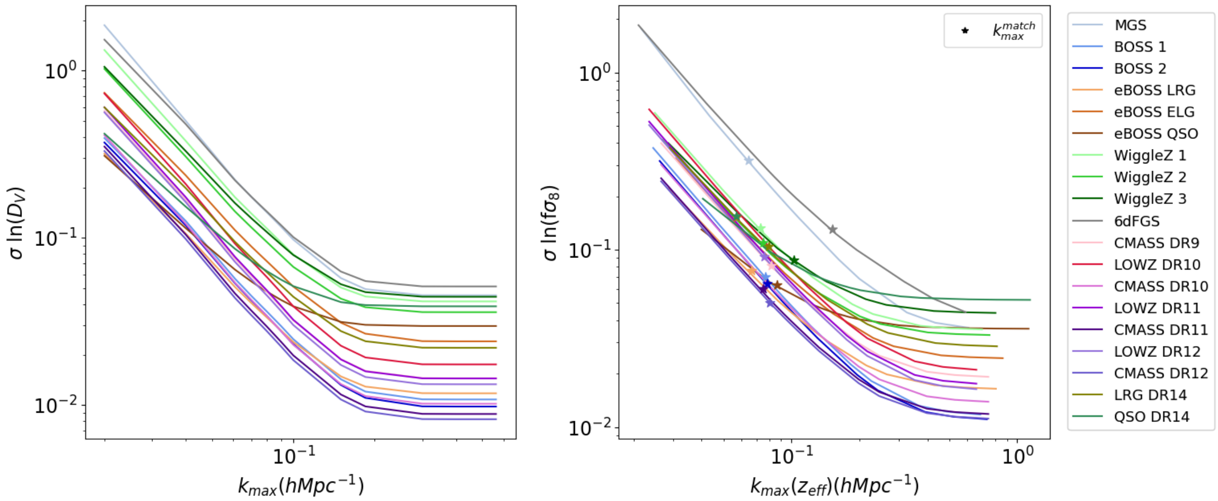

Figure 2.1: The Fisher-based predicted fractional error on D_V (*left*) and $f\sigma_8$ (*right*) plotted against $k_{\rm max}(z = z_{\rm eff})$ for different surveys. Note that in contrast to the $f\sigma_8$ error, the D_V error converges to a constant at $k \gtrsim 0.3\,h\,{\rm Mpc}^{-1}$. The stars on the right panel indicate the $k_{\rm max}$ at which the Fisher prediction and the experiment are equal.

2.3 Results

We have performed a Fisher matrix analysis to predict BAO and RSD errors for the surveys introduced in Section 2.2, matching the parameters assumed for the Fisher calculations as closely as we can to the parameters of the surveys. The final results of our calculations on the fractional error of the cosmological parameters, D_M, D_H, D_V, and $f\sigma_8$, for each survey's final data release and for BOSS and eBOSS intermediate data releases, are presented in Table 2.2 and Table 2.3, respectively (abbreviated as F.). For comparison, we also present the errors of D_M, D_H, D_V from the BAO measurements published in the most recent analyses of the data, with errors calculated using sets of mock catalogues (abbreviated as O. for observed). In addition, we present the fractional errors of $f\sigma_8$ from the most recent RSD analysis of the data, when dilation parameters are marginalized over (abbreviated as Mg. αs), and when they were held fixed (abbreviated as Fx. αs). The RSD predictions depend strongly on the value of $k_{\rm max}$ adopted, which is the upper limit of the integration in Eq. 2.2. In the penultimate rows in Table 2.2 and 2.3, we present $k_{\rm max}^{\rm fid} = 0.1/D(z_{\rm eff})$, matching the assumptions previously made for many surveys (e.g. [36]), and $k_{\rm max}^{\rm match}$, that we will describe in detail later in this section.

In these tables, the effective redshift, $z_{\rm eff}$, is the weighted mean redshift, using weights $w_{\rm FKP} = (1 + \bar{n}P_0)^{-1}$ from Feldman et al. [123]. The effective area, $A_{\rm eff}$, is the survey's area as reported from its corresponding clustering catalogue documentation. The effective volume is calculated from the equation below,

$$V_{\rm eff} = V_{\rm survey} \sum_{i=1}^{N_Z} \left(\frac{n(z_i)P_0}{1 + n(z_i)P_0} \right)^2 , \tag{2.11}$$

where P_0 is the amplitude of the power spectrum at $k \sim 0.15\,h\,{\rm Mpc}^{-1}$. Its value for 6dFGS, MGS, BOSS DR12 and eBOSS LRGs is $10,000$, for eBOSS ELGs is $4,000$, for eBOSS Quasars is $6,000$, for BOSS DR9-12 is $20,000$ and for WiggleZ is $5,000$, all in units of h^{-3} Mpc^3.

For the combined 6dFGS and MGS samples, we obtain a 3.1% accuracy on D_V, very similar to the 3.2% error reported by Carter et al. [95] for the combined samples. In Table 2.2, only the constraints recovered from the 6dFGS sample are reported, since we are interested in the surveys separately. Note that 6dFGS and MGS do not geometrically overlap more than 3%, allowing their Fisher matrices to be added directly to obtain the final constraint at low redshift. Additionally, Alam et al. used the combined CMASS+LOWZ BOSS catalogue over the redshift range $0.2 < z < 0.75$, split into three partially overlapping catalogues in redshift covering $0.2 < z < 0.5$, $0.4 < z < 0.6$, and $0.5 < z < 0.75$ and measured the BAO and RSD parameters in each of these bins separately. In this chapter we did not analyze the high redshift bin separately since we combined the high redshift BOSS LRGs with the eBOSS LRGs to match the catalogue used by Bautista et al. These two samples geometrically overlap in the eBOSS footprint, and that is why we needed to calculate the overlapping area and the non-overlapping area separately and add the Fisher matrices to obtain the errors reported in Table 2.2.

In the following, we briefly describe the key results that our analysis implies.

- From the left panel in Figure 2.2, we are able to confirm that there is a linear relationship between the fractional error on D_V and $V_{\rm eff}^{-1/2}$, as expected from Eq. 2.6, both for observations and predictions. The Fisher-based D_V errors were calculated under the assumption of $k \gtrsim 0.5\,h\,{\rm Mpc}^{-1}$. From the left panel in Figure 2.1, we found that $\sigma_{\ln D_V}$ is not sensitive to the choice of $k_{\rm max}$ for $k \gtrsim 0.3\,h\,{\rm Mpc}^{-1}$ (Section 2.1.3 for more detail on the $k_{\rm max}$ choice). Furthermore, we obtained similar slopes for the Fisher analysis and observations, showing that the Fisher method works well, and that observational methods are able to extract information reaching close to the maximum possible. In addition, Figure 2.3 supports this claim by revealing a linear relationship, with a slope very close to unity, between the measured D_V error and the Fisher-predicted D_V error.

- Table 2.2 and 2.3 show that our Fisher prediction of fractional error on the volume averaged distance from the BAO measurements, σ_{D_V}/D_V, deviates less than 35% from analyses that use similar techniques, including reconstruction and covariance matrices calculated using mock catalogues. We consider this to be an exceptionally positive result for the field of BAO analyses, showing that current methods are extracting all of the available signal (i.e. reconstruction is working as well as expected in Seo & Eisenstein, with a 50% drop in Σ_s). Better reconstruction methods (e.g. [81, 82, 83]) would be able to improve the BAO constraints by reducing the non-linear damping.

- The picture is worse for RSD-based measurements: If we assume that $k_{\rm max} = k_{\rm max}^{\rm fid}$, the $f\sigma_8$ fractional error is not very well estimated by the Fisher matrix analysis, and it shows a lower correlation with the effective volume than D_V (Figure 2.2; right panel). In our baseline Fisher calculation, we assume that the dilation parameters are fixed. Therefore, we choose the $f\sigma_8$ errors taken from observations to be those for which the dilation parameters D_M and D_H were fixed. We have been able to adjust most of the measurements we have considered to match the baseline assumed for the Fisher predictions. Whether or not we marginalise has a big effect on the results, and so it is important to match Fisher with observations.

- The $f\sigma_8$ error is highly dependent on the choice of maximum k to which we integrate to make Fisher predictions and hence from which we can recover information. Decreasing $k_{\max}$ weakens the predicted constraints on $f\sigma_8$ (Figure 2.1; right panel). For most of the catalogues used in this work, we calculated the $k_{\max}^{\text{match}}$ that, when used in the Fisher analysis, gives an $f\sigma_8$ error that matches with that of the experiments. The average of $k_{\max}^{\text{match}}$ over these catalogues is about $0.08 \pm 0.01\, h\, \text{Mpc}^{-1}$, with remarkably little scatter around this value. This should be interpreted as the amount of linear information that can be recovered from these data.

  If the theoretical arguments that led to expecting $k_{\max}^{\text{fid}}$ to increase at higher redshifts hold true, then the data analyses are missing significant information, particularly at high redshift. Alternatively, the theoretical arguments are wrong, possibly because the high bias of the samples analysed at high redshift shifts the non-linear scale to lower k. Either way, this is clearly an area where improved modeling is required (e.g. [124, 125, 126, 127, 128, 129, 130]).

- The right and left panels of Figure 2.4 show a consistent story. The left panel shows that the ratio of Fisher-predicted to observed $f\sigma_8$ error generally decreases to higher redshift (note that the samples are arranged from low to high redshift). The right hand panel shows that to match the observed information, we need $k_{\max}^{\text{match}}$ to stay fixed, while $k_{\max}^{\text{fid}}$ increases with redshift. The quasars are least consistent with this trend, with a relatively better agreement between Fisher and observations, but a strong change in $k_{\max}$. Figure 2.1 explains why this is: it shows that, for the low galaxy density of the quasar sample, there is increasingly little information on small scales due to the high shot noise. A large value of $k_{\max}^{\text{fid}}$ brings in less expected information (the green and brown curves are flatter, showing that for eBOSS DR14 and DR16 QSO information saturates quickly). This makes it even more interesting that, for all samples, the information recovered on $f\sigma_8$ is that predicted by the Fisher analysis to a consistent $k_{\max}^{\text{match}}$, despite large differences in shot noise, bias, and redshift.

- Our baseline results are presented assuming that the dilation parameters are fixed. We have also considered the alternative of marginalizing over unknown dilation parameters, using the sample itself, predominantly through the BAO signal to constrain these. We compare this alternative procedure for both the data and the Fisher matrix. In general, we find a better agreement between the Fisher and data for this procedure: comparing with the case of fixed dilation parameters shows that fixing the αs does not constrain $f\sigma_8$ as much in the data as in the Fisher. We suggest that the reason for this is that when modeling the data we have other parameters fitted (e.g.

shot noise, nonlinear bias parameters), and so our $f\sigma_8$ errors assuming fixed dilation do not reach their theoretical minima. That is, for the Fisher calculation, we reach a precision when we fix the dilation parameters that goes beyond that achievable in the data for other reasons.

Marginalising over the dilation parameters leads to more scatter in the ratio of the Fisher-based error on $f\sigma_8^{\mathrm{mg.}\,\alpha\mathrm{s}}$ to the data error. We also find a small shift in the value of $k_{\mathrm{max}}^{\mathrm{match}}$ required to match Fisher and data: marginalising over the dilation parameters, we find $k_{\mathrm{max}}^{\mathrm{match}} = 0.09 \pm 0.02\,h\,\mathrm{Mpc}^{-1}$. The increased scatter leads to an error on $k_{\mathrm{max}}^{\mathrm{match}}$ of $0.02\,h\,\mathrm{Mpc}^{-1}$ which is twice as large for fixed dilation parameters. This can be seen by eye comparing Figure A.1 to Figure 2.4. This is likely because in the data, imperfect measurement of the BAO peak adds an extra source of scatter in the marginalized $f\sigma_8$ errors. Hence our fiducial comparison uses $f\sigma_8$ errors with fixed dilation parameters, which are thus less noisy. In summary, our conclusion remains unchanged when considering $f\sigma_8^{\mathrm{mg.}\,\alpha\mathrm{s}}$; we still do not see the error decrease to high redshift, as one would naively expect. The exact prescription we use for marginalising over the dilation parameters is presented in Appendix A.

- By considering the average measurement recovered from mock catalogues, we are able to remove the statistical error from the measurements: i.e. the actual observation is only one realization of what could have happened in that particular region of the universe, and therefore its constraints can depend on how lucky the experiment was. For the MGS, eBOSS LRG, eBOSS ELG, and eBOSS Quasar experiments, the teams created 1000 mock catalogues and released the results of fitting the models to them, finding an $f\sigma_8$ error of 25.0%, 8.8%, 11.5%, and 5.9%, respectively. We plotted the ratio of Fisher forecast to the $f\sigma_8$ error recovered from both observations and mocks, if available, in the left panel of Figure 2.4. We see that the trends seen between Fisher predictions and measurements are well matched between data and mocks. This suggests that the trends are due to the methodology (particularly the model used to fit to the data) rather than statistical fluctuations.

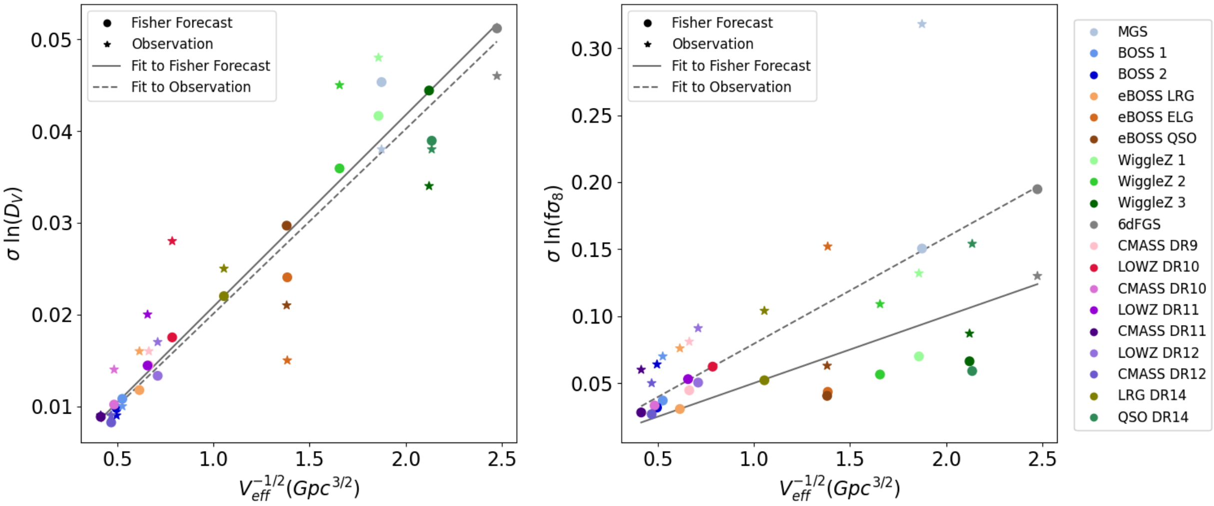

Figure 2.2: D_V fractional error as measured from the BAO position plotted against the effective volume $V_{\rm eff}^{-1/2}$ for different surveys (left panel). A clear trend is seen, with the slopes of the linear fit to the Fisher and observational errors being 0.022 and 0.020, respectively. The measured RSD constraints show a weaker correlation with $V_{\rm eff}^{-1/2}$.

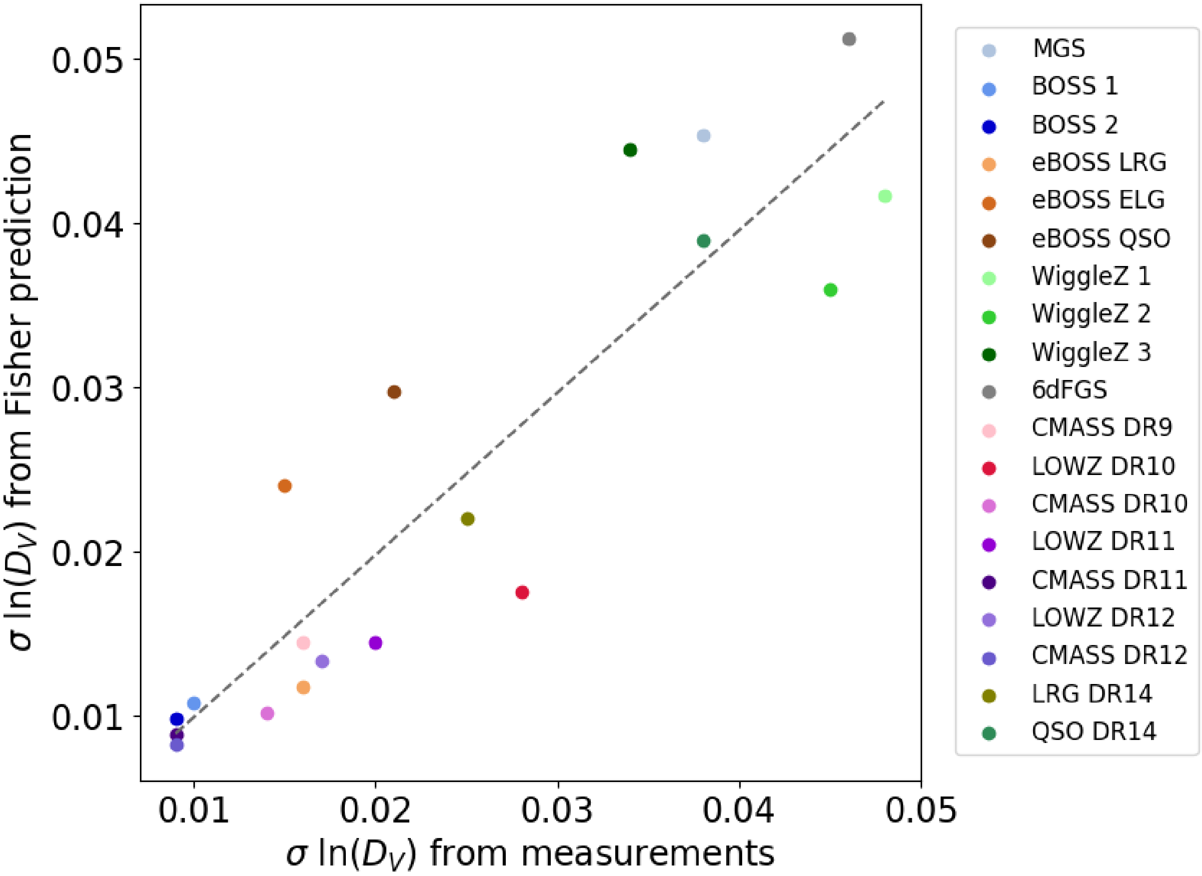

Figure 2.3: The Fisher-based predicted fractional error on D_V plotted against the fractional error recovered from BAO-only analysis. The slope of the fitted line is 1.1, which implies that the Fisher prediction and the BAO measurements are in good agreement.

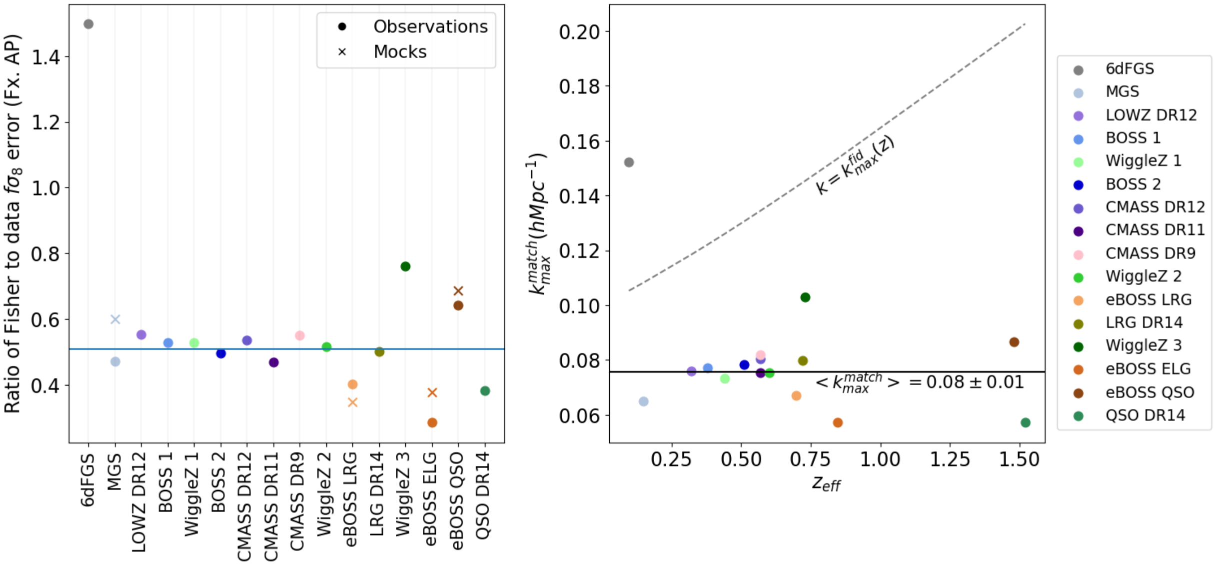

Figure 2.4: *Left*: The difference between Fisher-based prediction $f\sigma_8$ error and observational $f\sigma_8^{\mathrm{fx.}\,\alpha\mathrm{s}}$ error is plotted for each survey. The x markers indicate mock errors instead of the errors obtained from observations. *Right*: We have adjusted the $k_{\max}$ in order to make Fisher predictions match with the experiments. The dashed line represents the fiducial value of $k_{\max} = 0.1/D(z)\, h\,\mathrm{Mpc}^{-1}$. Note that the fiducial cosmology used to draw this line is the same as the BOSS cosmology. (WiggleZ Near, Mid, and Far redshift slices are shortened as 1, 2, and 3)

2.4 Discussion

We have performed a Fisher analysis for 19 different survey catalogues to obtain the constraints on the co-moving angular diameter distance, D_M, the Hubble distance, D_H, and the growth rate of structure $f\sigma_8$, from BAO and RSD analyses. Furthermore, the statistical errors derived were compared for each catalogue to that recovered in recent analyses modelling the correlation function (or the power spectrum). We only selected studies that adopted similar methodologies, using covariance matrices for the 2-point measurements created using mock catalogues, and for BAO measurements using a basic reconstruction method (except for the quasar samples where reconstruction does not improve the BAO signal).

Our Fisher-based BAO and RSD predictions are well matched to those from Zhao et al. [36] for the eBOSS survey if we correct for the difference between predicted and actual survey parameters (area, galaxy redshift distribution, galaxy bias). The differences between predicted and actual survey details make less than a 60% change on the measured errors. By comparing the final measurements with Fisher predictions using the actual eBOSS details, we find that the Fisher predictions and observational results are within 30% of each other for all samples for errors on D_V. In contrast, for RSD we find that in general, the errors predicted from our Fisher analysis are about 50% of those of the observations.

Using Fisher-based predictions for the BAO constraints on the BOSS Near sample ($0.2 < z < 0.5$), Dawson et al. [28] predicted a 1% error on D_M and a 1.8% error on D_H, and from their results it can be inferred that the error on D_V is about 1.0%, which is in a good agreement with our Fisher-prediction for BOSS DR12 Near sample. After the BOSS DR9 was released, Font-Ribera et al. [35] performed a Fisher matrix analysis and found 7.0% fractional error on $f\sigma_8$ and 1.15% fractional error on D_V for DR9 CMASS.

More accurate RSD techniques allow for extracting RSD information to smaller scales. For instance, Reid et al. [131] were able to extend the RSD analysis to scales of $0.8\,h^{-1}$ Mpc in configuration space, using an HOD to model the small-scale RSD, and found 2.4% accuracy on $f\sigma_8$ in the BOSS CMASS DR10 sample. This is a factor of 1.4 smaller than our Fisher matrix prediction using $k_{\rm max}^{\rm fid} = 0.132$. For the Fisher-based analysis to be as small as this error, we would need to include linear information to $k_{\rm max}^{\rm match} = 0.19\,h\,{\rm Mpc}^{-1}$. Additionally, using small scale RSD modelling, Lange et al. [132] extracted the RSD information down to scales of about $0.4\,h^{-1}\,\mathrm{Mpc}$ for two volume-limited catalogues created from the BOSS LOWZ sample in the North Galactic Cap. They found a precision of 5.1% and 5.8% on $f\sigma_8$ at effective redshifts of 0.25 and 0.4, respectively. Our Fisher code, when run on their catalogue with the fiducial $k_{\mathrm{max}} = 0.114$ and $0.123\ h\,\mathrm{Mpc}^{-1}$, yields an error of 11.8% and 9.8% on $f\sigma_8$. This implies that $k_{\mathrm{max}}^{\mathrm{match}}$ should be $0.23\,h\,\mathrm{Mpc}^{-1}$ and $0.14\,h\,\mathrm{Mpc}^{-1}$, respectively. This shows that improved small-scale modelling can extract information to smaller scales than the apparently-universal $k_{\mathrm{max}} = 0.08\,h\,\mathrm{Mpc}^{-1}$ we found for the large-scale analyses. However, ensuring that the RSD modelling remains unbiased on very small scales remains a challenge.

Table 2.2: The Fisher forecast (shortened as F.) errors for D_M, D_H, D_V, and $f\sigma_8$ compared to the errors from the BAO and RSD measurements (shortened as O.). The RSD rows show $f\sigma_8$ errors from observations with and without marginalisation over the dilation parameters (Mg. for marginalized and Fx. for fixed). For 6dFGS, the sample used for RSD has slightly different b_{eff} and z_{eff} from the sample used for BAO; in the Fisher forecast we use b_{eff} and z_{eff} from ref. [95], for consistency. The BOSS analysis have used 4 different RSD models that were briefly described in the text. The eBOSS LRG sample reported in this table is the combined eBOSS LRG sample covering 4242 deg^2 with the BOSS DR12 sample at high redshift ($0.6 < z < 1.0$), covering 9494 deg^2. We also display the $k_{\text{max}}^{\text{obs.}}$ of the observations, the fiducial Fisher k_{max}, and $k_{\text{max}}^{\text{match}}$; the RSD model used; whether the fit was performed in configuration (s) or Fourier (k) space; and the references.

	6dFGS	MGS	BOSS		eBOSS			WiggleZ		
			Near	Mid	LRG	ELG	QSO	Near	Mid	Far
z_{eff}	0.097	0.15	0.38	0.51	0.698	0.845	1.48	0.44	0.600	0.73
$A_{\text{eff}}(deg^2)$	17000	6813	9329	9329	4242	727	9494	816	816	816
$V_{eff}(Gpc^3)$	0.13	0.28	3.40	4.08	2.65	0.52	0.52	0.29	0.36	0.22
b_{eff}	1.65	1.5	2.03	2.13	2.2	1.52	2.33	1.0	1.1	1.2
Fractional errors from the BAO analysis (in percent)										
D_M (O.)			1.5	1.4	1.6	4.3	2.5			
D_M (F.)	8.0	6.4	1.5	1.3	1.7	3.6	3.4	6.9	6.0	7.5
D_H (O.)			2.7	2.3	2.5	9.0	4.0			
D_H (F.)	16.1	13.8	3.1	2.8	3.2	6.3	5.0	11.3	9.5	11.4
D_V (O.)	4.6	3.8	1.0	0.9	1.6	2.7	1.5	4.8	4.5	3.4
D_V (F.)	5.8	4.9	1.1	1.0	1.2	2.5	3.0	4.6	3.9	4.9
BAO ref.	[95]	[98]	[64]	[64]	[65]	[116]	[66]	[122]	[122]	[122]
Fractional errors from the RSD analysis (in percent)										
$f\sigma_8$(O.Mg.)		40.5	7.8	7.6	7.9	23.6	9.3	19.4	16.1	16.4
$f\sigma_8$(O.Fx.)	13.0	31.8	7.0	6.4	7.6	15.2	6.3	13.2	10.9	8.7
$f\sigma_8$(F.Fx.)	19.5	15.0	3.7	3.2	3.1	4.4	4.0	7.0	5.6	6.6
k_{max} for the RSD modeling										
$k_{\text{max}}^{\text{obs.}}$	0.23	0.14	0.17	0.17	0.16	0.16	0.24	0.2	0.2	0.2
$k_{\text{max}}^{\text{fid.}}$	0.11	0.11	0.12	0.13	0.14	0.15	0.20	0.12	0.13	0.14
$k_{\text{max}}^{\text{match}}$	0.16	0.06	0.08	0.08	0.07	0.06	0.08	0.07	0.07	0.11
RSD Model	Sc.	CLPT	4 Models		TNS&CLPT+GS			J+11		
RSD space	s	s	k/s	k/s	s	k/s	k/s	k	k	k
RSD ref.	[96]	[63]	[64]	[64]	[65]	[116]	[66]	[67]	[67]	[67]

Table 2.3: Same as Table 2.2, but including intermediate data releases of BOSS and eBOSS. LOWZ and CMASS are shortened as LZ and CM.

	BOSS	BOSS		BOSS		BOSS		eBOSS		eBOSS	
	BOSS	DR10		DR11		DR12		DR14		DR16	
	DR9	LZ	CM	LZ	CM	LZ	CM	LRG	QSO	LRG	QSO
z_{eff}	0.57	0.32	0.57	0.32	0.57	0.32	0.57	0.72	1.52	0.698	1.48
$A_{\text{eff}}(deg^2)$	3275	5156	6161	7341	8377	8337	9376	1845	2113	9494	4699
$V_{eff}(Gpc^3)$	2.47	1.77	4.67	2.53	6.38	2.18	5.03	0.91	0.22	2.65	0.52
b_{eff}	2.0	1.8	2.11	1.85	2.05	1.9	2.1	2.0	2.63	2.2	2.33
Fractional errors from the BAO analysis (in percent)											
D_M(O.)	2.0		1.9		1.4	2.2	1.3			1.6	2.5
D_M(F.)	2.2	2.7	1.6	2.2	1.4	2.0	1.3	3.2	5.2	1.7	3.4
D_H(O.)	3.8		5.0		3.5	5.9	2.9			2.5	4.0
D_H(F.)	4.4	5.4	3.1	4.5	2.7	4.2	2.5	5.9	7.8	3.2	5.0
D_V(O.)	1.6	2.8	1.4	2.0	0.9	1.7	0.9	2.5	3.8	1.6	1.5
D_V(F.)	1.6	2.0	1.1	1.6	1.0	1.5	0.9	2.2	3.9	1.2	3.0
BAO ref.	[24]	[101]	[101]	[101]	[101]	[108]	[108]	[114]	[120]	[65]	[66]
Fractional errors from the RSD analysis (in percent)											
$f\sigma_8$(O.Mg.)	14.6	23.3	12.8	20.8	9.9	15.7	8.6	29.2	16.4	7.9	9.3
$f\sigma_8$(O.Fx.)	8.1				6.0	9.1	5.0	10.4	15.4	7.6	6.3
$f\sigma_8$(F.Fx.)	4.5	6.2	3.3	5.3	2.8	5.0	2.7	5.2	5.9	3.1	4.0
k_{max} for the RSD modeling											
$k_{\text{max}}^{\text{obs.}}$	0.14	0.09	0.09	0.09	0.14	0.17	0.17	0.13	0.18	0.16	0.24
$k_{\text{max}}^{\text{fid.}}$	0.13	0.12	0.13	0.12	0.13	0.12	0.13	0.15	0.20	0.14	0.20
$k_{\text{max}}^{\text{match}}$	0.08				0.07	0.08	0.08	0.08	0.07	0.07	0.08
RSD Model	R11				R11	TNS		CLPT +GS		TNS & CLPT	
RSD space	s	s	s	s	s	k	k	s	s	s	k/s
RSD ref.	[100]	[102]	[102]	[102]	[103]	[104]	[104]	[115]	[75]	[65]	[66]

Chapter 3

Potential contaminants in surveys from the Roman space telescope

This work was published as [1] co-authored with Elena Massara and Will Percival. I undertook the BAO analysis, built the theoretical model, wrote the code, and led the writing of the paper with input from them.

3.1 Introduction

Space-based Large Scale Structure (LSS) spectroscopic surveys made possible by the Roman Space Telescope [133] and Euclid [134] missions will soon be available. These surveys will make use of slitless spectroscopy to measure galaxy redshifts meaning that, while they have the potential to constrain the cosmological parameters with sub percent levels of accuracy, this requires a thorough understanding of potential sources of systematic error arising from the slitless method. One possible systematic effect, that we study in this chapter, is the contamination of the sample by interlopers resulting from line confusion.

To estimate the redshifts of a set of galaxies using slitless spectroscopy, we measure the wavelengths of one or more emission lines for each. In this chapter we will primarily be concerned with samples where only one emission line is used to estimate the redshift. Generally, emission lines with different rest-frame wavelengths λ_1 and λ_2, from two different galaxies with true redshifts $z_1 = \lambda_{\rm obs}/\lambda_1 - 1$ and $z_2 = \lambda_{\rm obs}/\lambda_2 - 1$, can appear at the same observed wavelength, $\lambda_{\rm obs.}$. The measured redshift for a galaxy given only the observed position of this single line will depend on the rest-frame wavelength assumed. In the presence of a secondary emission line, one can distinguish between different options. However, if we are measuring redshifts from a single emission line, we are prone to line misidentification, if we assume, for a sample of galaxies, that the observed line has the same rest-frame wavelength for all galaxies. The galaxies in the sample for which the lines are misidentified resulting in them being assigned the wrong redshift, are called interlopers. We refer to the galaxies whose observed emission line matches the assumed rest-frame wavelength when measuring redshifts as the target galaxies.

For Roman, for example, it is likely that many redshifts will be measured using 2 or more emission lines [40]. At $2 < z < 3$, [O III] is the primary line for Roman observations, which is actually a doublet. Resolving this doublet as two separate lines, which is possible at given the resolution of Roman, or observing a secondary line from [O II] emission would allow a secure redshift to be measured. However, to provide a bonus sample to higher number densities, it will be useful to analyse galaxies where only one unresolved line is observed, assumed to be [O III], but where this identification is less secure. For this, we will have interlopers, where the Hβ line is mistaken for [O III]. The increased size of this bonus sample will help reduce the statistical errors on measured cosmological parameters, at the cost of increasing the systematic errors. It is these systematic errors, and methods to mitigate them, that we consider in this chapter.

In general, there are three different ways that a catalogue can be contaminated:

1. First, due to noise spikes being misidentified as emission lines. The noise is uncor-

related with all the other galaxies, and has a distribution different from that of the true observed lines. Thus, this population of contaminants Poisson samples a volume that has a window different from that of the target galaxy population. It can trivially be corrected in a clustering measurement as it is absorbed into (and is cancelled by) part of the expected density (often quantified by a random catalog) and simply adds to the shot noise and changes the amplitude of the signal measured.

2. Second, misidentified emission lines can arise from interloper galaxies displaced by a large radial distance. In this case, correlations with the target galaxy population are small and we only need to model the auto-correlation of the interloper sample (e.g. [135], [136], and [137]). Because the displacement is large, there is a significant change in $H(z)$ between the true redshift of the interlopers and the incorrect redshift inferred, such that the Baryon Acoustic Oscillation (BAO) signal in the auto-correlation of the interlopers is shifted with respect to its true value. This needs to be included in any analysis but, as the shift is known from the line emission wavelengths, this contribution to the clustering of the contaminated sample can be easily modeled provided the fraction of interlopers is known.

3. The third class of contaminant is a more pernicious type of interloper, which is one only shifted by a small radial displacement by the incorrect rest-frame wavelength assignment. Such interlopers will be correlated with other such objects *and* with the target galaxy sample. This type of interloper can occur for samples obtained using the Roman Space Telescope at high redshifts, where the target is the primary [O III] line, and Hβ line is the source of interlopers. The impact of these interlopers on the BAO peak position was studied by [138]. They showed that misidentifying Hβ line as [O III] line in an Emission Line galaxy will lead to underestimating its distance by $\sim 90\,h^{-1}\,\mathrm{Mpc}$. This would distort the shape of the galaxy correlation function and therefore introduce a shift in the BAO peak position. We call this class of interlopers, which are displaced by $\lesssim 150\,h^{-1}\,\mathrm{Mpc}$, "small-displacement" interlopers (see Section 3.5).

We focus on the third class of contaminant. Following [138], we present a model for the monopole and the quadrupole moments of the correlation function of a Roman-like catalogue, with an [O III] target line sample contaminated by Hβ interlopers. With this model, we investigate how to find an unbiased estimation of the isotropic and anisotropic dilation parameters α and ϵ from the BAO signal, as well as the fraction of interlopers f_{i}. Our method is based on standard BAO modeling, additionally allowing for the interlopers. The model correlation function has two terms: The galaxy auto-correlation that we estimate using CAMB [139], and a non-negligible cross-correlation between the galaxies and

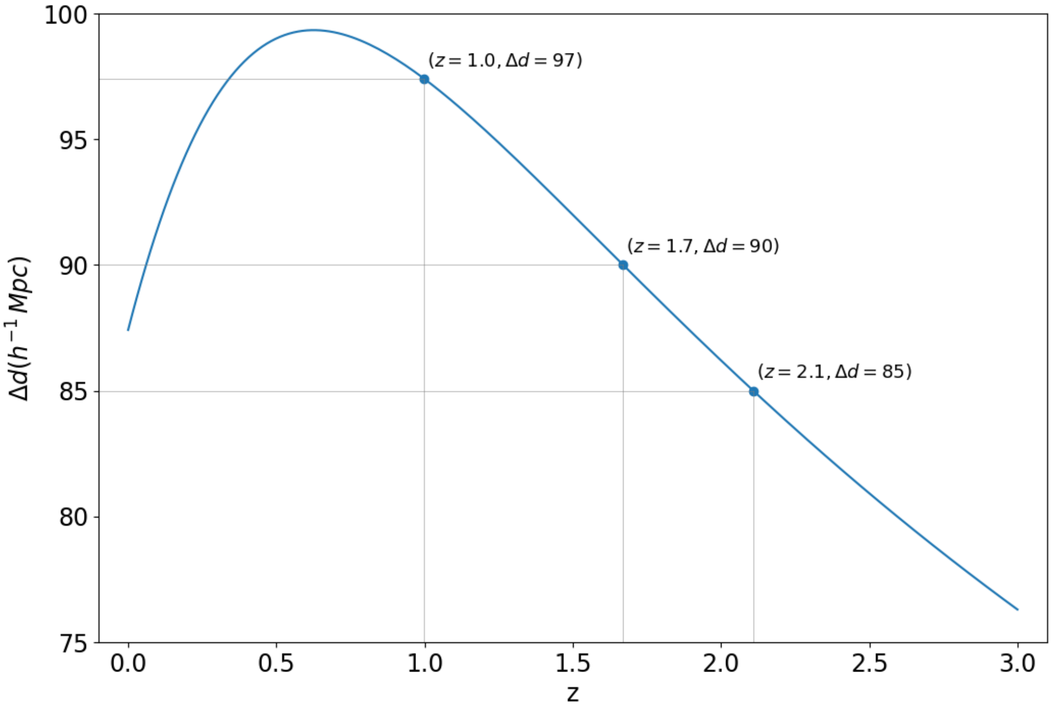

Figure 3.1: Displacement of interlopers as a function of their true redshift as shown in Eq. 3.2.

the interlopers that we consider a number of ways of estimating. If we can measure this from the contaminated auto-correlation, or use another way of accurately calibrating this statistic, our pipeline gives an unbiased estimation of all the three parameters. If we do not take into account the interlopers, the measurements would be highly biased.

The plan of our chapter is as follows: In section 3.2, we derive the interloper shift value. In section 3.3, we describe simulations that were used for our analysis. In section 3.4, we present our model for the correlation function of a catalogue contaminated by a same redshift fraction of interlopers. We show the outcomes of our pipeline in section 3.5. We finally conclude in section 3.6.

3.2 Displacement

Let us assume that in a survey, potential interlopers are at redshift z^{true}, and they emit a primary emission line with rest-frame wavelength $\lambda^{\text{true}}_{\text{emit}}$, that is observed at wavelength λ_{obs}. The observed wavelength can be misidentified for another photon as if it was emitted with rest-frame wavelength $\lambda^{\text{false}}_{\text{emit}}$ at redshift z^{false}. This redshift misidentification would effectively lead us to a wrong estimation of the comoving proper distance to the galaxies by Δd:

$$\Delta d = d^{\text{true}} - d^{\text{false}} = \int_{z^{\text{false}}}^{z^{\text{true}}} \frac{c dz}{H(z)} \tag{3.1a}$$

$$\approx \frac{c}{H(z^{\text{true}})}(z^{\text{true}} - z^{\text{false}}) \,. \tag{3.1b}$$

$$\approx \frac{c}{H(z^{\text{true}})}\left[1 - \frac{\lambda^{\text{true}}_{\text{emit}}}{\lambda^{\text{false}}_{\text{emit}}}\right](1 + z^{\text{true}}) \,. \tag{3.1c}$$

In this chapter we consider Hβ interlopers misidentified as [O III] emitters. While [O III] is a doublet, here we assume that Hβ is misidentified as the primary line in the doublet at $\lambda^{\text{OIII}}_{\text{false}} = 500.7\,\text{nm}$, rather than the secondary line at $\lambda^{\text{OIII}}_{\text{false}} = 495.9\,\text{nm}$. The rest-frame wavelength of Hβ is $\lambda^{\text{H}\beta}_{\text{true}} = 486.1\,\text{nm}$, leading to an offset between the true and wrongly inferred interloper comoving position equal to

$$\Delta d \approx 87.41 \frac{1 + z^{\text{true}}}{\sqrt{\Omega_\Lambda + \Omega_{\text{m}}(1 + z^{\text{true}})^3}} \; h^{-1}\,\text{Mpc}. \tag{3.2}$$

Figure 3.1 displays the distance Δd as a function of the true galaxy redshift and with the parameters Ω_Λ and Ω_{m} evaluated at the cosmology of the simulations used in this chapter and described in Section 3.3. In that cosmology, the displacement Δd is equal to $97\,h^{-1}\,\text{Mpc}$ at $z = 1$ (the redshift of the N-body snapshots considered in this work), and $90, 85\,h^{-1}\,\text{Mpc}$ at $z = 1.7, 2.1$, which are the redshifts of interest for the Roman Space Telescope.

Note that measurements stemming from rest-frame wavelength differences cannot be used as standard rulers in the same way as BAO - what is fixed is the difference in redshift, not the distance. The displacement in physical units depends on the assumed fiducial cosmology used to convert redshifts to distances not the true cosmology, and we do not have to vary the displacement when fitting different cosmological models to the data.

3.3 Simulations

In this study, our focus is on building and testing a model framework that describes the effect of interloper galaxies rather than predicting the actual expected fraction of interlopers. While some progress have been made in modelling the population of [O III] emitters (e.g., [140]), we need a thorough comparison with observations to know if we have the accuracy required. The population of Hβ emitters is less well understood. Therefore, we will use halos in place of galaxy catalogs to test our model, for simplicity. We employ the halo catalogs from $1,000$ N-body simulations of the Quijote suite [57]. These simulations have been run in a box with size $1h^{-1}$Gpc and follow the evolution of 512^3 cold dark matter particles in the fiducial cosmology of the suite, which is a flat ΛCDM cosmology with parameters $\Omega_m = 0.3175$, $\Omega_b = 0.049$, $n_s = 0.9624$, $h = 0.6711$, $\sigma_8 = 0.834$, $M_\nu = 0.0$ eV. Halos have been identified using the Friends-of-Friends algorithm with linking length parameter equal to 0.2, and only those with 20 or more cold dark matter particles have been stored in the catalog. This means that considered halos have minimum mass equal to $1.31 \cdot 10^{13} h^{-1} \mathrm{M}_\odot$.

Even though [O III] emission galaxies are the primary target at redshifts beyond $z = 1.8$ in the High-Latitude Survey of the Roman telescope, we use halo catalogs at redshift $z = 1$ to have a larger number density of objects, $\bar{n}_h = 2 \cdot 10^{-4} h^3 \mathrm{Mpc}^{-3}$, consistent with the expected [O III] mean number density in Roman between redshifts $1.8 - 2.8$ [140, 138]. At the redshift of the simulation, interlopers appear to be displaced by $97\,h^{-1}$ Mpc along the line of sight. To simulate interlopers at higher redshift, we also consider displacements equal 90 or $85\,h^{-1}$ Mpc that correspond to catalogs at redshifts $z = 1.7$ and $z = 2.1$, respectively. We build the contaminated halo catalogs by randomly selecting objects that will be interlopers and displacing them at the wrongly inferred distance along the z direction, that we assume to be the line-of-sight (hereafter, LOS). We implement four different percentages of interlopers (2, 5, 10, 15 %) and three different values for the displacement, obtaining 12 different contaminated halo catalogs for each of the initial uncontaminated ones.

We measure the correlation function from all these mocks, by making use of Nbodykit [141] adopting the Landy-Szalay estimator [54]. To build a better understanding of the problem, the monopole and quadrupole of this measured correlation function are shown in figure 3.2 and figure 3.3, respectively. In these plots, we show catalogues contaminated by different fractions of interlopers in different colours, and with different displacements in different panels: $\Delta d = 85$ (top), 90 (middle), and $97\,h^{-1}$ Mpc (bottom). The effects of the interlopers are clear to see in both moments. The amplitude of the small-scale monopole is suppressed by the presence of interlopers, and the suppression increases with the fraction of interlopers. The missing small-scales correlation is converted into larger scales, and in particular it enhances the amplitude of the correlation around the displacement scale, which is close to the BAO peak position. As a result, the BAO peak appears to be enhanced, broadened and shifted towards smaller separations. The quadupole is also modified by the interlopers: Its amplitude is enhanced on all scales with increasing interloper fraction. Moreover, it also exhibits a peak around the scales corresponding to the displacement of the interlopers, as a consequence of the increased number of interloper-target galaxy pairs along the LOS.

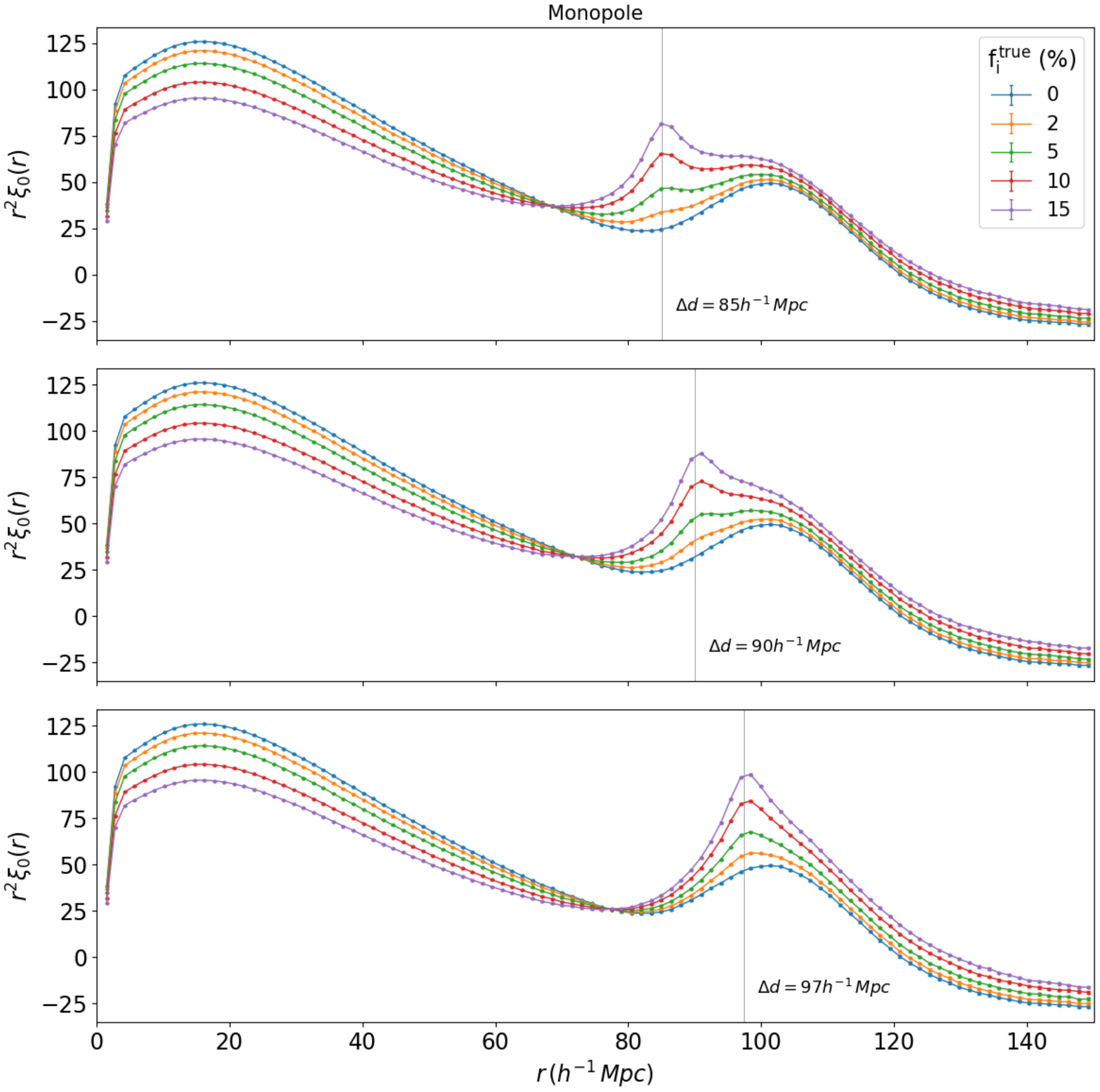

Figure 3.2: Monopole of the correlation function as calculated from the mean of 1000 mocks that are contaminated by different fractions of interlopers (different colours), and different interloper displacements: 85 (top row), 90 (middle row), and 97 h^{-1} Mpc (bottom row). As can be seen, the BAO peak is skewed towards Δd, and amplified more as the number of interlopers increase.

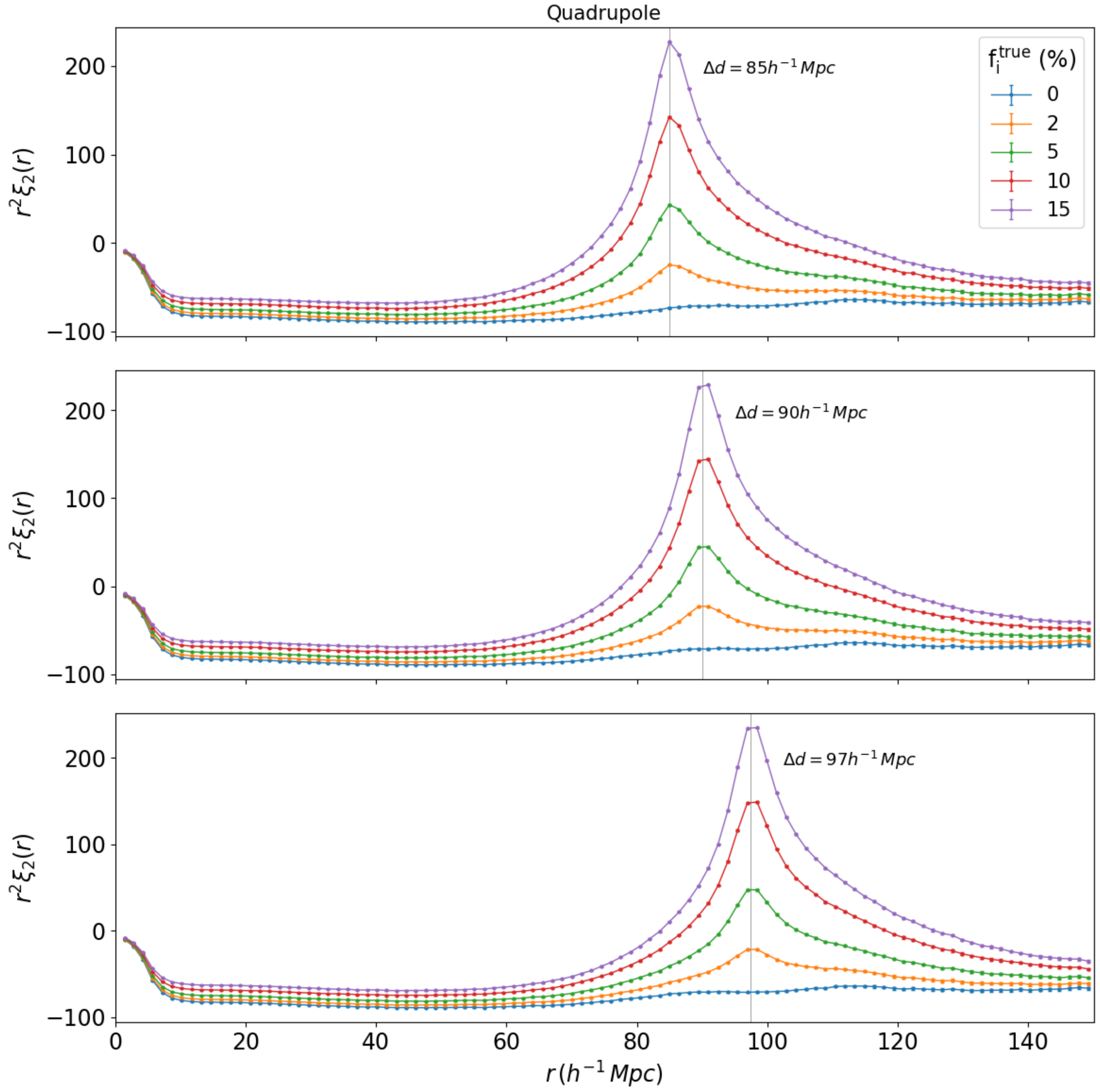

Figure 3.3: Quadrupole of the correlation function as calculated from the mean of 1000 mocks that are contaminated by different fractions of interlopers (different colours), and different interloper displacements: 85 (top row), 90 (middle row), and 97 h^{-1} Mpc (bottom row). As can be seen, the quadrupole peaks at Δd, which demonstrates the anisotropy caused by the shift of interlopers along the LOS.

3.4 Modelling the Contaminated Correlation Function

In this section, we show how to model the monopole and quadrupole moments of the correlation function for a catalogue that is contaminated by interlopers misplaced by relatively small displacements such that the interloper-galaxy cross-correlation term is not negligible. We build a model for the auto-correlation function of a contaminated catalogue in Section 3.4.1, and in Section 3.4.2 we introduce our method to estimate the interloper-target cross-correlation function. Finally, in Section 3.4.3, we discuss our completed model.

3.4.1 Correlation Function with Interlopers

We consider a catalogue contaminated by a given fraction of interlopers, $f_{\rm i}$, and define $\xi_{\rm gg}$ the auto-correlation function of the target galaxies, $\xi_{\rm gi}$ the cross-correlation between these galaxies and interlopers and $\xi_{\rm ii}$ the auto-correlation function of the interlopers. Throughout this chapter, indices "i", and "g", stand for interlopers, and galaxies respectively.

We denote the observed comoving distance of an object with $\vec{x}$: for target galaxies, this is the same as their true position, whereas for interlopers it is the wrong measured position. We denote the true position of an interloper with $\vec{y}$. Following [142], the contaminated galaxy overdensity is given by

$$\delta_{\rm t}(\vec{x}) = \frac{n_{\rm t}(\vec{x}) - \bar{n}_{\rm t}}{\bar{n}_{\rm t}} = \frac{n_{\rm g}(\vec{x}) - \bar{n}_{\rm g}}{\bar{n}_{\rm t}} + \frac{n_{\rm i}(\vec{x}) - \bar{n}_{\rm i}}{\bar{n}_{\rm t}}\,,$$

which can be simplified to

$$\delta(\vec{x}) = (1 - f_{\rm i})\delta_{\rm g}(\vec{x}) + f_{\rm i}\delta_{\rm i}(\vec{x})\,. \tag{3.3}$$

We can use this equation to calculate the contaminated correlation function at any observed separation $\vec{r} = \vec{x}_1 - \vec{x}_2$,

$$\begin{aligned}\xi(\vec{x}_1 - \vec{x}_2; f_{\rm i}) &= \langle \delta(\vec{x}_1)\delta^*(\vec{x}_2)\rangle \\ &= \langle [(1-f_{\rm i})\delta_{\rm g}(\vec{x}_1) + f_{\rm i}\delta_{\rm i}(\vec{x}_1)]\left[(1-f_{\rm i})\delta^*_{\rm g}(\vec{x}_2) + f_{\rm i}\delta^*_{\rm i}(\vec{x}_2)\right]\rangle \\ &= (1-f_{\rm i})^2\xi_{\rm gg}(\vec{r}) + f_{\rm i}^2\xi_{\rm ii}(\vec{r}) + 2f_{\rm i}(1-f_{\rm i})\xi_{\rm gi}(\vec{r})\,.\end{aligned} \tag{3.4}$$

This equation can be significantly simplified if we can make two key assumptions.

First, we assume that the displacement Δd in Eq. 3.2 between the true position of interlopers and the wrongly inferred one is a constant within a redshift bin when calculating the correlation function at a fixed cosmology. Indeed, we only consider correlation functions at separations r smaller than $150\,h^{-1}\,\mathrm{Mpc}$ in the following analysis and in this range the displacement only varies by at most 0.8% (see Figure 3.1). Therefore, we can assume that each object in the pair is displaced by the same amount. Moreover, it is commonly assumed that within a redshift bin $H(z)$ is a constant, therefore, we can assume that the displacement is fixed across the redshift bin considered for all the pairs. Thus, the wrongly inferred position of each interloper can be written in terms of a constant displacement along the LOS $\hat{z}$: $\vec{x}_{\mathrm{i}} = \vec{y}_{\mathrm{i}} - \Delta d\,\hat{z}$, where $\vec{y}_{\mathrm{i}}$ is the true position.

The interloper auto-correlation function can then be written as $\xi_{\mathrm{ii}}(\vec{x}_1 - \vec{x}_2) = \xi_{\mathrm{ii}}(\vec{y}_1 - \vec{y}_2)$ (where we have assumed that the LOS is the same for both galaxies in a pair), because two point correlators are invariant under translations – they depend only on the relative distance between two objects. This means that the correlation function of the interlopers at the wrong redshifts is equal to the correlation function of the interlopers at their true position.

Interlopers and targets belong to two different populations of galaxies and have in principle different bias schemes. Consequently, we either need calibration data to measure $\xi_{\mathrm{gi}}(\vec{r})$ and $\xi_{\mathrm{ii}}(\vec{r})$ (we discuss this particular case in section 3.6), or we need a way to model this function. On the other hand, we note that since displacements are small, interlopers and targets both trace a matter field with similar amplitude of clustering. It is also likely that interlopers have similar properties and intrinsic clustering as the target galaxies, meaning that they share the same galaxy bias. We thus make a second assumption: targets and interlopers share the same galaxy bias. In this case, together with the assumption of constant displacement for the interlopers, we have: $\xi_{\mathrm{ii}}(\vec{r}) = \xi_{\mathrm{gg}}(\vec{r})$. We assume that this is true in the rest of the chapter. Our results and conclusions will be similar if this is not true, but instead we are able to accurately estimate or model the bias scheme of the interlopers. Substituting into Eq. 3.4 yields

$$\xi(\vec{r}; f_{\mathrm{i}}) = (1 + 2f_{\mathrm{i}}^2 - 2f_{\mathrm{i}})\xi_{\mathrm{gg}}(\vec{r}) + 2f_{\mathrm{i}}(1 - f_{\mathrm{i}})\xi_{\mathrm{gi}}(\vec{r})\,. \tag{3.5}$$

In the next section, we will further consider methods to estimate the cross-correlation between interlopers and galaxies, $\xi_{\mathrm{gi}}(r)$.

3.4.2 Interloper-Target Cross-correlation

As mentioned before, the cross-correlation between galaxies and interlopers plays a key role in determining the shape of the contaminated correlation function. While the galaxy-

galaxy and interloper-interloper terms remain unchanged after misplacing interlopers along the LOS, the galaxy-interloper cross-correlation changes greatly. This change can easily be understood considering that $\xi_{\rm gi}$ at $\vec{r} = \vec{x}_1 - \vec{x}_2$, which is the separation between the two objects after misplacing interlopers by Δd, should be equal to $\xi_{\rm gi}$ at the true separation $\vec{r}\,' = \vec{x}_1 - \vec{y}_2$ (see Appendix B). Thus,

$$\xi_{\rm gi}(\vec{r}) = \xi_{\rm gi}(\vec{r}\,')\,. \tag{3.6}$$

There is a simple trigonometry transformation between $\vec{r}$ and $\vec{r}\,'$

$$\begin{aligned} r'(r,\mu) &= \sqrt{r^2 + \Delta d^2 - 2\,\Delta d\, r\, \mu}\,, \\ \mu'(r,\mu) &= \frac{r\mu - \Delta d}{\sqrt{r^2 + \Delta d^2 - 2\,\Delta d\, r\, \mu}}\,. \end{aligned} \tag{3.7}$$

where we have defined $r = |\vec{r}|$ being the modulus of the separation vector and $\mu = \vec{r}\cdot\hat{z}/r$ being the cosine of the angle between the separation vector and the LOS.

The auto-correlation to cross-correlation mapping effectively pushes pair separations to larger scales. Nearby objects are more correlated than more distant objects – the galaxy correlation function roughly decays by r^2, so the displacement of interlopers effectively moves the strong correlation between nearby objects around $< 20\,h^{-1}$ Mpc to larger scales in the galaxy-interloper cross-correlation, leaving a peak. The location of the center of this peak is at the interloper displacement. We show this in Figure 3.4 with blue points obtained by measuring the cross-correlation between galaxies and interlopers in a Quijote simulation box at $z = 1$, after misplacing interlopers by $97\,h^{-1}$ Mpc.

In practice, if we have a small survey with higher signal-to-noise ratio (calibration data), it will be possible to estimate which galaxies would appear as interlopers in a survey with lower signal-to-noise ratio. Using calibration data we can directly measure the cross-correlation between galaxies and interlopers at their *true* distance, and then infer the cross-correlation component at the wrong distance via Eq. 3.7. If the calibration data is not available, there are two other possible approaches that we discuss in the following to estimate the cross-correlation assuming that the bias scheme of interlopers is the same as main target galaxies: analytical and observational approaches.

Analytical approach: We considered taking the Fourier transform of the analytical power spectrum from CAMB linear and non-linear (from HALOFIT [143, 144]) to estimate the auto-correlation function. The results from the linear CAMB model are shown in red in Figure 3.4. The top and bottom panels of this plot show that the linear CAMB model roughly describes the shape of the measured monople and quadrupole of the cross-correlation, but it underestimates the peak height by $\sim 30\%$. This is because the prediction of CAMB for the monopole at small scales is significantly lower than the non-linear reality, and, as we discussed earlier, this directly impacts the height of the peak at $97\,h^{-1}\,\mathrm{Mpc}$. We have also used HALOFIT to create a non-linear model. The corresponding results are shown in green in the same figure. The outcome remains the same with a slightly better prediction of the height. In this case, while the displacement depends on the fiducial cosmology and it determines the position of the peak in the target-interloper correlation function, the shape of the cross-correlation depends on the true cosmology since it is a remapping of the auto-correlation of target galaxies via Eq. 3.13. This can be easily implemented in the model for the correlation function. The inability of this model to accurately fit the cross-correlation function led us to consider our second approach, or the observational approach.

Observational approach: If we assume that interlopers and targets are drawn from the same population of galaxies, we can estimate their cross-correlation directly from the measured auto-correlation of the contaminated catalog. As shown in figure 3.4, the monopole of cross-term vanishes on small scales $r < 40\,h^{-1}\,\mathrm{Mpc}$. Therefore, one can rewrite Eq. 3.5 as

$$\xi(\vec{r}; f_{\mathrm{i}}) \approx (1 + 2f_{\mathrm{i}}^2 - 2f_{\mathrm{i}})\,\xi_{\mathrm{gg}}(\vec{r}) \quad \text{for small r}, \tag{3.8}$$

indicating that the contaminated and uncontaminated catalogs have small-scale correlation functions that differ by an overall amplitude only, and this amplitude depends on the fraction of interlopers in the contaminated catalog. We can therefore infer the galaxy-galaxy small-scale correlation function directly from the measured contaminated correlation function, modulo an overall normalization. The large-scale feature in the cross-correlation seen in Figure 3.4 is mainly determined by the small-scale correlation of galaxies and interlopers at the true position, or equivalently the galaxy auto-correlation since we assumed that galaxies and interlopers have the same bias (see Eq. 3.6). Therefore, using Eqs. 3.8 and 3.6 we can estimate the cross-correlation term on the scales of interest ($r < 150\,h^{-1}\,\mathrm{Mpc}$) directly from the measured small-scale contaminated correlation function as

$$\xi_{\mathrm{gi}}(\vec{r}) = \frac{\xi(\vec{r}\,'; f_{\mathrm{i}})}{(1 + 2f_{\mathrm{i}}^2 - 2f_{\mathrm{i}})}\,, \tag{3.9}$$

where the mapping between $\vec{r}$ and $\vec{r}\,'$ is described in Eq. 3.7. Using this observational method, the model for the cross-correlation is already built from a correlation function in the true cosmology but measured in the fiducial one, and we will not need to account for differences between the two cosmologies when performing the fit.

Using this method to determine the cross-correlation, one can immediately see the improvement in the peak height estimation of the monopole and quadrupole moments of the cross-correlation function in Figure 3.4 (orange line). Note that this method assumes that interlopers and targets have the same bias scheme, and this assumption is satisfied exactly in our mocks. On the other hand, the general shape of the monopole of the cross-correlation, especially at larger scales, deviates from that of the measurement. We believe that this is due to the approximation that we made to derive Eq. 3.8; that of a vanishing cross-correlation on small scales. The quadrupole is less affected by this approximation. These effects do not alter the measured parameters (see Section 3.4.3). Finally, using this approximation, we can use Eq.3.9 for the galaxy-interloper cross-correlation and rewrite Eq. 3.5

$$\xi(\vec{r}; f_{\rm i}) = (1 + 2f_{\rm i}^2 - 2f_{\rm i})\xi_{\rm gg}(\vec{r}) + \frac{2f_{\rm i}(1 - f_{\rm i})}{(1 + 2f_{\rm i}^2 - 2f_{\rm i})} \times \mathcal{M}[\xi(f_i)](\vec{r})\,, \tag{3.10}$$

where for simplicity, we use $\mathcal{M}$ to denote the mapping of scales in Eq. 3.7 that describes the deformation due to interlopers.

3.4.3 Building a Cosmological Model

Thus far, we have introduced a model for the contaminated correlation function that consists of the galaxy-galaxy correlation function term, $\xi_{\rm gg}(\vec{r})$, and the cross-correlation term, $\xi_{\rm gi}(\vec{r}; f_{\rm i})$. There is still one part missing: How does our model depend on the assumptions about the fiducial cosmology? In this section, we will address this question based on the methodology and notation of Ref. [145] and [146].

To measure the correlation function from data, we need to calculate the separation between pairs by assuming a fiducial cosmology to translate from redshifts to distances. The BAO peak in the correlation function can be distorted if the assumed cosmology is not the same as the true cosmology. This distortion can be parameterized by Alcock–Paczynski parameters (hereafter AP; [147]): α, the isotropic dilation parameter, and ϵ, the anisotropic warping parameter:

$$\begin{aligned} \alpha &= \left[\frac{D_{\rm A,true}^2(z) H_{\rm fid}(z)}{D_{\rm A,fid}^2(z) H_{\rm true}(z)}\right]^{1/3} \frac{r_{\rm s,fid}}{r_{\rm s,true}}\,, \\ 1 + \epsilon &= \left[\frac{D_{\rm A,fid}(z) H_{\rm fid}(z)}{D_{\rm A,true}(z) H_{\rm true}(z)}\right]^{1/3}\,. \end{aligned} \tag{3.11}$$

And we can relate the fiducial and true distances using α and ϵ using the following equations:

$$\begin{aligned} r_{\parallel,\rm true} &= \alpha(1+\epsilon)^2 r_\parallel\,, \\ r_{\perp,\rm true} &= \alpha(1+\epsilon)^{-1} r_\perp\,, \end{aligned} \tag{3.12}$$

where we have dropped subscript "fid" for simplicity. The separation between two objects can be described in Cartesian $(r_\perp, r_\parallel)$ or polar coordinates (r, μ), which are related by

$$\begin{aligned} r^2 &= r_\perp^2 + r_\parallel^2\,, \\ \mu &= \cos(\theta) = \frac{r_\parallel}{r}\,. \end{aligned} \tag{3.13}$$

Therefore Eq. 3.13 for the true separations would be

$$\begin{aligned} r_{\rm true} &= \alpha\sqrt{(1+\epsilon)^4 r_\perp^2 + (1+\epsilon)^{-2} r_\parallel^2} \\ \mu_{\rm true} &= \frac{(1+\epsilon)^2 r_\parallel}{\sqrt{(1+\epsilon)^4 r_\perp^2 + (1+\epsilon)^{-2} r_\parallel^2}} \end{aligned} \tag{3.14}$$

The true correlation function can be decomposed into its Legendre multipoles. In the following, we assume that monopole, quadrupole, and hexadecapole would suffice in the summation below, as the higher order moments can be ignored.

$$\xi(r_{\rm true}, \mu_{\rm true}) = \sum_{l=0,2,4} \xi_l(r_{\rm true})\, \mathcal{L}_l(\mu_{\rm true}) \tag{3.15}$$

What we measure in reality, assuming a wrong fiducial cosmology, is shifted multipole moments of the correlation function ,

$$\xi_l(r; \alpha, \epsilon) = \frac{2l+1}{2} \int_{-1}^{1} d\mu L_l(\mu)\, \xi(r_{\rm true}(\alpha, \epsilon), \mu_{\rm true}(\alpha, \epsilon))\,. \tag{3.16}$$

For a BAO-only measurement, we are not interested in any feature of the correlation function other than where the BAO is. Typically, one adds an additive polynomial term $A(r)$ to account for the scale-dependent bias and redshift space distortions, and a multiplicative $B(r)$ factor to adjust the amplitude,

$$\xi_l^{\rm model}(r; \alpha, \epsilon) = B(r)\xi_l(r; \alpha, \epsilon) + A(r)) \tag{3.17}$$

Using the right form of polynomials is important, because even though $A(r)$ and $B(r)$ are nuisance parameters not containing any BAO information, they may bias our estimation of the BAO peak if not properly fitted for. We use three orders of polynomials: $A(r) = a_1/r^2 + a_2/r + a_3$, and a constant for the amplitude $B(r) = B_0$. Substituting Eq. 3.17 into Eq. 3.10 gives our final model for the monopole and quadrupole of a catalogue contaminated by some fraction of interlopers $f_{\rm i}$

$$
\begin{aligned}
&\xi_0^{\rm model}(r;\{a_1,a_2,a_3,B_0,\alpha,\epsilon,f_{\rm i}\}) \\
&\qquad = (1+2f_{\rm i}^2-2f_{\rm i})\times\Big[(\frac{a_1}{r^2}+\frac{a_2}{r}+a_3)+B_0\,\xi_0(r;\alpha,\epsilon))\Big] \\
&\qquad + \frac{2f_{\rm i}(1-f_{\rm i})}{(1+2f_{\rm i}^2-2f_{\rm i})}\times\mathcal{M}_0[\xi^{\rm measured}](r)\,,
\end{aligned}
\tag{3.18}
$$

$$
\begin{aligned}
&\xi_2^{\rm model}(r;\{w_1,w_2,w_3,B_0,\alpha,\epsilon,f_{\rm i}\}) \\
&\qquad = (1+2f_{\rm i}^2-2f_{\rm i})\times\Big[(\frac{w_1}{r^2}+\frac{w_2}{r}+w_3)+B_0\,\xi_2(r;\alpha,\epsilon))\Big] \\
&\qquad + \frac{2f_{\rm i}(1-f_{\rm i})}{(1+2f_{\rm i}^2-2f_{\rm i})}\times\mathcal{M}_2[\xi^{\rm measured}](r)\,.
\end{aligned}
\tag{3.19}
$$

Throughout this chapter, when we refer to a monopole only fit, we use Eq. 3.18 assuming $\epsilon = 0$, which simplifies $\xi_0(r;\alpha,\epsilon)$ to just $\xi_0(\alpha r)$. In that case, there are six free parameters that we fit for. When we refer to simultaneous monopole and quadrupole fit, we use Eq. 3.18 and 3.19 together. In that case, there are four additional free parameters (ten in total) that should be fitted for.

In the following, we describe the method used to obtain the templates of the monopole and quadrupole, $\xi_0(r)$ and $\xi_2(r)$. We model the matter power spectrum in real space as

$$
P(k,\mu) = [P_{\rm lin}(k) - P_{\rm smooth}(k)]\, e^{-\frac{1}{2}k^2(\mu^2\Sigma_\parallel^2+(1-\mu^2)\Sigma_\perp^2)} + P_{\rm smooth}(k)\,. \tag{3.20}
$$

where $P_{\rm lin}(k)$ is the linear matter power spectrum obtained from CAMB and $P_{\rm smooth}(k)$ is the no-wiggle counterpart computed as in [148], where the BAO oscillations have been removed. The Gaussian term accounts for the damping of the BAO wiggles due to non-linear evolution, with $\Sigma_\perp = 4.8\,h^{-1}$ Mpc and $\Sigma_\parallel = 7.3\,h^{-1}$ Mpc at $z = 1$ and the considered cosmology. In redshift space, the power spectrum is distorted by the Kaiser [48] and the Finger-of-God (FoG) [149] effects, which lead us to the following equation for the redshift space power spectrum [150]

$$
P_{\rm s}(k,\mu) = b^2(1+\beta\mu^2)^2F(k,\mu)P(k,\mu)\,. \tag{3.21}
$$

In our analysis, we use the streaming model for FoG, $F(k,\mu) = (1+k^2\mu^2\Sigma_s^2)^{-2}$, with $\Sigma_s = 3\,h^{-1}$ Mpc. Subsequently, we calculate the correlation function by taking the Fourier transform of the redshift-space power spectrum.

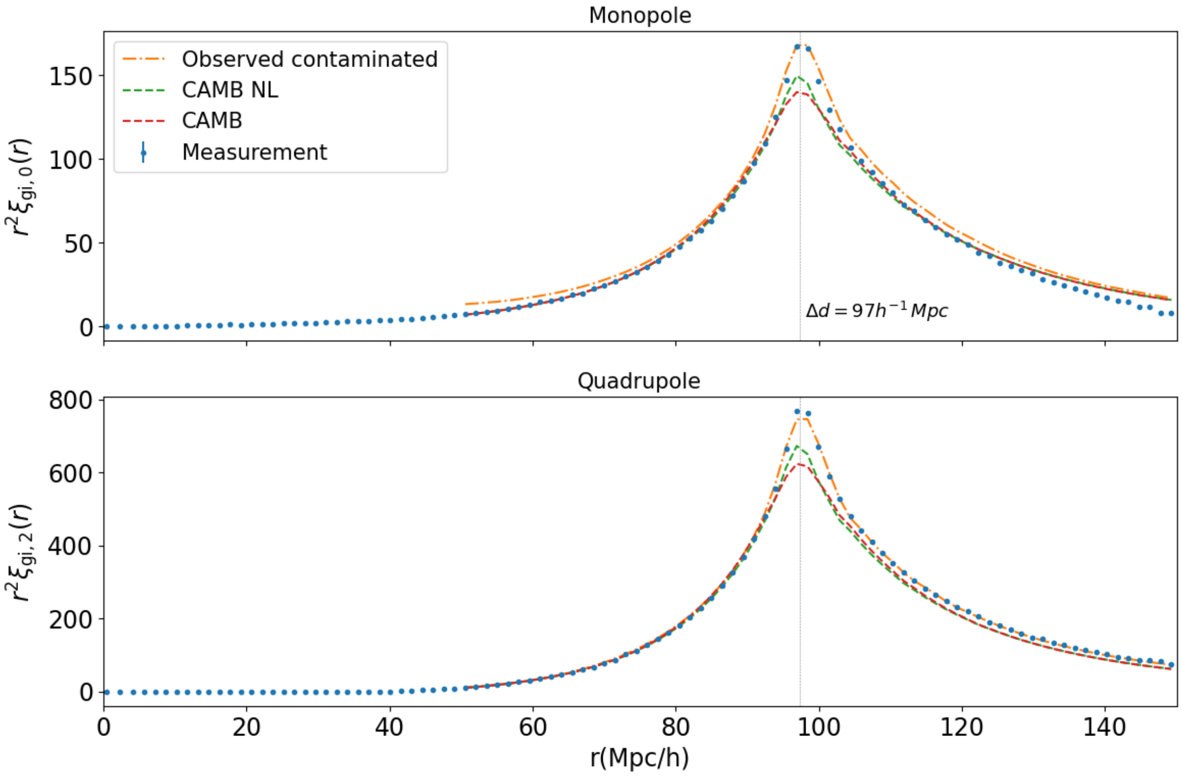

Figure 3.4: The importance of accurately modelling the small-scale cross-correlation in order to match the large-scale clustering around the BAO feature. Monopole (top) and quadrupole (bottom) of the galaxy-interloper cross-correlation function correlation in real-space, calculated from mapping of auto-correlation described in Eq. 3.6. We considered four different auto-correlations described in more detail in text. The interloper displacement, Δd, used in mapping equals 97 for $z = 1$.

3.5 Results

In this section, we present the results obtained by fitting the mean of the multipole moments of the correlation functions from $1,000$ mocks in redshift space (Same results for configuration space are shown in Appendix C). To find the best fit parameters, we carried out a Markov-chain Monte Carlo (MCMC) analysis (emcee package [151]) to minimize the posterior function introduced by Percival et al. [152]:

$$f(\xi^{\rm model}|\xi^{\rm data}, C) \propto \left[1 + \frac{\chi^2}{n_s - 1}\right]^{-\frac{m}{2}}\,, \tag{3.22}$$

where m is given by Eq. 54 of [152]. We also assumed the following uniform priors on our parameters:

$$f(\alpha, \epsilon, f_i) = \begin{cases} 1 & \text{if } 0.6 < \alpha < 1.4\,, \\ & \& \ -1 < \epsilon < 1\,, \\ & \& \ 0 < f_i < 0.5 \\ 0 & \text{otherwise} \end{cases} \tag{3.23}$$

Additionally, to calculate χ^2, we estimated the covariance matrix of $n_s = 1000$ independent contaminated mocks using

$$C_{ij}[\xi(r_i)\xi(r_j)] = \frac{1}{n_s - 1}\sum_{n=1}^{n_s}[\xi_n(r_i) - \bar{\xi}(r_i)][\xi_n(r_j) - \bar{\xi}(r_j)]\,. \tag{3.24}$$

To fit the model to the mean of n_s mocks, Eq. 3.24, which gives the covariance matrix used for an individual mock, is divided by n_s. For the purpose of this chapter, we only need to fit the data around the BAO peak. Therefore, in our analyses, we fit our model to data on scales between $r_{\rm min} = 50\,h^{-1}$ Mpc and $r_{\rm max} = 150\,h^{-1}$ Mpc. For a comparison between the data and the fits refer to Appendix D.

Let us begin with highlighting the necessity of correcting for the small-displacement interloper effect, and also roughly quantifying what we mean by “small” displacements. For this purpose, we repeated the process of making contaminated catalogues described in Section 3.3, but for a wider range of displacements, from 45 to $200\,h^{-1}$ Mpc. Without correcting for the interloper effect, we found the best fit estimations on α and ϵ. In Figure 3.6, the difference between the estimation and true is plotted against displacement, and from this figure we find that:

- *Monopole only with no correction (green triangles):* At a fixed value for the displacement Δd, the estimated isotropic dilation parameter α_{est} increasingly deviates from 1 when considering larger interloper fractions. This means that the bias in α introduced by the interlopers increases with the amount of contamination, as previously noted in [138]. How much the bias increases with f_i depends on the value of the displacement: the smaller the displacement, the faster the bias increases with the amount of contamination. Indeed, when the displacement is close to the BAO position, e.g. $\Delta d = 97\,h^{-1}\,\text{Mpc}$, the peak in the galaxy-interloper cross-correlation is very close to the BAO location and it causes a mild distortion and shift of the BAO peak. On the other hand, smaller displacements present a peak in the cross-correlation that is further away from the BAO peak location, causing a much larger distortion of the BAO feature (see also Figure 3.2).

- *Monopole+Quadrupole with no correction (green rectangles):* Compared to the previous case (monopole only with no correction) and for each combination of Δd and f_i^{true}, α_{est} is closer to 1 when including the quadrupole in the fit. This happens because the contamination is anisotropic: By including the quadrupole, the parameter ϵ can mimic and absorb the anisotropy, leaving α less biased. However, the ϵ measurements are strongly biased, with deviations from the fiducial value increasing with the amount of contamination and decreasing with increasing Δd.

- *Monopole only with interloper correction (orange triangles):* Compared to the no correction case, the values of α_{est} are now much closer to the true value and they exhibit a systematic bias smaller than 3.9×10^{-3} for all considered level of contamination and displacements. This model allows us to obtain an estimation for the fraction of interlopers f_i^{est} with a bias that is below 8×10^{-3} for all levels of contamination and displacements. (More details in Table 3.2)

- *Monopole+Quadrupole with interloper correction (orange rectangles):* The values of α_{est} and ϵ_{est} are much closer to the truth than in the no correction case. The residual systematic biases are smaller than 5×10^{-3} for α and 0.01 for ϵ. The percentage of contaminants can be estimated with better precision in this case than when fitting for the monopole alone: the statistical errors decrease by a factor of two on average. The accuracy on f_i is also generally improved when the displacement is small, while no significant amelioration appears if $\Delta d = 97\,h^{-1}\,\text{Mpc}$.

We should emphasize that large-displacements can still bias the BAO measurement, even though the cross-correlation would be negligible, as mentioned in Section 3.1.

Now, we take into account the effect of interlopers in the fitting model by using the formalism described in Section 3.4. Figure 3.5 demonstrates how much the estimation of our pipeline for α (top row), ϵ (middle row), and f_i (lower row) deviates from the corresponding true values when considering catalogs contaminated by different fractions of interlopers (x-axis), and three different values for the displacements Δd: $85\,h^{-1}\,\mathrm{Mpc}$ (left column), $90\,h^{-1}\,\mathrm{Mpc}$ (middle column), and $97\,h^{-1}\,\mathrm{Mpc}$ (right column). The orange symbols corresponds to the case where we account for the presence of interlopers in our analysis using Eq. 3.10, whereas green symbols show the results when ignoring interlopers (as if f_i was set to zero in Eq. 3.10). We considered fits to the monopole alone (shown in triangle) and to the monopole and quadrupole simultaneous (rectangles). From figure 3.5, we deduce that:

- *Monopole only with no correction (green triangles):* At a fixed value for the displacement Δd, the estimated isotropic dilation parameter α_{est} increasingly deviates from 1 when considering larger interloper fractions. This means that the bias in α introduced by the interlopers increases with the amount of contamination, as previously noted in [138]. How much the bias increases with f_i depends on the value of the displacement: the smaller the displacement, the faster the bias increases with the amount of contamination. Indeed, when the displacement is close to the BAO position, e.g. $\Delta d = 97\,h^{-1}\,\mathrm{Mpc}$, the peak in the galaxy-interloper cross-correlation is very close to the BAO location and it causes a mild distortion and shift of the BAO peak. On the other hand, smaller displacements present a peak in the cross-correlation that is further away from the BAO peak location, causing a much larger distortion of the BAO feature (see also Figure 3.2).

- *Monopole+Quadrupole with no correction (green rectangles):* Compared to the previous case (monopole only with no correction) and for each combination of Δd and f_i^{true}, α_{est} is closer to 1 when including the quadrupole in the fit. This happens because the contamination is anisotropic: By including the quadrupole, the parameter ϵ can mimic and absorb the anisotropy, leaving α less biased. However, the ϵ measurements are strongly biased, with deviations from the fiducial value increasing with the amount of contamination and decreasing with increasing Δd.

- *Monopole only with interloper correction (orange triangles):* Compared to the no correction case, the values of α_{est} are now much closer to the true value and they exhibit a systematic bias smaller than 3.9×10^{-3} for all considered level of contamination and displacements. This model allows us to obtain an estimation for the fraction of interlopers f_i^{est} with a bias that is below 8×10^{-3} for all levels of contamination and displacements. (More details in table 3.2)

- *Monopole+Quadrupole with interloper correction (orange rectangles):* The values of α_{est} and ϵ_{est} are much closer to the truth than in the no correction case. The residual systematic biases are smaller than 5×10^{-3} for α and 0.01 for ϵ. The percentage of contaminants can be estimated with better precision in this case than when fitting for the monopole alone: the statistical errors decrease by a factor of two on average. The accuracy on f_i is also generally improved when the displacement is small, while no significant amelioration appears if $\Delta d = 97\,h^{-1}\,\mathrm{Mpc}$.

A more detailed description of our results of the monopole+quadrupole and monopole only analyses are given in table 3.1 and table 3.2 respectively, where the systematic and statistical errors on α, ϵ and f_i are reported for all the displacements and fractions considered. We find that the systematic error on α with interlopers using our model is 4.4×10^{-3} which is consistent with pre-reconstruction BAO analyses on SDSS data without interlopers ([65], [153], [64]). This shows that slitless spectroscopy does not degrade BAO measurements.

3.6 Discussions

We have investigated how to extract the BAO scale from a contaminated galaxy catalogue containing a sub-sample of interlopers that are correlated with the main target galaxies. This case is particularly important for the future Roman Space Telescope, where a population of [O III] emitting galaxies extracted thanks to the observation of a single line is likely to be contaminated by Hβ interlopers. In this study, we assumed that the Hβ line is misidentified as the primary line at 500.7 nm of the [O III] doublet. Depending on how the doublet is fitted, one might need to take into account the weighted average of the primary and the secondary lines of [O III]. Nonetheless, this will only impact the value of Δd as a function of redshift in Eq. 3.2, and will not affect our conclusions. In the following, we highlight some of the main outcomes of our analysis.

Generally, the contaminated correlation function has three terms (Eq.3.4): The galaxy-galaxy term, the interloper-interloper term, and the galaxy-interloper term. We have split interlopers into three categories: random, large-displacement and small-displacement interlopers. We have argued that random contaminants, uncorrelated with either themselves or the target galaxies are trivial to account for.

Table 3.1: Systematic and statistical errors on α, ϵ, and f_i using monopole and quadrupole. Analysis is performed on the mean of 1000 mocks in redshift space, and different displacements.

$f_i^{\rm true}(\times 10^{-2})$	Error on α $(\times 10^{-3})$		Error on ϵ $(\times 10^{-3})$		Error on f_i $(\times 10^{-3})$	
	systematic	statistical	systematic	statistical	systematic	statistical
$\Delta d = 85\mathrm{h}^{-1}\mathrm{Mpc}$						
0	4.1	0.7	-0.5	0.9	0.7	0.4
2	3.9	0.8	-1.5	1.1	1.4	0.4
5	3.5	0.8	-3.1	1.1	1.4	0.4
10	2.5	0.8	-5.4	1.0	-0.5	0.4
15	1.6	0.9	-7.3	1.1	-4.7	0.4
$\Delta d = 90\mathrm{h}^{-1}\mathrm{Mpc}$						
0	4.1	0.7	-0.5	1.0	0.4	0.3
2	3.6	0.9	-1.5	1.4	1.1	0.5
5	3.0	0.8	-4.1	1.3	2.1	0.5
10	0.3	0.8	-7.9	1.3	1.2	0.5
15	0.3	0.9	-10.8	1.5	-2.9	0.6
$\Delta d = 97\mathrm{h}^{-1}\mathrm{Mpc}$						
0	4.3	0.7	0.1	0.8	0.1	0.1
2	4.4	0.7	1.1	0.9	-1.0	0.4
5	3.5	0.8	-0.7	1.1	-0.5	0.5
10	3.9	1.1	-2.5	1.5	-2.4	0.5
15	3.4	1.2	-4.3	1.7	-6.5	0.6

For both small-displacement and large-displacement interlopers, we need to model their auto-correlation, but this is generally easy to do. In addition, the effect of the interloper-interloper auto-correlation on the contaminated signal is a simple linear super-position of two correlation functions: in the extremes, either the change in $H(z)$ between true redshifts of the targets and interlopers is small and so the BAO position is unaffected, or it is large and the superimposed BAO peak is far from that of the targets. In either case and in between, to measure the BAO position, we only need a model on large scales where linear theory is sufficient to describe the BAO feature and we know the position through the relative line positions. If interlopers and galaxies have different bias, an extra (bias) parameter can be added to the second term of Eq. 3.4 and can be fitted for along other parameters introduced in our analysis. It also may be possible to measure this using calibration data, by comparing the interloper-interloper and target-target correlation functions. In contrast, for small-displacement interlopers, it is critical to have a good estimate of the interloper-target cross-correlation.

For our simulations, the interlopers are drawn from the same underlying distribution as the target galaxies. This allowed us to simplify the equations, merging the galaxy-galaxy and interloper-interloper terms together. In practice, the populations of [O III] and Hβ emission line galaxies are different, and this can change our equations requiring us to keep these terms separate. We do not expect this to significantly alter our conclusions, or to present a difficulty for modeling.

For small-displacement interlopers, the interloper shift can be considered as being constant, and is dependent on the fiducial cosmology used to convert redshifts to distances. Thus its position does not provide cosmological information. We made the assumption of a constant shift because the displacement only changes by less than one percent across the bin considered, similar to the case for the BAO scale being fixed within an bin of observational data. Hence, the BAO signal in $\xi_{\mathrm{ii}}(\vec{r})$ will not be shifted as a correlation function is not modified by a translation, while it is modified in $\xi_{\mathrm{gi}}(\vec{r})$. Thus, the key to understanding and modelling the contaminated correlation function is through accurately modelling the cross-correlation between the main galaxy targets and the interlopers that are misidentified as main targets, which is described in Eq. 3.6 and required a mapping between true and wrongly inferred positions for the interlopers. Again, with calibration data, it is possible to apply this mapping (refer to 3.7) to the measured cross-correlation at the true distance. We leave it to future work to determine the size of calibration data required to determine this function with sufficient accuracy that it does not impact on BAO measurements. The good news is that we need to know this function on small scales, where small volumes of the Universe will be sufficient.

For our study, we used the same assumptions used to create the simulations (the [O III] and Hβ emitting galaxies are drawn from the same population) to estimate the cross-correlation with the auto-correlation function of the main galaxy targets. We considered models based on CAMB and HALOFIT to derive an estimation of the cross-correlation. We found that they both fail in precisely modelling the peak of the monopole and quadrupole of the cross-correlation. These models also need to account for the difference between fiducial and true cosmologies via the AP parameters, that would need to be added in the cross-correlation function of Eq. 3.18, and Eq. 3.19 as well. Therefore, we tested another possibility that is more powerful on smaller scales: using the measured contaminated correlation functions to estimate cross-correlation. We argued that using the latter is the most precise for the Quijote mocks used in this chapter, since it matches the way that the mocks were constructed (interlopers and target galaxies have the same galaxy bias). Indeed, the resulting cross-correlation is able to better model the peak of the monopole of the cross-correlation, and both peak and the shape of the quadrupole of the cross-correlation (refer to Figure 3.4).

With all of the mentioned assumptions made, we finally presented a model for monopole and quadrupole of the contaminated correlation function. We tested our model by fitting it to the mean of 1,000 mocks for five different interloper fractions and three different displacements. We found that for all these cases, our method is successful at making an unbiased prediction of the dilation parameters (recovering the BAO peak), with a systematic error of less than 4.4×10^{-3}, which is consistent with previous pre-reconstruction analyses. It also enables us to have a good estimation of the fraction of interlopers. Whereas if we did not take interlopers into account in the model, for 15% interlopers we would have an order of magnitude higher systematic errors – as high as -0.020 and 0.044 for α and ϵ. Moreover, the signal in the correlation function from interlopers is sufficiently clear that it allows us to measure the fraction of interlopers with a systematic error of at most few percent. This will be useful for cosmological analysis other than measuring BAO where the fraction of interlopers can change the amplitude of the signal, and knowing the fraction is important.

Since our analysis is specifically useful for future Roman [O III] targets that are contaminated by Hβ interlopers, we predict the statistical error that our method would have for Roman telescope data. To do so, we scaled the statistical errors on the mean calculations from 1,000 mocks at redshift 1 ($\Delta d = 85\,h^{-1}$ Mpc). These 1,000 mocks have a cumulative volume of $1,000(\mathrm{h}^{-1}\mathrm{Gpc})^3$. The approximate volume of Roman survey between redshift 1.8 and 2.8 (where [O III] galaxies live) is $V \approx 10(\mathrm{h}^{-1}\mathrm{Gpc})^3$. Thus, the statistical error is scaled by $\sqrt{1000/10} = 100$. For the range of $0-15\%$ interlopers, we find that the statistical error on α and ϵ is 0.01 which is larger than their corresponding systematic errors.

Small-displacement interlopers give rise to a strong signal in the correlation function on similar scales to the cosmological signal. Even so, this signal has key differences from the cosmological signal such that a joint model fitting both the cosmological signal and the effect of interlopers can be constructed and we do not see a degradation in the cosmological measurements in the tests we have performed. Furthermore, the interloper signal itself allows excellent diagnostics on the contamination, allowing a simultaneous fit to the contaminant fraction. For random interlopers however, it is more difficult to measure the contaminant fraction, which has to be done before the amplitude of clustering can be measured. Thus, while small-displacement interlopers are definitely the most pernicious in terms of the correlation function, for fits to the data this is not the case.

Table 3.2: Systematic and statistical errors on α, and f_i using the monopole only analysis performed on the mean of 1000 mocks in redshift space, and different displacements.

$f_i^{\text{true}}(\times 10^{-2})$	Error on α $(\times 10^{-3})$ systematic	Error on α $(\times 10^{-3})$ statistical	Error on f_i $(\times 10^{-3})$ systematic	Error on f_i $(\times 10^{-3})$ statistical
$\Delta d = 85\text{h}^{-1}\text{Mpc}$				
0	2.2	0.7	3.4	0.8
2	2.1	0.7	4.1	0.8
5	1.9	0.7	3.5	0.7
10	0.8	0.7	1.4	0.7
15	-0.1	0.8	-3.4	0.7
$\Delta d = 90\text{h}^{-1}\text{Mpc}$				
0	-0.6	0.8	6.9	0.9
2	-1.4	0.8	7.8	0.9
5	-1.5	0.9	7.7	0.9
10	-3.0	0.9	5.9	0.9
15	-3.9	0.9	1.0	0.8
$\Delta d = 97\text{h}^{-1}\text{Mpc}$				
0	2.7	0.7	0.6	0.5
2	3.2	0.9	-0.4	1.5
5	2.4	0.9	0.4	1.5
10	1.3	1.0	0.1	1.4
15	-0.9	1.2	-2.4	1.5

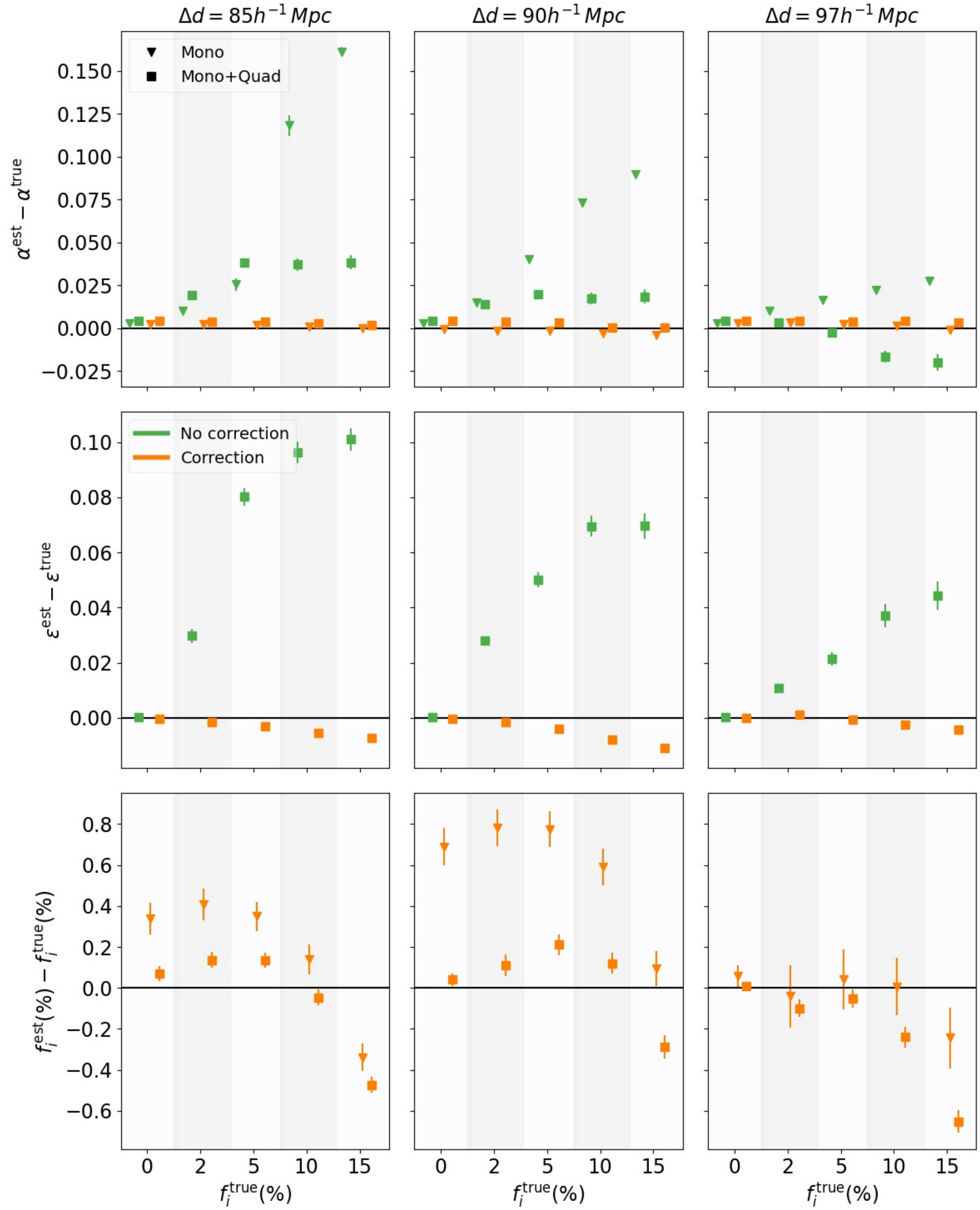

Figure 3.5: The difference between estimation and true for α (top row), ϵ (middle row), and f_i (bottom row), as plotted against the true fraction of interlopers. For comparison, the green lines show the fit without taking into account interlopers and the orange shows the fit with interlopers (our analysis).

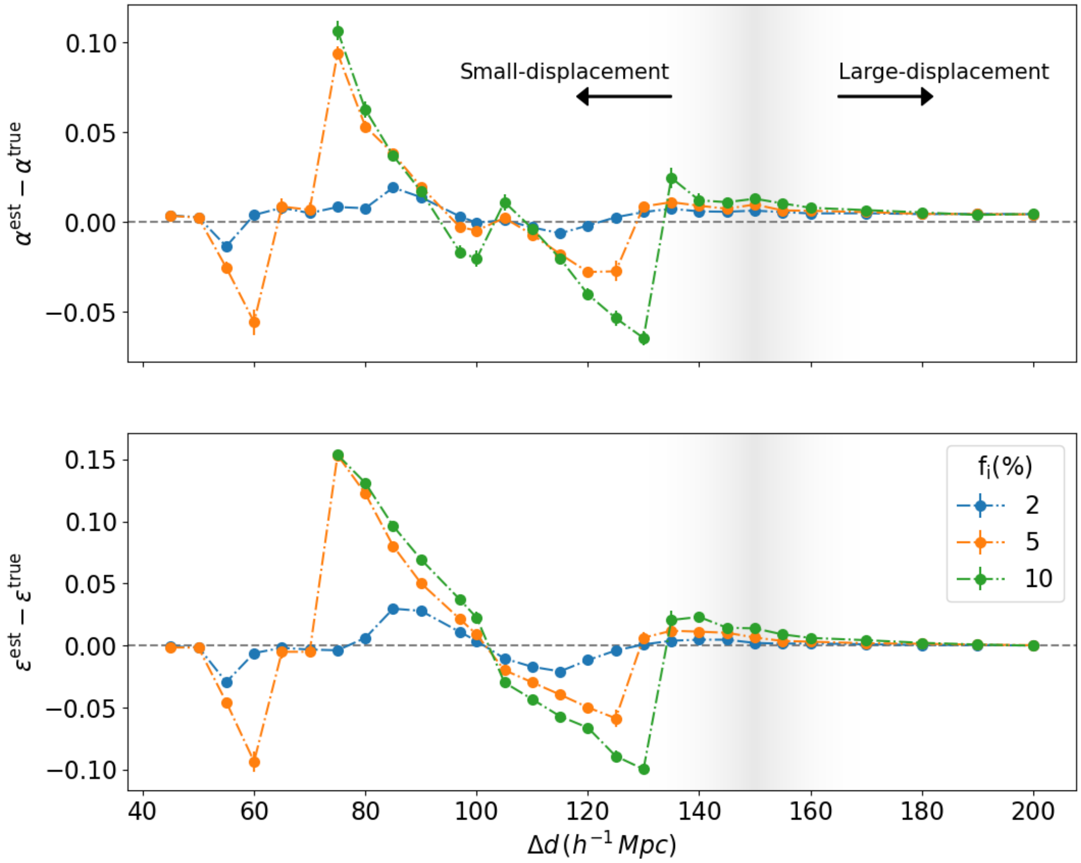

Figure 3.6: The effect of small-displacement interlopers on estimating the dilation parameters.

Chapter 4

Conclusions and future work

In Chapter 2, I presented my work on the Fisher analysis forecast on the uncertainties of the cosmological parameters measured by BAO and RSD analyses. We performed a Fisher analysis on 19 different survey catalogues to obtain the constraints on the BAO dilation parameters, D_M and D_H, and the growth rate of structure times the normalization factor, $f\sigma_8$, from BAO and RSD analyses. In the following, we consider the meaning of our results and their impact on future galaxy surveys.

We compared the prediction from our BAO Fisher analysis to the post-reconstruction BAO measurements and found that Fisher matrix calculations are very good at predicting BAO constraints and that measurements and the way in which they are analyzed are delivering the expected level of precision. This is clearly great news for future projects – one can trust the BAO Fisher analysis to forecast the constraints on the dilation parameters for future surveys. Moreover, it means that the current BAO analyses are exploiting a high level of precision. That being said, there is room for improvement, particularly with reconstruction.

On the other hand, for RSD measurements, we found a discrepancy between constraints obtained from the Fisher prediction and the measurements if $k_{\max}$ in the Fisher analysis is chosen to match the scale at which the power spectrum turns strongly non-linear, $0.1/D(z)$. The two constraints would match if $k_{\max}$ is chosen correctly – our work suggests that current methods extract RSD information to a fixed $k_{\max}$ for all samples and redshifts, and that is equal to $0.08\,h\,\mathrm{Mpc}^{-1}$. This can be interpreted in two ways: Either some RSD information is missing from the observations, or the information is there, but the current RSD analyses can not extract all the existing information and need to be improved.

Recent analyses have used emulators to extract information from smaller scales. By doing so, they have been able to provide substantial improvements on the precision obtained from RSD [130, 132, 154, 155]. Thus, we ruled out the former possibility (missing information) by testing the precision recovered from our Fisher analysis against that of small-scale RSD analysis and found that small-scale analyses *do* allow for extracting RSD information to smaller scales, i.e., $k_{\mathrm{max}} > 0.08\,h\,\mathrm{Mpc}^{-1}$. The improvement from small-scale analyses means that the RSD information is available, and improved modeling with fully extracting the linear signal may be able to extract it.

In Chapter 3, I presented our article on the effects of small-displacement contaminants on the BAO analysis. Small-displacement interlopers are galaxies whose observed distance is misplaced by $\Delta d \lesssim 150\,h^{-1}\,\mathrm{Mpc}$ along the line-of-sight due to line misidentification in low-resolution slitless spectroscopy. We focused on Roman-like catalogues, with an [O III] target line sample contaminated by Hβ interlopers, but our analysis can be generalized to other catalogues that are contaminated by small-displacement interlopers. We found that for 15% interlopers that are misplaced by $97\,\mathrm{Mpc}\,h^{-1}$, the systematic error can be as high as 2% on α and 4% on ϵ, if the model used to describe the correlation function does not account for the presence of interlopers (following [156]). Therefore, it is important that we use a model that takes into account that the catalogue might be contaminated.

Given the high interloper bias, we considered building a model for the monopole and quadrupole moments of the contaminated correlation function, including an additional free parameter for the level of contamination. The key ingredient of our model is the cross-correlation between the interloper galaxies at the wrong distance and the main target galaxies. We estimated this term using a distance convolution on the measured contaminated small-scale auto-correlation function. This method enabled us to measure the dilation parameters without significant degradation in accuracy. Furthermore, this model allows for estimating the fraction of interlopers with a systematic error of at most a few percent. Having an estimation of the fraction is important since it can be used in other future cosmological analyses, where the fraction of interlopers can change the amplitude of the signal.

Finally, let us briefly conclude the future impacts of these two projects:

- The bottom line from my first work is that considering recent improvements achieved from the RSD small-scale analyses, we can be optimistic that in the near future, measurements will be able to extract information from smaller scales (larger wavenumbers), hence reach the maximum theoretical precision possible. Until then, in order to realistically forecast the achievable precision of the upcoming galaxy surveys from *linear* RSD analyses, a correction to the maximum wavenumber should be made in the Fisher analysis: $k_{\mathrm{max}} = 0.08\,h^{-1}\,\mathrm{Mpc}$.

- The most critical impact of my second work for cosmology would be on the BAO analysis of the future Roman Space Telescope [O III] targets that are contaminated by Hβ interlopers. We provided a theoretical model for the contaminated auto-correlation, with which the recovered accuracy and precision of the dilation parameters are unchanged compared to uncontaminated catalogues, which is clearly good news for future slitless spectroscopy surveys prone to contamination. Indeed, improvements can be made to our analysis by, for instance: Using light-cone simulations, varying the interloper displacement with redshift instead of making the constant-displacement approximation, using better priors on f_i, including other (multiple) sources of contaminants, allowing the RSD parameters (Σ, β) and biases to vary in MCMC. Another possible future work is to use better simulations to know if the 22 deg^2 deep-field calibration data for Roman GRS would suffice for measuring the cross-correlation between [O III] and Hβ at $2 < z < 3$.

- Based on [157], Lyman α forest analysis is also prone to a small fraction of contaminants from silicon emission lines (metal contamination) with small-displacements at 20, 60 and $100\,h^{-1}$ Mpc. It is possible to constrain the effective biases of the contaminants ($b_g \times f_i$) mostly with the correlations near the LOS. Since, in this case, the impact of interlopers is asymmetric in the target-interloper cross-correlation, it is helpful to cross-check the constrained effective bias using the Lyα × QSO cross-correlation too. Another proposal for a future work is to use the method mentioned above in order to get an adequate measurement of the effective bias of our interlopers, i.e., make use of the cross-correlation of Roman with other surveys around the same redshift of interest: DESI ELGs at $z > 1$, quasars at $z > 1.5$ and Lyα forest at $z > 1.9$.

References

[1] Setareh Foroozan, Elena Massara, and Will J. Percival. Correcting for small-displacement interlopers in BAO analyses.

[2] Setareh Foroozan, Alex Krolewski, and Will J. Percival. Testing large-scale structure measurements against fisher matrix predictions. *J. Cosmol. Astropart. Phys.*, 2021(10):044, 10 2021.

[3] Stefan van der Walt, S. Chris Colbert, and Gael Varoquaux. The numpy array: A structure for efficient numerical computation. *Computing in Science Engineering*, 13(2):22–30, 2011.

[4] Pauli Virtanen, Ralf Gommers, Travis E. Oliphant, Matt Haberland, Tyler Reddy, David Cournapeau, Evgeni Burovski, Pearu Peterson, Warren Weckesser, Jonathan Bright, Stéfan J. van der Walt, Matthew Brett, Joshua Wilson, K. Jarrod Millman, Nikolay Mayorov, Andrew R. J. Nelson, Eric Jones, Robert Kern, Eric Larson, C J Carey, İlhan Polat, Yu Feng, Eric W. Moore, Jake VanderPlas, Denis Laxalde, Josef Perktold, Robert Cimrman, Ian Henriksen, E. A. Quintero, Charles R. Harris, Anne M. Archibald, Antônio H. Ribeiro, Fabian Pedregosa, Paul van Mulbregt, and SciPy 1.0 Contributors. SciPy 1.0: Fundamental Algorithms for Scientific Computing in Python. *Nature Methods*, 17:261–272, 2020.

[5] John D. Hunter. Matplotlib: A 2d graphics environment. *Computing in Science Engineering*, 9(3):90–95, 2007.

[6] Benedikt Diemer. COLOSSUS: A Python Toolkit for Cosmology, Large-scale Structure, and Dark Matter Halos. *ApJS*, 239(2):35, December 2018.

[7] The Astropy Collaboration, Robitaille, Thomas P., Tollerud, Erik J., Greenfield, Perry, Droettboom, Michael, Bray, Erik, Aldcroft, Tom, Davis, Matt, Ginsburg, Adam, Price-Whelan, Adrian M., Kerzendorf, Wolfgang E., Conley, Alexander,

Crighton, Neil, Barbary, Kyle, Muna, Demitri, Ferguson, Henry, Grollier, Frédéric, Parikh, Madhura M., Nair, Prasanth H., Günther, Hans M., Deil, Christoph, Woillez, Julien, Conseil, Simon, Kramer, Roban, Turner, James E. H., Singer, Leo, Fox, Ryan, Weaver, Benjamin A., Zabalza, Victor, Edwards, Zachary I., Azalee Bostroem, K., Burke, D. J., Casey, Andrew R., Crawford, Steven M., Dencheva, Nadia, Ely, Justin, Jenness, Tim, Labrie, Kathleen, Lim, Pey Lian, Pierfederici, Francesco, Pontzen, Andrew, Ptak, Andy, Refsdal, Brian, Servillat, Mathieu, and Streicher, Ole. Astropy: A community Python package for astronomy. *A&A*, 558:A33, 2013.

[8] Yun Wang. Flux-averaging analysis of type ia supernova data. 536(2):531–539.

[9] Adam G. Riess, Alexei V. Filippenko, Peter Challis, Alejandro Clocchiattia, Alan Diercks, Peter M. Garnavich, Ron L. Gilliland, Craig J. Hogan, Saurabh Jha, Robert P. Kirshner, B. Leibundgut, M. M. Phillips, David Reiss, Brian P. Schmidt, Robert A. Schommer, R. Chris Smith, J. Spyromilio, Christopher Stubbs, Nicholas B. Suntzeff, and John Tonry. Observational evidence from supernovae for an accelerating universe and a cosmological constant. 116(3):1009–1038.

[10] S. Perlmutter, G. Aldering, G. Goldhaber, R. A. Knop, P. Nugent, P. G. Castro, S. Deustua, S. Fabbro, A. Goobar, D. E. Groom, I. M. Hook, A. G. Kim, M. Y. Kim, J. C. Lee, N. J. Nunes, R. Pain, C. R. Pennypacker, R. Quimby, C. Lidman, R. S. Ellis, M. Irwin, R. G. Mcmahon, P. Ruiz-lapuente, N. Walton, B. Schaefer, B. J. Boyle, A. V. Filippenko, T. Matheson, A. S. Fruchter, N. Panagia, H. J. M. Newberg, and W. J. Couch. ACCEPTED FOR PUBLICATION IN the astrophysical journal preprint typeset using l ATEX style emulateapj v. 04/03/99.

[11] Adrian L. Melott, Jaan Einasto, Enn Saar, Ivar Suisalu, Anatoli A. Klypin, and Sergei F. Shandarin. Cluster analysis of the nonlinear evolution of large-scale structure in an axion/gravitino/photino-dominated universe. *Phys. Rev. Lett.*, 51:935–938, Sep 1983.

[12] S. D. M. White, C. S. Frenk, and M. Davis. Clustering in a neutrino-dominated universe. 274:L1.

[13] Albert Einstein. Kosmologische betrachtungen zur allgemeinen relativitätstheorie. pages 142–152, jan 1917.

[14] Brian P. Schmidt, Nicholas B. Suntzeff, M. M. Phillips, Robert A. Schommer, Alejandro Clocchiatti, Robert P. Kirshner, Peter Garnavich, Peter Challis, B. Leibundgut, J. Spyromilio, Adam G. Riess, Alexei V. Filippenko, Mario Hamuy, R. Chris Smith,

Craig Hogan, Christopher Stubbs, Alan Diercks, David Reiss, Ron Gilliland, John Tonry, Jose Maza, A. Dressler, J. Walsh, and R. Ciardullo. The high-z supernova search: Measuring cosmic deceleration and global curvature of the universe using type ia supernovae. *The Astrophysical Journal*, 507(1):46–63, nov 1998.

[15] DESI Collaboration, Amir Aghamousa, Jessica Aguilar, Steve Ahlen, Shadab Alam, Lori E. Allen, Carlos Allende Prieto, James Annis, Stephen Bailey, Christophe Balland, Otger Ballester, Charles Baltay, Lucas Beaufore, Chris Bebek, Timothy C. Beers, Eric F. Bell, José Luis Bernal, Robert Besuner, Florian Beutler, Chris Blake, Hannes Bleuler, Michael Blomqvist, Robert Blum, Adam S. Bolton, Cesar Briceno, David Brooks, Joel R. Brownstein, Elizabeth Buckley-Geer, Angela Burden, Etienne Burtin, Nicolas G. Busca, Robert N. Cahn, Yan-Chuan Cai, Laia Cardiel-Sas, Raymond G. Carlberg, Pierre-Henri Carton, Ricard Casas, Francisco J. Castander, Jorge L. Cervantes-Cota, Todd M. Claybaugh, Madeline Close, Carl T. Coker, Shaun Cole, Johan Comparat, Andrew P. Cooper, M.-C. Cousinou, Martin Crocce, Jean-Gabriel Cuby, Daniel P. Cunningham, Tamara M. Davis, Kyle S. Dawson, Axel de la Macorra, Juan De Vicente, Timothée Delubac, Mark Derwent, Arjun Dey, Govinda Dhungana, Zhejie Ding, Peter Doel, Yutong T. Duan, Anne Ealet, Jerry Edelstein, Sarah Eftekharzadeh, Daniel J. Eisenstein, Ann Elliott, Stéphanie Escoffier, Matthew Evatt, Parker Fagrelius, Xiaohui Fan, Kevin Fanning, Arya Farahi, Jay Farihi, Ginevra Favole, Yu Feng, Enrique Fernandez, Joseph R. Findlay, Douglas P. Finkbeiner, Michael J. Fitzpatrick, Brenna Flaugher, Samuel Flender, Andreu Font-Ribera, Jaime E. Forero-Romero, Pablo Fosalba, Carlos S. Frenk, Michele Fumagalli, Boris T. Gaensicke, Giuseppe Gallo, Juan Garcia-Bellido, Enrique Gaztanaga, Nicola Pietro Gentile Fusillo, Terry Gerard, Irena Gershkovich, Tommaso Giannantonio, Denis Gillet, Guillermo Gonzalez-de Rivera, Violeta Gonzalez-Perez, Shelby Gott, Or Graur, Gaston Gutierrez, Julien Guy, Salman Habib, Henry Heetderks, Ian Heetderks, Katrin Heitmann, Wojciech A. Hellwing, David A. Herrera, Shirley Ho, Stephen Holland, Klaus Honscheid, Eric Huff, Timothy A. Hutchinson, Dragan Huterer, Ho Seong Hwang, Joseph Maria Illa Laguna, Yuzo Ishikawa, Dianna Jacobs, Niall Jeffrey, Patrick Jelinsky, Elise Jennings, Linhua Jiang, Jorge Jimenez, Jennifer Johnson, Richard Joyce, Eric Jullo, Stéphanie Juneau, Sami Kama, Armin Karcher, Sonia Karkar, Robert Kehoe, Noble Kennamer, Stephen Kent, Martin Kilbinger, Alex G. Kim, David Kirkby, Theodore Kisner, Ellie Kitanidis, Jean-Paul Kneib, Sergey Koposov, Eve Kovacs, Kazuya Koyama, Anthony Kremin, Richard Kron, Luzius Kronig, Andrea Kueter-Young, Cedric G. Lacey, Robin Lafever, Ofer Lahav, Andrew Lambert, Michael Lampton, Martin Landriau, Dustin Lang, Tod R. Lauer, Jean-Marc Le Goff, Laurent Le Guillou, Auguste Le Van Suu, Jae Hyeon Lee,

Su-Jeong Lee, Daniela Leitner, Michael Lesser, Michael E. Levi, Benjamin L'Huillier, Baojiu Li, Ming Liang, Huan Lin, Eric Linder, Sarah R. Loebman, Zarija Lukić, Jun Ma, Niall MacCrann, Christophe Magneville, Laleh Makarem, Marc Manera, Christopher J. Manser, Robert Marshall, Paul Martini, Richard Massey, Thomas Matheson, Jeremy McCauley, Patrick McDonald, Ian D. McGreer, Aaron Meisner, Nigel Metcalfe, Timothy N. Miller, Ramon Miquel, John Moustakas, Adam Myers, Milind Naik, Jeffrey A. Newman, Robert C. Nichol, Andrina Nicola, Luiz Nicolati da Costa, Jundan Nie, Gustavo Niz, Peder Norberg, Brian Nord, Dara Norman, Peter Nugent, Thomas O'Brien, Minji Oh, Knut A. G. Olsen, Cristobal Padilla, Hamsa Padmanabhan, Nikhil Padmanabhan, Nathalie Palanque-Delabrouille, Antonella Palmese, Daniel Pappalardo, Isabelle Pâris, Changbom Park, Anna Patej, John A. Peacock, Hiranya V. Peiris, Xiyan Peng, Will J. Percival, Sandrine Perruchot, Matthew M. Pieri, Richard Pogge, Jennifer E. Pollack, Claire Poppett, Francisco Prada, Abhishek Prakash, Ronald G. Probst, David Rabinowitz, Anand Raichoor, Chang Hee Ree, Alexandre Refregier, Xavier Regal, Beth Reid, Kevin Reil, Mehdi Rezaie, Constance M. Rockosi, Natalie Roe, Samuel Ronayette, Aaron Roodman, Ashley J. Ross, Nicholas P. Ross, Graziano Rossi, Eduardo Rozo, Vanina Ruhlmann-Kleider, Eli S. Rykoff, Cristiano Sabiu, Lado Samushia, Eusebio Sanchez, Javier Sanchez, David J. Schlegel, Michael Schneider, Michael Schubnell, Aurélia Secroun, Uros Seljak, Hee-Jong Seo, Santiago Serrano, Arman Shafieloo, Huanyuan Shan, Ray Sharples, Michael J. Sholl, William V. Shourt, Joseph H. Silber, David R. Silva, Martin M. Sirk, Anze Slosar, Alex Smith, George F. Smoot, Debopam Som, Yong-Seon Song, David Sprayberry, Ryan Staten, Andy Stefanik, Gregory Tarle, Suk Sien Tie, Jeremy L. Tinker, Rita Tojeiro, Francisco Valdes, Octavio Valenzuela, Monica Valluri, Mariana Vargas-Magana, Licia Verde, Alistair R. Walker, Jiali Wang, Yuting Wang, Benjamin A. Weaver, Curtis Weaverdyck, Risa H. Wechsler, David H. Weinberg, Martin White, Qian Yang, Christophe Yeche, Tianmeng Zhang, Gong-Bo Zhao, Yi Zheng, Xu Zhou, Zhimin Zhou, Yaling Zhu, Hu Zou, and Ying Zu. The DESI Experiment Part I: Science,Targeting, and Survey Design. *arXiv:1611.00036 [astro-ph]*, December 2016. arXiv: 1611.00036.

[16] LSST Dark Energy Science Collaboration. Large Synoptic Survey Telescope: Dark Energy Science Collaboration. *arXiv:1211.0310 [astro-ph, physics:hep-ex]*, November 2012. arXiv: 1211.0310.

[17] Euclid Collaboration, A. Blanchard, S. Camera, C. Carbone, V. F. Cardone, S. Casas, S. Clesse, S. Ilić, M. Kilbinger, T. Kitching, M. Kunz, F. Lacasa, E. Linder, E. Majerotto, K. Markovič, M. Martinelli, V. Pettorino, A. Pourtsidou, Z. Sakr,

A. G. Sánchez, D. Sapone, I. Tutusaus, S. Yahia-Cherif, V. Yankelevich, S. Andreon, H. Aussel, A. Balaguera-Antolínez, M. Baldi, S. Bardelli, R. Bender, A. Biviano, D. Bonino, A. Boucaud, E. Bozzo, E. Branchini, S. Brau-Nogue, M. Brescia, J. Brinchmann, C. Burigana, R. Cabanac, V. Capobianco, A. Cappi, J. Carretero, C. S. Carvalho, R. Casas, F. J. Castander, M. Castellano, S. Cavuoti, A. Cimatti, R. Cledassou, C. Colodro-Conde, G. Congedo, C. J. Conselice, L. Conversi, Y. Copin, L. Corcione, J. Coupon, H. M. Courtois, M. Cropper, A. Da Silva, S. de la Torre, D. Di Ferdinando, F. Dubath, F. Ducret, C. A. J. Duncan, X. Dupac, S. Dusini, G. Fabbian, M. Fabricius, S. Farrens, P. Fosalba, S. Fotopoulou, N. Fourmanoit, M. Frailis, E. Franceschi, P. Franzetti, M. Fumana, S. Galeotta, W. Gillard, B. Gillis, C. Giocoli, P. Gómez-Alvarez, J. Graciá-Carpio, F. Grupp, L. Guzzo, H. Hoekstra, F. Hormuth, H. Israel, K. Jahnke, E. Keihanen, S. Kermiche, C. C. Kirkpatrick, R. Kohley, B. Kubik, H. Kurki-Suonio, S. Ligori, P. B. Lilje, I. Lloro, D. Maino, E. Maiorano, O. Marggraf, N. Martinet, F. Marulli, R. Massey, E. Medinaceli, S. Mei, Y. Mellier, B. Metcalf, J. J. Metge, G. Meylan, M. Moresco, L. Moscardini, E. Munari, R. C. Nichol, S. Niemi, A. A. Nucita, C. Padilla, S. Paltani, F. Pasian, W. J. Percival, S. Pires, G. Polenta, M. Poncet, L. Pozzetti, G. D. Racca, F. Raison, A. Renzi, J. Rhodes, E. Romelli, M. Roncarelli, E. Rossetti, R. Saglia, P. Schneider, V. Scottez, A. Secroun, G. Sirri, L. Stanco, J.-L. Starck, F. Sureau, P. Tallada-Crespí, D. Tavagnacco, A. N. Taylor, M. Tenti, I. Tereno, R. Toledo-Moreo, F. Torradeflot, L. Valenziano, T. Vassallo, G. A. Verdoes Kleijn, M. Viel, Y. Wang, A. Zacchei, J. Zoubian, and E. Zucca. Euclid preparation: VII. Forecast validation for Euclid cosmological probes. *A&A*, 642:A191, October 2020. arXiv: 1910.09273.

[18] D. Spergel, N. Gehrels, C. Baltay, D. Bennett, J. Breckinridge, M. Donahue, A. Dressler, B. S. Gaudi, T. Greene, O. Guyon, C. Hirata, J. Kalirai, N. J. Kasdin, B. Macintosh, W. Moos, S. Perlmutter, M. Postman, B. Rauscher, J. Rhodes, Y. Wang, D. Weinberg, D. Benford, M. Hudson, W. S. Jeong, Y. Mellier, W. Traub, T. Yamada, P. Capak, J. Colbert, D. Masters, M. Penny, D. Savransky, D. Stern, N. Zimmerman, R. Barry, L. Bartusek, K. Carpenter, E. Cheng, D. Content, F. Dekens, R. Demers, K. Grady, C. Jackson, G. Kuan, J. Kruk, M. Melton, B. Nemati, B. Parvin, I. Poberezhskiy, C. Peddie, J. Ruffa, J. K. Wallace, A. Whipple, E. Wollack, and F. Zhao. Wide-Field InfrarRed Survey Telescope-Astrophysics Focused Telescope Assets WFIRST-AFTA 2015 Report. *arXiv e-prints*, page arXiv:1503.03757, March 2015.

[19] Will J. Percival, Carlton M. Baugh, Joss Bland-Hawthorn, Terry Bridges, Russell Cannon, Shaun Cole, Matthew Colless, Chris Collins, Warrick Couch, Gavin Dalton,

Roberto De Propris, Simon P. Driver, George Efstathiou, Richard S. Ellis, Carlos S. Frenk, Karl Glazebrook, Carole Jackson, Ofer Lahav, Ian Lewis, Stuart Lumsden, Steve Maddox, Stephen Moody, Peder Norberg, John A. Peacock, Bruce A. Peterson, Will Sutherland, and Keith Taylor. The 2dF Galaxy Redshift Survey: The power spectrum and the matter content of the universe. *arXiv:astro-ph/0105252*, May 2001. arXiv: astro-ph/0105252.

[20] D. G. York. The Sloan Digital Sky Survey: Technical Summary. *The Astronomical Journal*, 120(3):1579–1587, September 2000. arXiv: astro-ph/0006396.

[21] D. J. Eisenstein, I. Zehavi, D. W. Hogg, R. Scoccimarro, M. R. Blanton, R. C. Nichol, R. Scranton, H. Seo, M. Tegmark, Z. Zheng, S. Anderson, J. Annis, N. Bahcall, J. Brinkmann, S. Burles, F. J. Castander, A. Connolly, I. Csabai, M. Doi, M. Fukugita, J. A. Frieman, K. Glazebrook, J. E. Gunn, J. S. Hendry, G. Hennessy, Z. Ivezic, S. Kent, G. R. Knapp, H. Lin, Y. Loh, R. H. Lupton, B. Margon, T. McKay, A. Meiksin, J. A. Munn, A. Pope, M. Richmond, D. Schlegel, D. Schneider, K. Shimasaku, C. Stoughton, M. Strauss, M. SubbaRao, A. S. Szalay, I. Szapudi, D. Tucker, B. Yanny, and D. York. Detection of the Baryon Acoustic Peak in the Large-Scale Correlation Function of SDSS Luminous Red Galaxies. *ApJ*, 633(2):560–574, November 2005. arXiv: astro-ph/0501171.

[22] S. Cole, W. J. Percival, J. A. Peacock, P. Norberg, C. M. Baugh, C. S. Frenk, I. Baldry, J. Bland-Hawthorn, T. Bridges, R. Cannon, M. Colless, C. Collins, W. Couch, N. J. G. Cross, G. Dalton, V. R. Eke, R. De Propris, S. P. Driver, G. Efstathiou, R. S. Ellis, K. Glazebrook, C. Jackson, A. Jenkins, O. Lahav, I. Lewis, S. Lumsden, S. Maddox, D. Madgwick, B. A. Peterson, W. Sutherland, and K. Taylor. The 2dF Galaxy Redshift Survey: Power-spectrum analysis of the final dataset and cosmological implications. *Monthly Notices of the Royal Astronomical Society*, 362(2):505–534, September 2005. arXiv: astro-ph/0501174.

[23] Will J. Percival, Beth A. Reid, Daniel J. Eisenstein, Neta A. Bahcall, Tamas Budavari, Joshua A. Frieman, Masataka Fukugita, James E. Gunn, Zeljko Ivezic, Gillian R. Knapp, Richard G. Kron, Jon Loveday, Robert H. Lupton, Timothy A. McKay, Avery Meiksin, Robert C. Nichol, Adrian C. Pope, David J. Schlegel, Donald P. Schneider, David N. Spergel, Chris Stoughton, Michael A. Strauss, Alexander S. Szalay, Max Tegmark, Michael S. Vogeley, David H. Weinberg, Donald G. York, and Idit Zehavi. Baryon Acoustic Oscillations in the Sloan Digital Sky Survey Data Release 7 Galaxy Sample. *Monthly Notices of the Royal Astronomical Society*, 401(4):2148–2168, February 2010. arXiv: 0907.1660.

[24] Lauren Anderson, Eric Aubourg, Stephen Bailey, Dmitry Bizyaev, Michael Blanton, Adam S. Bolton, J. Brinkmann, Joel R. Brownstein, Angela Burden, Antonio J. Cuesta, Luiz N. A. da Costa, Kyle S. Dawson, Roland de Putter, Daniel J. Eisenstein, James E. Gunn, Hong Guo, Jean-Christophe Hamilton, Paul Harding, Shirley Ho, Klaus Honscheid, Eyal Kazin, D. Kirkby, Jean-Paul Kneib, Antione Labatie, Craig Loomis, Robert H. Lupton, Elena Malanushenko, Viktor Malanushenko, Rachel Mandelbaum, Marc Manera, Claudia Maraston, Cameron K. McBride, Kushal T. Mehta, Olga Mena, Francesco Montesano, Demetri Muna, Robert C. Nichol, Sebastian E. Nuza, Matthew D. Olmstead, Daniel Oravetz, Nikhil Padmanabhan, Nathalie Palanque-Delabrouille, Kaike Pan, John Parejko, Isabelle Paris, Will J. Percival, Patrick Petitjean, Francisco Prada, Beth Reid, Natalie A. Roe, Ashley J. Ross, Nicholas P. Ross, Lado Samushia, Ariel G. Sanchez, David J. Schlegel Donald P. Schneider, Claudia G. Scoccola, Hee-Jong Seo, Erin S. Sheldon, Audrey Simmons, Ramin A. Skibba, Michael A. Strauss, Molly E. C. Swanson, Daniel Thomas, Jeremy L. Tinker, Rita Tojeiro, Mariana Vargas Magana, Licia Verde, Christian Wagner, David A. Wake, Benjamin A. Weaver, David H. Weinberg, Martin White, Xiaoying Xu, Christophe Yeche, Idit Zehavi, and Gong-Bo Zhao. The clustering of galaxies in the SDSS-III Baryon Oscillation Spectroscopic Survey: Baryon Acoustic Oscillations in the Data Release 9 Spectroscopic Galaxy Sample. *Monthly Notices of the Royal Astronomical Society*, 427(4):3435–3467, December 2012. arXiv: 1203.6594.

[25] Michael A. Strauss, David H. Weinberg, Robert H. Lupton, and Vijay K. Narayanan. Spectroscopic Target Selection in the Sloan Digital Sky Survey: The Main Galaxy Sample. *The Astronomical Journal*, 124(3):1810–1824, September 2002. arXiv: astro-ph/0206225.

[26] K. Abazajian. The Seventh Data Release of the Sloan Digital Sky Survey. *ApJS*, 182(2):543–558, June 2009. arXiv: 0812.0649.

[27] Daniel J. Eisenstein, David H. Weinberg, Eric Agol, Hiroaki Aihara, Carlos Allende Prieto, Scott F. Anderson, James A. Arns, Éric Aubourg, Stephen Bailey, Eduardo Balbinot, Robert Barkhouser, Timothy C. Beers, Andreas A. Berlind, Steven J. Bickerton, Dmitry Bizyaev, Michael R. Blanton, John J. Bochanski, Adam S. Bolton, Casey T. Bosman, Jo Bovy, W. N. Brandt, Ben Breslauer, Howard J. Brewington, J. Brinkmann, Peter J. Brown, Joel R. Brownstein, Dan Burger, Nicolas G. Busca, Heather Campbell, Phillip A. Cargile, William C. Carithers, Joleen K. Carlberg, Michael A. Carr, Liang Chang, Yanmei Chen, Cristina Chiappini, Johan Comparat, Natalia Connolly, Marina Cortes, Rupert A. C. Croft, Katia Cunha,

Luiz N. da Costa, James R. A. Davenport, Kyle Dawson, Nathan De Lee, Gustavo F. Porto de Mello, Fernando de Simoni, Janice Dean, Saurav Dhital, Anne Ealet, Garrett L. Ebelke, Edward M. Edmondson, Jacob M. Eiting, Stephanie Escoffier, Massimiliano Esposito, Michael L. Evans, Xiaohui Fan, Bruno Femenía Castellá, Leticia Dutra Ferreira, Greg Fitzgerald, Scott W. Fleming, Andreu Font-Ribera, Eric B. Ford, Peter M. Frinchaboy, Ana Elia García Pérez, B. Scott Gaudi, Jian Ge, Luan Ghezzi, Bruce A. Gillespie, G. Gilmore, Léo Girardi, J. Richard Gott, Andrew Gould, Eva K. Grebel, James E. Gunn, Jean-Christophe Hamilton, Paul Harding, David W. Harris, Suzanne L. Hawley, Frederick R. Hearty, Joseph F. Hennawi, Jonay I. González Hernández, Shirley Ho, David W. Hogg, Jon A. Holtzman, Klaus Honscheid, Naohisa Inada, Inese I. Ivans, Linhua Jiang, Peng Jiang, Jennifer A. Johnson, Cathy Jordan, Wendell P. Jordan, Guinevere Kauffmann, Eyal Kazin, David Kirkby, Mark A. Klaene, G. R. Knapp, Jean-Paul Kneib, C. S. Kochanek, Lars Koesterke, Juna A. Kollmeier, Richard G. Kron, Hubert Lampeitl, Dustin Lang, James E. Lawler, Jean-Marc Le Goff, Brian L. Lee, Young Sun Lee, Jarron M. Leisenring, Yen-Ting Lin, Jian Liu, Daniel C. Long, Craig P. Loomis, Sara Lucatello, Britt Lundgren, Robert H. Lupton, Bo Ma, Zhibo Ma, Nicholas MacDonald, Claude Mack, Suvrath Mahadevan, Marcio A. G. Maia, Steven R. Majewski, Martin Makler, Elena Malanushenko, Viktor Malanushenko, Rachel Mandelbaum, Claudia Maraston, Daniel Margala, Paul Maseman, Karen L. Masters, Cameron K. McBride, Patrick McDonald, Ian D. McGreer, Richard G. McMahon, Olga Mena Requejo, Brice Ménard, Jordi Miralda-Escudé, Heather L. Morrison, Fergal Mullally, Demitri Muna, Hitoshi Murayama, Adam D. Myers, Tracy Naugle, Angelo Fausti Neto, Duy Cuong Nguyen, Robert C. Nichol, David L. Nidever, Robert W. O'Connell, Ricardo L. C. Ogando, Matthew D. Olmstead, Daniel J. Oravetz, Nikhil Padmanabhan, Martin Paegert, Nathalie Palanque-Delabrouille, Kaike Pan, Parul Pandey, John K. Parejko, Isabelle Pâris, Paulo Pellegrini, Joshua Pepper, Will J. Percival, Patrick Petitjean, Robert Pfaffenberger, Janine Pforr, Stefanie Phleps, Christophe Pichon, Matthew M. Pieri, Francisco Prada, Adrian M. Price-Whelan, M. Jordan Raddick, Beatriz H. F. Ramos, I. Neill Reid, Celine Reyle, James Rich, Gordon T. Richards, George H. Rieke, Marcia J. Rieke, Hans-Walter Rix, Annie C. Robin, Helio J. Rocha-Pinto, Constance M. Rockosi, Natalie A. Roe, Emmanuel Rollinde, Ashley J. Ross, Nicholas P. Ross, Bruno Rossetto, Ariel G. Sánchez, Basilio Santiago, Conor Sayres, Ricardo Schiavon, David J. Schlegel, Katharine J. Schlesinger, Sarah J. Schmidt, Donald P. Schneider, Kris Sellgren, Alaina Shelden, Erin Sheldon, Matthew Shetrone, Yiping Shu, John D. Silverman, Jennifer Simmerer, Audrey E. Simmons, Thirupathi Sivarani, M. F. Skrutskie, Anže Slosar, Stephen Smee, Verne V. Smith, Stephanie A. Snedden, Keivan G. Stassun, Oliver Steele, Matthias Steinmetz,

Mark H. Stockett, Todd Stollberg, Michael A. Strauss, Alexander S. Szalay, Masayuki Tanaka, Aniruddha R. Thakar, Daniel Thomas, Jeremy L. Tinker, Benjamin M. Toflemire, Rita Tojeiro, Christy A. Tremonti, Mariana Vargas Magaña, Licia Verde, Nicole P. Vogt, David A. Wake, Xiaoke Wan, Ji Wang, Benjamin A. Weaver, Martin White, Simon D. M. White, John C. Wilson, John P. Wisniewski, W. Michael Wood-Vasey, Brian Yanny, Naoki Yasuda, Christophe Yèche, Donald G. York, Erick Young, Gail Zasowski, Idit Zehavi, and Bo Zhao. SDSS-III: Massive spectroscopic surveys of the distant Universe, the Milky Way, and extra-solar planetary systems. *The Astronomical Journal*, 142(3):72, September 2011.

[28] Kyle S. Dawson, David J. Schlegel, Christopher P. Ahn, Scott F. Anderson, Éric Aubourg, Stephen Bailey, Robert H. Barkhouser, Julian E. Bautista, Alessandra Beifiori, Andreas A. Berlind, Vaishali Bhardwaj, Dmitry Bizyaev, Cullen H. Blake, Michael R. Blanton, Michael Blomqvist, Adam S. Bolton, Arnaud Borde, Jo Bovy, W. N. Brandt, Howard Brewington, Jon Brinkmann, Peter J. Brown, Joel R. Brownstein, Kevin Bundy, N. G. Busca, William Carithers, Aurelio R. Carnero, Michael A. Carr, Yanmei Chen, Johan Comparat, Natalia Connolly, Frances Cope, Rupert A. C. Croft, Antonio J. Cuesta, Luiz N. da Costa, James R. A. Davenport, Timothée Delubac, Roland de Putter, Saurav Dhital, Anne Ealet, Garrett L. Ebelke, Daniel J. Eisenstein, S. Escoffier, Xiaohui Fan, N. Filiz Ak, Hayley Finley, Andreu Font-Ribera, R. Génova-Santos, James E. Gunn, Hong Guo, Daryl Haggard, Patrick B. Hall, Jean-Christophe Hamilton, Ben Harris, David W. Harris, Shirley Ho, David W. Hogg, Diana Holder, Klaus Honscheid, Joe Huehnerhoff, Beatrice Jordan, Wendell P. Jordan, Guinevere Kauffmann, Eyal A. Kazin, David Kirkby, Mark A. Klaene, Jean-Paul Kneib, Jean-Marc Le Goff, Khee-Gan Lee, Daniel C. Long, Craig P. Loomis, Britt Lundgren, Robert H. Lupton, Marcio A. G. Maia, Martin Makler, Elena Malanushenko, Viktor Malanushenko, Rachel Mandelbaum, Marc Manera, Claudia Maraston, Daniel Margala, Karen L. Masters, Cameron K. McBride, Patrick McDonald, Ian D. McGreer, Richard McMahon, Olga Mena, Jordi Miralda-Escudé, Antonio D. Montero-Dorta, Francesco Montesano, Demitri Muna, Adam D. Myers, Tracy Naugle, Robert C. Nichol, Pasquier Noterdaeme, Sebastián E. Nuza, Matthew D. Olmstead, Audrey Oravetz, Daniel J. Oravetz, Russell Owen, Nikhil Padmanabhan, Nathalie Palanque-Delabrouille, Kaike Pan, John K. Parejko, Isabelle Pâris, Will J. Percival, Ismael Pérez-Fournon, Ignasi Pérez-Ràfols, Patrick Petitjean, Robert Pfaffenberger, Janine Pforr, Matthew M. Pieri, Francisco Prada, Adrian M. Price-Whelan, M. Jordan Raddick, Rafael Rebolo, James Rich, Gordon T. Richards, Constance M. Rockosi, Natalie A. Roe, Ashley J. Ross, Nicholas P. Ross, Graziano Rossi, J. A. Rubiño-Martin, Lado Samushia, Ariel G. Sánchez, Conor

Sayres, Sarah J. Schmidt, Donald P. Schneider, C. G. Scóccola, Hee-Jong Seo, Alaina Shelden, Erin Sheldon, Yue Shen, Yiping Shu, Anže Slosar, Stephen A. Smee, Stephanie A. Snedden, Fritz Stauffer, Oliver Steele, Michael A. Strauss, Alina Streblyanska, Nao Suzuki, Molly E. C. Swanson, Tomer Tal, Masayuki Tanaka, Daniel Thomas, Jeremy L. Tinker, Rita Tojeiro, Christy A. Tremonti, M. Vargas Magana, Licia Verde, Matteo Viel, David A. Wake, Mike Watson, Benjamin A. Weaver, David H. Weinberg, Benjamin J. Weiner, Andrew A. West, Martin White, W. M. Wood-Vasey, Christophe Yeche, Idit Zehavi, Gong-Bo Zhao, and Zheng Zheng. The Baryon Oscillation Spectroscopic Survey of SDSS-III. *The Astronomical Journal*, 145(1):10, January 2013. arXiv: 1208.0022.

[29] Michael R Blanton. Sloan Digital Sky Survey IV: Mapping the Milky Way, Nearby Galaxies, and the Distant Universe. *The Astronomical Journal*, page 35, 2017.

[30] Kyle S. Dawson, Jean-Paul Kneib, Will J. Percival, Shadab Alam, Franco D. Albareti, Scott F. Anderson, Eric Armengaud, Éric Aubourg, Stephen Bailey, Julian E. Bautista, Andreas A. Berlind, Matthew A. Bershady, Florian Beutler, Dmitry Bizyaev, Michael R. Blanton, Michael Blomqvist, Adam S. Bolton, Jo Bovy, W. N. Brandt, Jon Brinkmann, Joel R. Brownstein, Etienne Burtin, N. G. Busca, Zheng Cai, Chia-Hsun Chuang, Nicolas Clerc, Johan Comparat, Frances Cope, Rupert A. C. Croft, Irene Cruz-Gonzalez, Luiz N. da Costa, Marie-Claude Cousinou, Jeremy Darling, Axel de la Macorra, Sylvain de la Torre, Timothée Delubac, Hélion du Mas des Bourboux, Tom Dwelly, Anne Ealet, Daniel J. Eisenstein, Michael Eracleous, S. Escoffier, Xiaohui Fan, Alexis Finoguenov, Andreu Font-Ribera, Peter Frinchaboy, Patrick Gaulme, Antonis Georgakakis, Paul Green, Hong Guo, Julien Guy, Shirley Ho, Diana Holder, Joe Huehnerhoff, Timothy Hutchinson, Yipeng Jing, Eric Jullo, Vikrant Kamble, Karen Kinemuchi, David Kirkby, Francisco-Shu Kitaura, Mark A. Klaene, Russ R. Laher, Dustin Lang, Pierre Laurent, Jean-Marc Le Goff, Cheng Li, Yu Liang, Marcos Lima, Qiufan Lin, Weipeng Lin, Yen-Ting Lin, Daniel C. Long, Britt Lundgren, Nicholas MacDonald, Marcio Antonio Geimba Maia, Elena Malanushenko, Viktor Malanushenko, Vivek Mariappan, Cameron K. McBride, Ian D. McGreer, Brice Ménard, Andrea Merloni, Andres Meza, Antonio D. Montero-Dorta, Demitri Muna, Adam D. Myers, Kirpal Nandra, Tracy Naugle, Jeffrey A. Newman, Pasquier Noterdaeme, Peter Nugent, Ricardo Ogando, Matthew D. Olmstead, Audrey Oravetz, Daniel J. Oravetz, Nikhil Padmanabhan, Nathalie Palanque-Delabrouille, Kaike Pan, John K. Parejko, Isabelle Pâris, John A. Peacock, Patrick Petitjean, Matthew M. Pieri, Alice Pisani, Francisco Prada, Abhishek Prakash, Anand Raichoor, Beth Reid, James Rich, Jethro Ridl, Ser-

gio Rodriguez-Torres, Aurelio Carnero Rosell, Ashley J. Ross, Graziano Rossi, John Ruan, Mara Salvato, Conor Sayres, Donald P. Schneider, David J. Schlegel, Uros Seljak, Hee-Jong Seo, Branimir Sesar, Sarah Shandera, Yiping Shu, Anže Slosar, Flavia Sobreira, Alina Streblyanska, Nao Suzuki, Donna Taylor, Charling Tao, Jeremy L. Tinker, Rita Tojeiro, Mariana Vargas-Magaña, Yuting Wang, Benjamin A. Weaver, David H. Weinberg, Martin White, W. M. Wood-Vasey, Christophe Yeche, Zhongxu Zhai, Cheng Zhao, Gong-bo Zhao, Zheng Zheng, Guangtun Ben Zhu, and Hu Zou. THE SDSS-IV EXTENDED BARYON OSCILLATION SPECTROSCOPIC SURVEY: OVERVIEW AND EARLY DATA. *The Astronomical Journal*, 151(2):44, February 2016.

[31] D. Heath Jones, Mike A. Read, Will Saunders, Matthew Colless, Tom Jarrett, Quentin A. Parker, Anthony P. Fairall, Thomas Mauch, Elaine M. Sadler, Fred G. Watson, Donna Burton, Lachlan A. Campbell, Paul Cass, Scott M. Croom, John Dawe, Kristin Fiegert, Leela Frankcombe, Malcolm Hartley, John Huchra, Dionne James, Emma Kirby, Ofer Lahav, John Lucey, Gary A. Mamon, Lesa Moore, Bruce A. Peterson, Sayuri Prior, Dominique Proust, Ken Russell, Vicky Safouris, Ken-ichi Wakamatsu, Eduard Westra, and Mary Williams. The 6dF Galaxy Survey: final redshift release (DR3) and southern large-scale structures. *Monthly Notices of the Royal Astronomical Society*, 399(2):683–698, October 2009.

[32] David Parkinson, Signe Riemer-Sørensen, Chris Blake, Gregory B. Poole, Tamara M. Davis, Sarah Brough, Matthew Colless, Carlos Contreras, Warrick Couch, Scott Croom, Darren Croton, Michael J. Drinkwater, Karl Forster, David Gilbank, Mike Gladders, Karl Glazebrook, Ben Jelliffe, Russell J. Jurek, I.-hui Li, Barry Madore, D. Christopher Martin, Kevin Pimbblet, Michael Pracy, Rob Sharp, Emily Wisnioski, David Woods, Ted K. Wyder, and H. K. C. Yee. The WiggleZ Dark Energy Survey: Final data release and cosmological results. *Phys. Rev. D*, 86(10):103518, November 2012. arXiv: 1210.2130.

[33] Max Tegmark. Measuring Cosmological Parameters with Galaxy Surveys. *Phys. Rev. Lett.*, 79(20):3806–3809, November 1997.

[34] Martin White, Yong-Seon Song, and Will J. Percival. Forecasting Cosmological Constraints from Redshift Surveys. *Monthly Notices of the Royal Astronomical Society*, 397(3):1348–1354, August 2009. arXiv: 0810.1518.

[35] Andreu Font-Ribera, Patrick McDonald, Nick Mostek, Beth A. Reid, Hee-Jong Seo, and Anže Slosar. DESI and other dark energy experiments in the era of neutrino mass

measurements. *J. Cosmol. Astropart. Phys.*, 2014(05):023–023, May 2014. arXiv: 1308.4164.

[36] Gong-Bo Zhao, Yuting Wang, Ashley J. Ross, Sarah Shandera, Will J. Percival, Kyle S. Dawson, Jean-Paul Kneib, Adam D. Myers, Joel R. Brownstein, Johan Comparat, Timothée Delubac, Pengyuan Gao, Alireza Hojjati, Kazuya Koyama, Cameron K. McBride, Andrés Meza, Jeffrey A. Newman, Nathalie Palanque-Delabrouille, Levon Pogosian, Francisco Prada, Graziano Rossi, Donald P. Schneider, Hee-Jong Seo, Charling Tao, Dandan Wang, Christophe Yèche, Hanyu Zhang, Yuecheng Zhang, Xu Zhou, Fangzhou Zhu, and Hu Zou. The extended Baryon Oscillation Spectroscopic Survey (eBOSS): a cosmological forecast. *arXiv:1510.08216 [astro-ph]*, February 2016. arXiv: 1510.08216.

[37] R. A. Fisher. The Logic of Inductive Inference. *Journal of the Royal Statistical Society*, 98(1):39–82, 1935. Publisher: [Wiley, Royal Statistical Society].

[38] Rossana Ruggeri and Chris Blake. How accurately can we measure the baryon acoustic oscillation feature? *Monthly Notices of the Royal Astronomical Society*, 498(3):3744–3757, September 2020. arXiv: 1909.13011.

[39] T. Treu, G. Roberts-Borsani, M. Bradac, G. Brammer, A. Fontana, A. Henry, C. Mason, T. Morishita, L. Pentericci, X. Wang, A. Acebron, M. Bagley, P. Bergamini, D. Belfiori, A. Bonchi, K. Boyett, K. Boutsia, A. Calabro, G. B. Caminha, M. Castellano, A. Dressler, K. Glazebrook, C. Grillo, C. Jacobs, T. Jones, P. Kelly, N. Leethochawalit, M. Malkan, D. Marchesini, S. Mascia, A. Mercurio, E. Merlin, T. Nanayakkara, M. Nonino, D. Paris, B. Poggianti, P. Rosati, P. Santini, C. Scarlata, H. Shipley, V. Strait, M. Trenti, C. Tubthong, E. Vanzella, B. Vulcani, and L. Yang. The glass james webb space telescope early release science program. i. survey design and release plans. 2022.

[40] Yun Wang, Zhongxu Zhai, Anahita Alavi, Elena Massara, Alice Pisani, Andrew Benson, Christopher M. Hirata, Lado Samushia, David H. Weinberg, James Colbert, Olivier Doré, Tim Eifler, Chen Heinrich, Shirley Ho, Elisabeth Krause, Nikhil Padmanabhan, David Spergel, and Harry I. Teplitz. The high latitude spectroscopic survey on the nancy grace roman space telescope. 928(1):1.

[41] Stephen A. Smee, James E. Gunn, Alan Uomoto, Natalie Roe, David Schlegel, Constance M. Rockosi, Michael A. Carr, French Leger, Kyle S. Dawson, Matthew D. Olmstead, Jon Brinkmann, Russell Owen, Robert H. Barkhouser, Klaus Honscheid, Paul Harding, Dan Long, Robert H. Lupton, Craig Loomis, Lauren Anderson, James

Annis, Mariangela Bernardi, Vaishali Bhardwaj, Dmitry Bizyaev, Adam S. Bolton, Howard Brewington, John W. Briggs, Scott Burles, James G. Burns, Francisco Javier Castander, Andrew Connolly, James R. A. Davenport, Garrett Ebelke, Harland Epps, Paul D. Feldman, Scott D. Friedman, Joshua Frieman, Timothy Heckman, Charles L. Hull, Gillian R. Knapp, David M. Lawrence, Jon Loveday, Edward J. Mannery, Elena Malanushenko, Viktor Malanushenko, Aronne James Merrelli, Demitri Muna, Peter R. Newman, Robert C. Nichol, Daniel Oravetz, Kaike Pan, Adrian C. Pope, Paul G. Ricketts, Alaina Shelden, Dale Sandford, Walter Siegmund, Audrey Simmons, D. Shane Smith, Stephanie Snedden, Donald P. Schneider, Mark SubbaRao, Christy Tremonti, Patrick Waddell, and Donald G. York. THE MULTI-OBJECT, FIBER-FED SPECTROGRAPHS FOR THE SLOAN DIGITAL SKY SURVEY AND THE BARYON OSCILLATION SPECTROSCOPIC SURVEY. 146(2):32.

[42] Joseph Harry Silber, Parker Fagrelius, Kevin Fanning, Michael Schubnell, Jessica Nicole Aguilar, Steven Ahlen, Jon Ameel, Otger Ballester, Charles Baltay, Chris Bebek, Dominic Benton Beard, Robert Besuner, Laia Cardiel-Sas, Ricard Casas, Francisco Javier Castander, Todd Claybaugh, Carl Dobson, Yutong Duan, Patrick Dunlop, Jerry Edelstein, William T. Emmet, Ann Elliott, Matthew Evatt, Irena Gershkovich, Julien Guy, Stu Harris, Henry Heetderks, Ian Heetderks, Klaus Honscheid, Jose Maria Illa, Patrick Jelinsky, Sharon R. Jelinsky, Jorge Jimenez, Armin Karcher, Stephen Kent, David Kirkby, Jean-Paul Kneib, Andrew Lambert, Mike Lampton, Daniela Leitner, Michael Levi, Jeremy McCauley, Aaron Meisner, Timothy N. Miller, Ramon Miquel, Juliá Mundet, Claire Poppett, David Rabinowitz, Kevin Reil, David Roman, David Schlegel, Santiago Serrano, William Van Shourt, David Sprayberry, Gregory Tarlé, Suk Sien Tie, Curtis Weaverdyck, Kai Zhang, Marco Azzaro, Stephen Bailey, Santiago Becerril, Tami Blackwell, Mohamed Bouri, David Brooks, Elizabeth Buckley-Geer, Jose Peñate Castro, Mark Derwent, Arjun Dey, Govinda Dhungana, Peter Doel, Daniel J. Eisenstein, Nasib Fahim, Juan Garcia-Bellido, Enrique Gaztañaga, Satya Gontcho A Gontcho, Gaston Gutierrez, Philipp Hörler, Robert Kehoe, Theodore Kisner, Anthony Kremin, Luzius Kronig, Martin Landriau, Laurent Le Guillou, Paul Martini, John Moustakas, Nathalie Palanque-Delabrouille, Xiyan Peng, Will Percival, Francisco Prada, Carlos Allende Prieto, Guillermo Gonzalez de Rivera, Eusebio Sanchez, Justo Sanchez, Ray Sharples, Marcelle Soares-Santos, Edward Schlafly, Benjamin Alan Weaver, Zhimin Zhou, Yaling Zhu, and Hu Zou. The robotic multi-object focal plane system of the dark energy spectroscopic instrument (desi). 2022.

[43] L. Perivolaropoulos and F. Skara. Challenges for lambda cdm: An update. 95:101659,

dec 2022.

[44] Paul Shah, Pablo Lemos, and Ofer Lahav. A buyer's guide to the hubble constant. 29(1), dec 2021.

[45] Elcio Abdalla, Guillermo Franco Abellán, Amin Aboubrahim, Adriano Agnello, Özgür Akarsu, Yashar Akrami, George Alestas, Daniel Aloni, Luca Amendola, Luis A. Anchordoqui, Richard I. Anderson, Nikki Arendse, Marika Asgari, Mario Ballardini, Vernon Barger, Spyros Basilakos, Ronaldo C. Batista, Elia S. Battistelli, Richard Battye, Micol Benetti, David Benisty, Asher Berlin, Paolo de Bernardis, Emanuele Berti, Bohdan Bidenko, Simon Birrer, John P. Blakeslee, Kimberly K. Boddy, Clecio R. Bom, Alexander Bonilla, Nicola Borghi, François R. Bouchet, Matteo Braglia, Thomas Buchert, Elizabeth Buckley-Geer, Erminia Calabrese, Robert R. Caldwell, David Camarena, Salvatore Capozziello, Stefano Casertano, Geoff C.-F. Chen, Jens Chluba, Angela Chen, Hsin-Yu Chen, Anton Chudaykin, Michele Cicoli, Craig J. Copi, Fred Courbin, Francis-Yan Cyr-Racine, Bożena Czerny, Maria Dainotti, Guido D'Amico, Anne-Christine Davis, Javier de Cruz Pérez, Jaume de Haro, Jacques Delabrouille, Peter B. Denton, Suhail Dhawan, Keith R. Dienes, Eleonora Di Valentino, Pu Du, Dominique Eckert, Celia Escamilla-Rivera, Agnès Ferté, Fabio Finelli, Pablo Fosalba, Wendy L. Freedman, Noemi Frusciante, Enrique Gaztañaga, William Giarè, Elena Giusarma, Adrià Gómez-Valent, Will Handley, Ian Harrison, Luke Hart, Dhiraj Kumar Hazra, Alan Heavens, Asta Heinesen, Hendrik Hildebrandt, J. Colin Hill, Natalie B. Hogg, Daniel E. Holz, Deanna C. Hooper, Nikoo Hosseininejad, Dragan Huterer, Mustapha Ishak, Mikhail M. Ivanov, Andrew H. Jaffe, In Sung Jang, Karsten Jedamzik, Raul Jimenez, Melissa Joseph, Shahab Joudaki, Marc Kamionkowski, Tanvi Karwal, Lavrentios Kazantzidis, Ryan E. Keeley, Michael Klasen, Eiichiro Komatsu, Léon V.E. Koopmans, Suresh Kumar, Luca Lamagna, Ruth Lazkoz, Chung-Chi Lee, Julien Lesgourgues, Jackson Levi Said, Tiffany R. Lewis, Benjamin L'Huillier, Matteo Lucca, Roy Maartens, Lucas M. Macri, Danny Marfatia, Valerio Marra, Carlos J.A.P. Martins, Silvia Masi, Sabino Matarrese, Arindam Mazumdar, Alessandro Melchiorri, Olga Mena, Laura Mersini-Houghton, James Mertens, Dinko Milaković, Yuto Minami, Vivian Miranda, Cristian Moreno-Pulido, Michele Moresco, David F. Mota, Emil Mottola, Simone Mozzon, Jessica Muir, Ankan Mukherjee, Suvodip Mukherjee, Pavel Naselsky, Pran Nath, Savvas Nesseris, Florian Niedermann, Alessio Notari, Rafael C. Nunes, Eoin Ó Colgáin, Kayla A. Owens, Emre Özülker, Francesco Pace, Andronikos Paliathanasis, Antonella Palmese, Supriya Pan, Daniela Paoletti, Santiago E. Perez Bergliaffa, Leandros Perivolaropoulos, Dominic W. Pesce, Valeria Pettorino, Oliver H.E. Philcox,

Levon Pogosian, Vivian Poulin, Gaspard Poulot, Marco Raveri, Mark J. Reid, Fabrizio Renzi, Adam G. Riess, Vivian I. Sabla, Paolo Salucci, Vincenzo Salzano, Emmanuel N. Saridakis, Bangalore S. Sathyaprakash, Martin Schmaltz, Nils Schöneberg, Dan Scolnic, Anjan A. Sen, Neelima Sehgal, Arman Shafieloo, M.M. Sheikh-Jabbari, Joseph Silk, Alessandra Silvestri, Foteini Skara, Martin S. Sloth, Marcelle Soares-Santos, Joan Solà Peracaula, Yu-Yang Songsheng, Jorge F. Soriano, Denitsa Staicova, Glenn D. Starkman, István Szapudi, Elsa M. Teixeira, Brooks Thomas, Tommaso Treu, Emery Trott, Carsten van de Bruck, J. Alberto Vazquez, Licia Verde, Luca Visinelli, Deng Wang, Jian-Min Wang, Shao-Jiang Wang, Richard Watkins, Scott Watson, John K. Webb, Neal Weiner, Amanda Weltman, Samuel J. Witte, Radosław Wojtak, Anil Kumar Yadav, Weiqiang Yang, Gong-Bo Zhao, and Miguel Zumalacárregui. Cosmology intertwined: A review of the particle physics, astrophysics, and cosmology associated with the cosmological tensions and anomalies. 34:49–211, jun 2022.

[46] Eleonora Di Valentino, Olga Mena, Supriya Pan, Luca Visinelli, Weiqiang Yang, Alessandro Melchiorri, David F Mota, Adam G Riess, and Joseph Silk. In the realm of the hubble tension—a review of solutions. *Classical and Quantum Gravity*, 38(15):153001, jul 2021.

[47] A. J. S. Hamilton. Linear redshift distortions: A review. pages 185–275, 1998.

[48] Nick Kaiser. Clustering in real space and in redshift space. *Monthly Notices of the Royal Astronomical Society*, 227(1):1–21, 07 1987.

[49] E. Hivon, F. R. Bouchet, S. Colombi, and R. Juszkiewicz. Redshift distortions of clustering: A lagrangian approach. 1994.

[50] L. Verde, A. F. Heavens, S. Matarrese, and L. Moscardini. Large-scale bias in the universe - II. redshift-space bispectrum. *Monthly Notices of the Royal Astronomical Society*, 300(3):747–756, nov 1998.

[51] Roman Scoccimarro, H. M. P. Couchman, and Joshua A. Frieman. The bispectrum as a signature of gravitational instability in redshift space. *The Astrophysical Journal*, 517(2):531–540, jun 1999.

[52] P. J. E. Peebles and M. G. Hauser. Statistical analysis of catalogs of extragalactic objects. III. the shane-wirtanen and zwicky catalogs. 28:19.

[53] M. Davis and P. J. E. Peebles. A survey of galaxy redshifts. v - the two-point position and velocity correlations. 267:465.

[54] Stephen D Landy and Alexander S Szalay. Bias and variance of angular correlation functions. *The Astrophysical Journal*, 412:64–71, 1993.

[55] J. A. Peacock and S. J. Dodds. Reconstructing the linear power spectrum of cosmological mass fluctuations. *Monthly Notices of the Royal Astronomical Society*, 267(4):1020–1034, 04 1994.

[56] Beth A Reid and Martin White. Towards an accurate model of the redshiftspace clustering of haloes in the quasilinear regime. *Monthly Notices of the Royal Astronomical Society*, page 15, 2011.

[57] Francisco Villaescusa-Navarro, ChangHoon Hahn, Elena Massara, Arka Banerjee, Ana Maria Delgado, Doogesh Kodi Ramanah, Tom Charnock, Elena Giusarma, Yin Li, Erwan Allys, Antoine Brochard, Cora Uhlemann, Chi-Ting Chiang, Siyu He, Alice Pisani, Andrej Obuljen, Yu Feng, Emanuele Castorina, Gabriella Contardo, Christina D. Kreisch, Andrina Nicola, Justin Alsing, Roman Scoccimarro, Licia Verde, Matteo Viel, Shirley Ho, Stephane Mallat, Benjamin Wandelt, and David N. Spergel. The quijote simulations. *The Astrophysical Journal Supplement Series*, 250(1):2, aug 2020.

[58] Planck Collaboration, P. A. R. Ade, N. Aghanim, C. Armitage-Caplan, M. Arnaud, M. Ashdown, F. Atrio-Barandela, J. Aumont, C. Baccigalupi, A. J. Banday, R. B. Barreiro, J. G. Bartlett, E. Battaner, K. Benabed, A. Benoît, A. Benoit-Lévy, J.-P. Bernard, M. Bersanelli, P. Bielewicz, J. Bobin, J. J. Bock, A. Bonaldi, J. R. Bond, J. Borrill, F. R. Bouchet, M. Bridges, M. Bucher, C. Burigana, R. C. Butler, E. Calabrese, B. Cappellini, J.-F. Cardoso, A. Catalano, A. Challinor, A. Chamballu, R.-R. Chary, X. Chen, H. C. Chiang, L.-Y Chiang, P. R. Christensen, S. Church, D. L. Clements, S. Colombi, L. P. L. Colombo, F. Couchot, A. Coulais, B. P. Crill, A. Curto, F. Cuttaia, L. Danese, R. D. Davies, R. J. Davis, P. de Bernardis, A. de Rosa, G. de Zotti, J. Delabrouille, J.-M. Delouis, F.-X. Désert, C. Dickinson, J. M. Diego, K. Dolag, H. Dole, S. Donzelli, O. Doré, M. Douspis, J. Dunkley, X. Dupac, G. Efstathiou, F. Elsner, T. A. Enßlin, H. K. Eriksen, F. Finelli, O. Forni, M. Frailis, A. A. Fraisse, E. Franceschi, T. C. Gaier, S. Galeotta, S. Galli, K. Ganga, M. Giard, G. Giardino, Y. Giraud-Héraud, E. Gjerløw, J. González-Nuevo, K. M. Górski, S. Gratton, A. Gregorio, A. Gruppuso, J. E. Gudmundsson, J. Haissinski, J. Hamann, F. K. Hansen, D. Hanson, D. Harrison, S. Henrot-Versillé, C. Hernández-Monteagudo, D. Herranz, S. R. Hildebrandt, E. Hivon, M. Hobson, W. A. Holmes, A. Hornstrup, Z. Hou, W. Hovest, K. M. Huffenberger, A. H. Jaffe, T. R. Jaffe, J. Jewell, W. C. Jones, M. Juvela, E. Keihänen, R. Keskitalo, T. S. Kisner, R. Kneissl,

J. Knoche, L. Knox, M. Kunz, H. Kurki-Suonio, G. Lagache, A. Lähteenmäki, J.-M. Lamarre, A. Lasenby, M. Lattanzi, R. J. Laureijs, C. R. Lawrence, S. Leach, J. P. Leahy, R. Leonardi, J. León-Tavares, J. Lesgourgues, A. Lewis, M. Liguori, P. B. Lilje, M. Linden-Vørnle, M. López-Caniego, P. M. Lubin, J. F. Macías-Pérez, B. Maffei, D. Maino, N. Mandolesi, M. Maris, D. J. Marshall, P. G. Martin, E. Martínez-González, S. Masi, M. Massardi, S. Matarrese, F. Matthai, P. Mazzotta, P. R. Meinhold, A. Melchiorri, J.-B. Melin, L. Mendes, E. Menegoni, A. Mennella, M. Migliaccio, M. Millea, S. Mitra, M.-A. Miville-Deschênes, A. Moneti, L. Montier, G. Morgante, D. Mortlock, A. Moss, D. Munshi, J. A. Murphy, P. Naselsky, F. Nati, P. Natoli, C. B. Netterfield, H. U. Nørgaard-Nielsen, F. Noviello, D. Novikov, I. Novikov, I. J. O'Dwyer, S. Osborne, C. A. Oxborrow, F. Paci, L. Pagano, F. Pajot, R. Paladini, D. Paoletti, B. Partridge, F. Pasian, G. Patanchon, D. Pearson, T. J. Pearson, H. V. Peiris, O. Perdereau, L. Perotto, F. Perrotta, V. Pettorino, F. Piacentini, M. Piat, E. Pierpaoli, D. Pietrobon, S. Plaszczynski, P. Platania, E. Pointecouteau, G. Polenta, N. Ponthieu, L. Popa, T. Poutanen, G. W. Pratt, G. Prézeau, S. Prunet, J.-L. Puget, J. P. Rachen, W. T. Reach, R. Rebolo, M. Reinecke, M. Remazeilles, C. Renault, S. Ricciardi, T. Riller, I. Ristorcelli, G. Rocha, C. Rosset, G. Roudier, M. Rowan-Robinson, J. A. Rubiño-Martín, B. Rusholme, M. Sandri, D. Santos, M. Savelainen, G. Savini, D. Scott, M. D. Seiffert, E. P. S. Shellard, L. D. Spencer, J.-L. Starck, V. Stolyarov, R. Stompor, R. Sudiwala, R. Sunyaev, F. Sureau, D. Sutton, A.-S. Suur-Uski, J.-F. Sygnet, J. A. Tauber, D. Tavagnacco, L. Terenzi, L. Toffolatti, M. Tomasi, M. Tristram, M. Tucci, J. Tuovinen, M. Türler, G. Umana, L. Valenziano, J. Valiviita, B. Van Tent, P. Vielva, F. Villa, N. Vittorio, L. A. Wade, B. D. Wandelt, I. K. Wehus, M. White, S. D. M. White, A. Wilkinson, D. Yvon, A. Zacchei, and A. Zonca. *Planck* 2013 results. XVI. Cosmological parameters. *A&A*, 571:A16, November 2014.

[59] Gary Hinshaw, D Larson, Eiichiro Komatsu, David N Spergel, CLaa Bennett, Joanna Dunkley, MR Nolta, M Halpern, RS Hill, N Odegard, et al. Nine-year wilkinson microwave anisotropy probe (wmap) observations: cosmological parameter results. *The Astrophysical Journal Supplement Series*, 208(2):19, 2013.

[60] Matthew Colless, G. B. Dalton, S. J. Maddox, W. J. Sutherland, P. Norberg, S. Cole, J. Bland-Hawthorn, T. J. Bridges, R. D. Cannon, C. A. Collins, W. J. Couch, N. G. J. Cross, K. Deeley, R. DePropris, S. P. Driver, G. Efstathiou, R. S. Ellis, C. S. Frenk, K. Glazebrook, C. A. Jackson, O. Lahav, I. J. Lewis, S. L. Lumsden, D. S. Madgwick, J. A. Peacock, B. A. Peterson, I. A. Price, M. Seaborne, and K. Taylor. The

2dF Galaxy Redshift Survey: Spectra and redshifts. *Monthly Notices of the Royal Astronomical Society*, 328(4):1039–1063, December 2001. arXiv: astro-ph/0106498.

[61] Donald G. York, J. Adelman, John E. Anderson, Jr., Scott F. Anderson, James Annis, Neta A. Bahcall, J. A. Bakken, Robert Barkhouser, Steven Bastian, Eileen Berman, William N. Boroski, Steve Bracker, Charlie Briegel, John W. Briggs, J. Brinkmann, Robert Brunner, Scott Burles, Larry Carey, Michael A. Carr, Francisco J. Castander, Bing Chen, Patrick L. Colestock, A. J. Connolly, J. H. Crocker, István Csabai, Paul C. Czarapata, John Eric Davis, Mamoru Doi, Tom Dombeck, Daniel Eisenstein, Nancy Ellman, Brian R. Elms, Michael L. Evans, Xiaohui Fan, Glenn R. Federwitz, Larry Fiscelli, Scott Friedman, Joshua A. Frieman, Masataka Fukugita, Bruce Gillespie, James E. Gunn, Vijay K. Gurbani, Ernst de Haas, Merle Haldeman, Frederick H. Harris, J. Hayes, Timothy M. Heckman, G. S. Hennessy, Robert B. Hindsley, Scott Holm, Donald J. Holmgren, Chi-hao Huang, Charles Hull, Don Husby, Shin-Ichi Ichikawa, Takashi Ichikawa, Željko Ivezić, Stephen Kent, Rita S. J. Kim, E. Kinney, Mark Klaene, A. N. Kleinman, S. Kleinman, G. R. Knapp, John Korienek, Richard G. Kron, Peter Z. Kunszt, D. Q. Lamb, B. Lee, R. French Leger, Siriluk Limmongkol, Carl Lindenmeyer, Daniel C. Long, Craig Loomis, Jon Loveday, Rich Lucinio, Robert H. Lupton, Bryan MacKinnon, Edward J. Mannery, P. M. Mantsch, Bruce Margon, Peregrine McGehee, Timothy A. McKay, Avery Meiksin, Aronne Merelli, David G. Monet, Jeffrey A. Munn, Vijay K. Narayanan, Thomas Nash, Eric Neilsen, Rich Neswold, Heidi Jo Newberg, R. C. Nichol, Tom Nicinski, Mario Nonino, Norio Okada, Sadanori Okamura, Jeremiah P. Ostriker, Russell Owen, A. George Pauls, John Peoples, R. L. Peterson, Donald Petravick, Jeffrey R. Pier, Adrian Pope, Ruth Pordes, Angela Prosapio, Ron Rechenmacher, Thomas R. Quinn, Gordon T. Richards, Michael W. Richmond, Claudio H. Rivetta, Constance M. Rockosi, Kurt Ruthmansdorfer, Dale Sandford, David J. Schlegel, Donald P. Schneider, Maki Sekiguchi, Gary Sergey, Kazuhiro Shimasaku, Walter A. Siegmund, Stephen Smee, J. Allyn Smith, S. Snedden, R. Stone, Chris Stoughton, Michael A. Strauss, Christopher Stubbs, Mark SubbaRao, Alexander S. Szalay, Istvan Szapudi, Gyula P. Szokoly, Anirudda R. Thakar, Christy Tremonti, Douglas L. Tucker, Alan Uomoto, Dan Vanden Berk, Michael S. Vogeley, Patrick Waddell, Shu-i Wang, Masaru Watanabe, David H. Weinberg, Brian Yanny, and Naoki Yasuda. The sloan digital sky survey: Technical summary. *The Astronomical Journal*, 120(3):1579–1587, Sep 2000.

[62] Florian Beutler, Chris Blake, Matthew Colless, D. Heath Jones, Lister Staveley-Smith, Lachlan Campbell, Quentin Parker, Will Saunders, and Fred Watson. The 6dF Galaxy Survey: Baryon Acoustic Oscillations and the Local Hubble Constant.

Monthly Notices of the Royal Astronomical Society, 416(4):3017–3032, October 2011. arXiv: 1106.3366.

[63] Cullan Howlett, Ashley J. Ross, Lado Samushia, Will J. Percival, and Marc Manera. The Clustering of the SDSS Main Galaxy Sample II: Mock galaxy catalogues and a measurement of the growth of structure from Redshift Space Distortions at \$z=0.15\$. *Monthly Notices of the Royal Astronomical Society*, 449(1):848–866, May 2015. arXiv: 1409.3238.

[64] Shadab Alam, Metin Ata, Stephen Bailey, Florian Beutler, Dmitry Bizyaev, Jonathan A. Blazek, Adam S. Bolton, Joel R. Brownstein, Angela Burden, Chia-Hsun Chuang, Johan Comparat, Antonio J. Cuesta, Kyle S. Dawson, Daniel J. Eisenstein, Stephanie Escoffier, Héctor Gil-Marín, Jan Niklas Grieb, Nick Hand, Shirley Ho, Karen Kinemuchi, David Kirkby, Francisco Kitaura, Elena Malanushenko, Viktor Malanushenko, Claudia Maraston, Cameron K. McBride, Robert C. Nichol, Matthew D. Olmstead, Daniel Oravetz, Nikhil Padmanabhan, Nathalie Palanque-Delabrouille, Kaike Pan, Marcos Pellejero-Ibanez, Will J. Percival, Patrick Petitjean, Francisco Prada, Adrian M. Price-Whelan, Beth A. Reid, Sergio A. Rodríguez-Torres, Natalie A. Roe, Ashley J. Ross, Nicholas P. Ross, Graziano Rossi, Jose Alberto Rubiño-Martín, Ariel G. Sánchez, Shun Saito, Salvador Salazar-Albornoz, Lado Samushia, Siddharth Satpathy, Claudia G. Scóccola, David J. Schlegel, Donald P. Schneider, Hee-Jong Seo, Audrey Simmons, Anže Slosar, Michael A. Strauss, Molly E. C. Swanson, Daniel Thomas, Jeremy L. Tinker, Rita Tojeiro, Mariana Vargas Magaña, Jose Alberto Vazquez, Licia Verde, David A. Wake, Yuting Wang, David H. Weinberg, Martin White, W. Michael Wood-Vasey, Christophe Yèche, Idit Zehavi, Zhongxu Zhai, and Gong-Bo Zhao. The clustering of galaxies in the completed SDSS-III baryon oscillation spectroscopic survey: cosmological analysis of the DR12 galaxy sample. *Monthly Notices of the Royal Astronomical Society*, 470(3):2617–2652, 09 2017.

[65] Julian E. Bautista, Romain Paviot, Mariana Vargas Magaña, Sylvain de la Torre, Sebastien Fromenteau, Hector Gil-Marín, Ashley J. Ross, Etienne Burtin, Kyle S. Dawson, Jiamin Hou, Jean-Paul Kneib, Arnaud de Mattia, Will J. Percival, Graziano Rossi, Rita Tojeiro, Cheng Zhao, Gong-Bo Zhao, Shadab Alam, Joel Brownstein, Michael J. Chapman, Peter D. Choi, Chia-Hsun Chuang, Stéphanie Escoffier, Axel de la Macorra, Hélion du Mas des Bourboux, Faizan G. Mohammad, Jeongin Moon, Eva-Maria Müller, Seshadri Nadathur, Jeffrey A. Newman, Donald Schneider, Hee-Jong Seo, and Yuting Wang. The completed SDSS-IV extended baryon oscillation spectroscopic survey: measurement of the BAO and growth rate of structure of

the luminous red galaxy sample from the anisotropic correlation function between redshifts 0.6 and 1. *Monthly Notices of the Royal Astronomical Society*, 500(1):736–762, 11 2020.

[66] Richard Neveux, Etienne Burtin, Arnaud de Mattia, Alex Smith, Ashley J. Ross, Jiamin Hou, Julian Bautista, Jonathan Brinkmann, Chia-Hsun Chuang, Kyle S. Dawson, Héctor Gil-Marín, Brad W. Lyke, Axel de la Macorra, Hélion du Mas des Bourboux, Eva-Maria Müller, Adam D. Myers, Jeffrey A. Newman, Will J. Percival, Graziano Rossi, Donald Schneider, M. Vivek, Pauline Zarrouk, Cheng Zhao, and Gong-Bo Zhao. The Completed SDSS-IV extended Baryon Oscillation Spectroscopic Survey: BAO and RSD measurements from the anisotropic power spectrum of the Quasar sample between redshift 0.8 and 2.2. *arXiv:2007.08999 [astro-ph]*, July 2020. arXiv: 2007.08999.

[67] Chris Blake, Sarah Brough, Matthew Colless, Carlos Contreras, Warrick Couch, Scott Croom, Darren Croton, Tamara Davis, Michael J. Drinkwater, Karl Forster, David Gilbank, Mike Gladders, Karl Glazebrook, Ben Jelliffe, Russell J. Jurek, I.-hui Li, Barry Madore, Chris Martin, Kevin Pimbblet, Gregory B. Poole, Michael Pracy, Rob Sharp, Emily Wisnioski, David Woods, Ted Wyder, and Howard Yee. The WiggleZ Dark Energy Survey: Joint measurements of the expansion and growth history at z < 1. *Monthly Notices of the Royal Astronomical Society*, 425(1):405–414, September 2012. arXiv: 1204.3674.

[68] Max Tegmark, Andy Taylor, and Alan Heavens. Karhunen-Loeve eigenvalue problems in cosmology: how should we tackle large data sets? *ApJ*, 480(1):22–35, May 1997. arXiv: astro-ph/9603021.

[69] Hee-Jong Seo and Daniel J. Eisenstein. Improved forecasts for the baryon acoustic oscillations and cosmological distance scale. *ApJ*, 665(1):14–24, August 2007. arXiv: astro-ph/0701079.

[70] Daniel J. Eisenstein and Wayne Hu. Baryonic Features in the Matter Transfer Function. *ApJ*, 496(2):605–614, April 1998.

[71] P. J. E. Peebles. Tracing galaxy orbits back in time. *ApJ*, 344:L53, September 1989.

[72] Daniel J. Eisenstein, Hee-Jong Seo, Edwin Sirko, and David N. Spergel. Improving Cosmological Distance Measurements by Reconstruction of the Baryon Acoustic Peak. *ApJ*, 664(2):675–679, August 2007.

[73] Florian Beutler, Hee-Jong Seo, Shun Saito, Chia-Hsun Chuang, Antonio J. Cuesta, Daniel J. Eisenstein, Héctor Gil-Marín, Jan Niklas Grieb, Nick Hand, Francisco-Shu Kitaura, Chirag Modi, Robert C. Nichol, Matthew D. Olmstead, Will J. Percival, Francisco Prada, Ariel G. Sánchez, Sergio Rodriguez-Torres, Ashley J. Ross, Nicholas P. Ross, Donald P. Schneider, Jeremy Tinker, Rita Tojeiro, and Mariana Vargas-Magaña. The clustering of galaxies in the completed SDSS-III Baryon Oscillation Spectroscopic Survey: anisotropic galaxy clustering in Fourier space. *Mon. Not. R. Astron. Soc.*, 466(2):2242–2260, April 2017.

[74] Teppei Okumura, Uros Seljak, Patrick McDonald, and Vincent Desjacques. Distribution function approach to redshift space distortions. Part II: N-body simulations. *arXiv:1109.1609 [astro-ph]*, February 2012. arXiv: 1109.1609.

[75] Pauline Zarrouk, Etienne Burtin, Hector Gil-Marin, Ashley J. Ross, Rita Tojeiro, Isabelle Paris, Kyle S. Dawson, Adam D. Myers, Will J. Percival, Chia-Hsun Chuang, Gong-Bo Zhao, Julian Bautista, Johan Comparat, Violeta Gonzalez-Perez, Salman Habib, Katrin Heitmann, Jiamin Hou, Pierre Laurent, Jean-Marc Le Goff, Francisco Prada, Sergio A. Rodriguez-Torres, Graziano Rossi, Rossana Ruggeri, Ariel G. Sanchez, Donald P. Schneider, Jeremy L. Tinker, Yuting Wang, Christophe Yèche, Falk Baumgarten, Joel R. Brownstein, Sylvain de la Torre, Hélion du Mas des Bourboux, Jean-Paul Kneib, Nathalie Palanque-Delabrouille, John Peacock, Patrick Petitjean, Hee-Jong Seo, and Cheng Zhao. The clustering of the SDSS-IV extended Baryon Oscillation Spectroscopic Survey DR14 quasar sample: measurement of the growth rate of structure from the anisotropic correlation function between redshift 0.8 and 2.2. *Monthly Notices of the Royal Astronomical Society*, 477(2):1639–1663, June 2018. arXiv: 1801.03062.

[76] Daniel J. Eisenstein, Hee-jong Seo, and Martin White. On the Robustness of the Acoustic Scale in the Low-Redshift Clustering of Matter. *ApJ*, 664(2):660–674, August 2007. arXiv: astro-ph/0604361.

[77] Nikhil Padmanabhan, Martin White, and J. D. Cohn. Reconstructing baryon oscillations: A Lagrangian theory perspective. *Phys. Rev. D*, 79(6):063523, March 2009.

[78] Angela Burden, Will J. Percival, Marc Manera, Antonio J. Cuesta, Mariana Vargas Magana, and Shirley Ho. Efficient Reconstruction of Linear Baryon Acoustic Oscillations in Galaxy Surveys. *Monthly Notices of the Royal Astronomical Society*, 445(3):3152–3168, December 2014. arXiv: 1408.1348.

[79] A. Burden, W. J. Percival, and C. Howlett. Reconstruction in Fourier space. *Mon. Not. R. Astron. Soc.*, 453(1):456–468, October 2015.

[80] Nikhil Padmanabhan, Xiaoying Xu, Daniel J. Eisenstein, Richard Scalzo, Antonio J. Cuesta, Kushal T. Mehta, and Eyal Kazin. A 2 per cent distance to $z = 0.35$ by reconstructing baryon acoustic oscillations – I. Methods and application to the Sloan Digital Sky Survey: A 2 per cent distance to z = 0.35. *Monthly Notices of the Royal Astronomical Society*, 427(3):2132–2145, December 2012.

[81] Jack Birkin, Baojiu Li, Marius Cautun, and Yanlong Shi. Reconstructing the baryon acoustic oscillations using biased tracers. *Monthly Notices of the Royal Astronomical Society*, 483(4):5267–5280, March 2019. arXiv: 1809.08135.

[82] E. Sarpa, C. Schimd, E. Branchini, and S. Matarrese. BAO reconstruction: a swift numerical action method for massive spectroscopic surveys. *Monthly Notices of the Royal Astronomical Society*, 484(3):3818–3830, April 2019. arXiv: 1809.10738.

[83] Chirag Modi, Yu Feng, and Uros Seljak. Cosmological Reconstruction From Galaxy Light: Neural Network Based Light-Matter Connection. *J. Cosmol. Astropart. Phys.*, 2018(10):028–028, October 2018. arXiv: 1805.02247.

[84] Farnik Nikakhtar, Ravi K. Sheth, and Idit Zehavi. Laguerre reconstruction of the correlation function on Baryon Acoustic Oscillation scales. *arXiv:2101.08376 [astro-ph]*, January 2021. arXiv: 2101.08376.

[85] Roman Scoccimarro. Redshift-Space Distortions, Pairwise Velocities and Nonlinearities. *Phys. Rev. D*, 70(8):083007, October 2004. arXiv: astro-ph/0407214.

[86] Atsushi Taruya, Takahiro Nishimichi, and Shun Saito. Baryon acoustic oscillations in 2D: Modeling redshift-space power spectrum from perturbation theory. *Phys. Rev. D*, 82(6):063522, September 2010.

[87] Lile Wang, Beth Reid, and Martin White. An analytic model for redshift-space distortions. *Monthly Notices of the Royal Astronomical Society*, 437(1):588–599, January 2014.

[88] E. Jennings, C. M. Baugh, and S. Pascoli. Modelling redshift space distortions in hierarchical cosmologies: Redshift space distortions. *Monthly Notices of the Royal Astronomical Society*, pages no–no, October 2010.

[89] Ariel G. Sánchez, Eyal A. Kazin, Florian Beutler, Chia-Hsun Chuang, Antonio J. Cuesta, Daniel J. Eisenstein, Marc Manera, Francesco Montesano, Robert C. Nichol, Nikhil Padmanabhan, Will Percival, Francisco Prada, Ashley J. Ross, David J. Schlegel, Jeremy Tinker, Rita Tojeiro, David H. Weinberg, Xiaoying Xu, J. Brinkmann, Joel R. Brownstein, Donald P. Schneider, and Daniel Thomas. The clustering of galaxies in the SDSS-III Baryon Oscillation Spectroscopic Survey: cosmological constraints from the full shape of the clustering wedges. *Monthly Notices of the Royal Astronomical Society*, 433(2):1202–1222, August 2013.

[90] M. Crocce and R. Scoccimarro. Renormalized Cosmological Perturbation Theory. *Phys. Rev. D*, 73(6):063519, March 2006. arXiv: astro-ph/0509418.

[91] Ariel G. Sánchez, Román Scoccimarro, Martín Crocce, Jan Niklas Grieb, Salvador Salazar-Albornoz, Claudio Dalla Vecchia, Martha Lippich, Florian Beutler, Joel R. Brownstein, Chia-Hsun Chuang, Daniel J. Eisenstein, Francisco-Shu Kitaura, Matthew D. Olmstead, Will J. Percival, Francisco Prada, Sergio Rodríguez-Torres, Ashley J. Ross, Lado Samushia, Hee-Jong Seo, Jeremy Tinker, Rita Tojeiro, Mariana Vargas-Magaña, Yuting Wang, and Gong-Bo Zhao. The clustering of galaxies in the completed SDSS-III Baryon Oscillation Spectroscopic Survey: Cosmological implications of the configuration-space clustering wedges. *Mon. Not. R. Astron. Soc.*, 464(2):1640–1658, January 2017.

[92] Andrea Pezzotta, Martin Crocce, Alexander Eggemeier, Ariel G. Sánchez, and Román Scoccimarro. Testing one-loop galaxy bias: cosmological constraints from the power spectrum. *arXiv e-prints*, page arXiv:2102.08315, February 2021.

[93] Jan Niklas Grieb, Ariel G. Sánchez, Salvador Salazar-Albornoz, Román Scoccimarro, Martín Crocce, Claudio Dalla Vecchia, Francesco Montesano, Héctor Gil-Marín, Ashley J. Ross, Florian Beutler, Sergio Rodríguez-Torres, Chia-Hsun Chuang, Francisco Prada, Francisco-Shu Kitaura, Antonio J. Cuesta, Daniel J. Eisenstein, Will J. Percival, Mariana Vargas-Magana, Jeremy L. Tinker, Rita Tojeiro, Joel R. Brownstein, Claudia Maraston, Robert C. Nichol, Matthew D. Olmstead, Lado Samushia, Hee-Jong Seo, Alina Streblyanska, and Gong-bo Zhao. The clustering of galaxies in the completed SDSS-III Baryon Oscillation Spectroscopic Survey: Cosmological implications of the Fourier space wedges of the final sample. *Mon. Not. R. Astron. Soc.*, page stw3384, January 2017. arXiv: 1607.03143.

[94] D. Heath Jones, Will Saunders, Matthew Colless, Mike A. Read, Quentin A. Parker, Fred G. Watson, Lachlan A. Campbell, Daniel Burkey, Thomas Mauch, Malcolm

Hartley, Paul Cass, Dionne James, Ken Russell, Kristin Fiegert, John Dawe, John Huchra, Tom Jarrett, Ofer Lahav, John Lucey, Gary A. Mamon, Dominique Proust, Elaine M. Sadler, and Ken-ichi Wakamatsu. The 6dF Galaxy Survey: Samples, Observational Techniques and the First Data Release. *Monthly Notices of the Royal Astronomical Society*, 355(3):747–763, December 2004. arXiv: astro-ph/0403501.

[95] Paul Carter, Florian Beutler, Will J. Percival, Chris Blake, Jun Koda, and Ashley J. Ross. Low Redshift Baryon Acoustic Oscillation Measurement from the Reconstructed 6-degree Field Galaxy Survey. *Monthly Notices of the Royal Astronomical Society*, 481(2):2371–2383, December 2018. arXiv: 1803.01746.

[96] Florian Beutler, Chris Blake, Matthew Colless, D. Heath Jones, Lister Staveley-Smith, Gregory B. Poole, Lachlan Campbell, Quentin Parker, Will Saunders, and Fred Watson. The 6dF Galaxy Survey: z? 0 measurements of the growth rate and σ8: 6dFGS: z? 0 measurements of fσ8 and σ8. *Monthly Notices of the Royal Astronomical Society*, 423(4):3430–3444, July 2012.

[97] James E. Gunn, Walter A. Siegmund, Edward J. Mannery, Russell E. Owen, Charles L. Hull, R. French Leger, Larry N. Carey, Gillian R. Knapp, Donald G. York, William N. Boroski, Stephen M. Kent, Robert H. Lupton, Constance M. Rockosi, Michael L. Evans, Patrick Waddell, John E. Anderson, James Annis, John C. Barentine, Larry M. Bartoszek, Steven Bastian, Stephen B. Bracker, Howard J. Brewington, Charles I. Briegel, Jon Brinkmann, Yorke J. Brown, Michael A. Carr, Paul C. Czarapata, Craig C. Drennan, Thomas Dombeck, Glenn R. Federwitz, Bruce A. Gillespie, Carlos Gonzales, Sten U. Hansen, Michael Harvanek, Jeffrey Hayes, Wendell Jordan, Ellyne Kinney, Mark Klaene, S. J. Kleinman, Richard G. Kron, Jurek Kresinski, Glenn Lee, Siriluk Limmongkol, Carl W. Lindenmeyer, Daniel C. Long, Craig L. Loomis, Peregrine M. McGehee, Paul M. Mantsch, Eric H. Neilsen, Jr., Richard M. Neswold, Peter R. Newman, Atsuko Nitta, John Peoples, Jr., Jeffrey R. Pier, Peter S. Prieto, Angela Prosapio, Claudio Rivetta, Donald P. Schneider, Stephanie Snedden, and Shu-i Wang. The 2.5 m Telescope of the Sloan Digital Sky Survey. *AJ*, 131(4):2332–2359, April 2006.

[98] Ashley J. Ross, Lado Samushia, Cullan Howlett, Will J. Percival, Angela Burden, and Marc Manera. The Clustering of the SDSS DR7 Main Galaxy Sample I: A 4 per cent Distance Measure at z=0.15. *Monthly Notices of the Royal Astronomical Society*, 449(1):835–847, May 2015. arXiv: 1409.3242.

[99] Beth Reid, Shirley Ho, Nikhil Padmanabhan, Will J. Percival, Jeremy Tinker, Rita Tojeiro, Martin White, Daniel J. Eisenstein, Claudia Maraston, Ashley J.

Ross, Ariel G. Sanchez, David Schlegel, Erin Sheldon, Michael A. Strauss, Daniel Thomas, David Wake, Florian Beutler, Dmitry Bizyaev, Adam S. Bolton, Joel R. Brownstein, Chia-Hsun Chuang, Kyle Dawson, Paul Harding, Francisco-Shu Kitaura, Alexie Leauthaud, Karen Masters, Cameron K. McBride, Surhud More, Matthew D. Olmstead, Daniel Oravetz, Sebastian E. Nuza, Kaike Pan, John Parejko, Janine Pforr, Francisco Prada, Sergio Rodriguez-Torres, Salvador Salazar-Albornoz, Lado Samushia, Donald P. Schneider, Claudia G. Scoccola, Audrey Simmons, and Mariana Vargas-Magana. SDSS-III Baryon Oscillation Spectroscopic Survey Data Release 12: galaxy target selection and large scale structure catalogues. *arXiv:1509.06529 [astro-ph]*, October 2015. arXiv: 1509.06529.

[100] Beth A. Reid, Lado Samushia, Martin White, Will J. Percival, Marc Manera, Nikhil Padmanabhan, Ashley J. Ross, Ariel G. Sánchez, Stephen Bailey, Dmitry Bizyaev, Adam S. Bolton, Howard Brewington, J. Brinkmann, Joel R. Brownstein, Antonio J. Cuesta, Daniel J. Eisenstein, James E. Gunn, Klaus Honscheid, Elena Malanushenko, Viktor Malanushenko, Claudia Maraston, Cameron K. McBride, Demitri Muna, Robert C. Nichol, Daniel Oravetz, Kaike Pan, Roland de Putter, N. A. Roe, Nicholas P. Ross, David J. Schlegel, Donald P. Schneider, Hee-Jong Seo, Alaina Shelden, Erin S. Sheldon, Audrey Simmons, Ramin A. Skibba, Stephanie Snedden, Molly E. C. Swanson, Daniel Thomas, Jeremy Tinker, Rita Tojeiro, Licia Verde, David A. Wake, Benjamin A. Weaver, David H. Weinberg, Idit Zehavi, and Gong-Bo Zhao. The clustering of galaxies in the SDSS-III Baryon Oscillation Spectroscopic Survey: measurements of the growth of structure and expansion rate at z=0.57 from anisotropic clustering. *Monthly Notices of the Royal Astronomical Society*, 426(4):2719–2737, November 2012. arXiv: 1203.6641.

[101] Lauren Anderson, Eric Aubourg, Stephen Bailey, Florian Beutler, Vaishali Bhardwaj, Michael Blanton, Adam S. Bolton, J. Brinkmann, Joel R. Brownstein, Angela Burden, Chia-Hsun Chuang, Antonio J. Cuesta, Kyle S. Dawson, Daniel J. Eisenstein, Stephanie Escoffier, James E. Gunn, Hong Guo, Shirley Ho, Klaus Honscheid, Cullan Howlett, David Kirkby, Robert H. Lupton, Marc Manera, Claudia Maraston, Cameron K. McBride, Olga Mena, Francesco Montesano, Robert C. Nichol, Sebastian E. Nuza, Matthew D. Olmstead, Nikhil Padmanabhan, Nathalie Palanque-Delabrouille, John Parejko, Will J. Percival, Patrick Petitjean, Francisco Prada, Adrian M. Price-Whelan, Beth Reid, Natalie A. Roe, Ashley J. Ross, Nicholas P. Ross, Cristiano G. Sabiu, Shun Saito, Lado Samushia, Ariel G. Sanchez, David J. Schlegel, Donald P. Schneider, Claudia G. Scoccola, Hee-Jong Seo, Ramin A. Skibba, Michael A. Strauss, Molly E. C. Swanson, Daniel Thomas, Jeremy L. Tinker, Rita

Tojeiro, Mariana Vargas Magana, Licia Verde, David A. Wake, Benjamin A. Weaver, David H. Weinberg, Martin White, Xiaoying Xu, Christophe Yeche, Idit Zehavi, and Gong-Bo Zhao. The clustering of galaxies in the SDSS-III Baryon Oscillation Spectroscopic Survey: Baryon Acoustic Oscillations in the Data Release 10 and 11 galaxy samples. *Monthly Notices of the Royal Astronomical Society*, 441(1):24–62, June 2014. arXiv: 1312.4877.

[102] Ariel G. Sánchez, Francesco Montesano, Eyal A. Kazin, Eric Aubourg, Florian Beutler, Jon Brinkmann, Joel R. Brownstein, Antonio J. Cuesta, Kyle S. Dawson, Daniel J. Eisenstein, Shirley Ho, Klaus Honscheid, Marc Manera, Claudia Maraston, Cameron K. McBride, Will J. Percival, Ashley J. Ross, Lado Samushia, David J. Schlegel, Donald P. Schneider, Ramin Skibba, Daniel Thomas, Jeremy L. Tinker, Rita Tojeiro, David A. Wake, Benjamin A. Weaver, Martin White, and Idit Zehavi. The clustering of galaxies in the SDSS-III Baryon Oscillation Spectroscopic Survey: cosmological implications of the full shape of the clustering wedges in the data release 10 and 11 galaxy samples. *Monthly Notices of the Royal Astronomical Society*, 440(3):2692–2713, May 2014.

[103] Lado Samushia, Beth A. Reid, Martin White, Will J. Percival, Antonio J. Cuesta, Gong-Bo Zhao, Ashley J. Ross, Marc Manera, Éric Aubourg, Florian Beutler, Jon Brinkmann, Joel R. Brownstein, Kyle S. Dawson, Daniel J. Eisenstein, Shirley Ho, Klaus Honscheid, Claudia Maraston, Francesco Montesano, Robert C. Nichol, Natalie A. Roe, Nicholas P. Ross, Ariel G. Sánchez, David J. Schlegel, Donald P. Schneider, Alina Streblyanska, Daniel Thomas, Jeremy L. Tinker, David A. Wake, Benjamin A. Weaver, and Idit Zehavi. The Clustering of Galaxies in the SDSS-III Baryon Oscillation Spectroscopic Survey (BOSS): measuring growth rate and geometry with anisotropic clustering. *Monthly Notices of the Royal Astronomical Society*, 439(4):3504–3519, April 2014. arXiv: 1312.4899.

[104] Héctor Gil-Marín, Will J. Percival, Antonio J. Cuesta, Joel R. Brownstein, Chia-Hsun Chuang, Shirley Ho, Francisco-Shu Kitaura, Claudia Maraston, Francisco Prada, Sergio Rodríguez-Torres, Ashley J. Ross, David J. Schlegel, Donald P. Schneider, Daniel Thomas, Jeremy L. Tinker, Rita Tojeiro, Mariana Vargas Magaña, and Gong-Bo Zhao. The clustering of galaxies in the SDSS-III Baryon Oscillation Spectroscopic Survey: BAO measurement from the LOS-dependent power spectrum of DR12 BOSS galaxies. *Mon. Not. R. Astron. Soc.*, 460(4):4210–4219, August 2016. arXiv: 1509.06373.

[105] Cheng Zhao, Chia-Hsun Chuang, Julian Bautista, Arnaud de Mattia, Anand Raichoor, Ashley J. Ross, Jiamin Hou, Richard Neveux, Charling Tao, Etienne Burtin, Kyle S. Dawson, Sylvain de la Torre, Héctor Gil-Marín, Jean-Paul Kneib, Will J. Percival, Graziano Rossi, Amélie Tamone, Jeremy L. Tinker, Gong-Bo Zhao, Shadab Alam, and Eva-Maria Mueller. The Completed SDSS-IV extended Baryon Oscillation Spectroscopic Survey: one thousand multi-tracer mock catalogues with redshift evolution and systematics for galaxies and quasars of the final data release. *arXiv:2007.08997 [astro-ph]*, July 2020. arXiv: 2007.08997.

[106] Abhishek Prakash, Timothy C. Licquia, Jeffrey A. Newman, Ashley J. Ross, Adam D. Myers, Kyle S. Dawson, Jean-Paul Kneib, Will J. Percival, Julian E. Bautista, Johan Comparat, Jeremy L. Tinker, David J. Schlegel, Rita Tojeiro, Shirley Ho, Dustin Lang, Sandhya M. Rao, Cameron K. McBride, Guangtun Ben Zhu, Joel R. Brownstein, Stephen Bailey, Adam S. Bolton, Timothee Delubac, Vivek Mariappan, Michael R. Blanton, Beth Reid, Donald P. Schneider, Hee-Jong Seo, Aurelio Carnero Rosell, and Francisco Prada. The SDSS-IV extended Baryonic Oscillation Spectroscopic Survey: Luminous Red Galaxy Target Selection. *ApJS*, 224(2):34, June 2016. arXiv: 1508.04478.

[107] Siddharth Satpathy, Shadab Alam, Shirley Ho, Martin White, Neta A. Bahcall, Florian Beutler, Joel R. Brownstein, Chia-Hsun Chuang, Daniel J. Eisenstein, Jan Niklas Grieb, Francisco Kitaura, Matthew D. Olmstead, Will J. Percival, Salvador Salazar-Albornoz, Ariel G. Sánchez, Hee-Jong Seo, Daniel Thomas, Jeremy L. Tinker, and Rita Tojeiro. The clustering of galaxies in the completed SDSS-III Baryon Oscillation Spectroscopic Survey: On the measurement of growth rate using galaxy correlation functions. *Monthly Notices of the Royal Astronomical Society*, 469(2):1369–1382, August 2017. arXiv: 1607.03148.

[108] Héctor Gil-Marín, Will J. Percival, Antonio J. Cuesta, Joel R. Brownstein, Chia-Hsun Chuang, Shirley Ho, Francisco-Shu Kitaura, Claudia Maraston, Francisco Prada, Sergio Rodríguez-Torres, Ashley J. Ross, David J. Schlegel, Donald P. Schneider, Daniel Thomas, Jeremy L. Tinker, Rita Tojeiro, Mariana Vargas Magaña, and Gong-Bo Zhao. The clustering of galaxies in the SDSS-III Baryon Oscillation Spectroscopic Survey: BAO measurement from the LOS-dependent power spectrum of DR12 BOSS galaxies. *Mon. Not. R. Astron. Soc.*, 460(4):4210–4219, August 2016. arXiv: 1509.06373.

[109] Ashley J. Ross, Julian Bautista, Rita Tojeiro, Shadab Alam, Stephen Bailey, Etienne Burtin, Johan Comparat, Kyle S. Dawson, Arnaud de Mattia, Hélion du

Mas des Bourboux, Héctor Gil-Marín, Jiamin Hou, Hui Kong, Brad W. Lyke, Faizan G. Mohammad, John Moustakas, Eva-Maria Mueller, Adam D. Myers, Will J. Percival, Anand Raichoor, Mehdi Rezaie, Hee-Jong Seo, Alex Smith, Jeremy L. Tinker, Pauline Zarrouk, Cheng Zhao, Gong-Bo Zhao, Dmitry Bizyaev, Jonathan Brinkmann, Joel R. Brownstein, Aurelio Carnero Rosell, Solène Chabanier, Peter D. Choi, Chia-Hsun Chuang, Irene Cruz-Gonzalez, Axel de la Macorra, Sylvain de la Torre, Stephanie Escoffier, Sebastien Fromenteau, Alexandra Higley, Eric Jullo, Jean-Paul Kneib, Jacob N. McLane, Andrea Muñoz-Gutiérrez, Richard Neveux, Jeffrey A. Newman, Christian Nitschelm, Nathalie Palanque-Delabrouille, Romain Paviot, Anthony R. Pullen, Graziano Rossi, Vanina Ruhlmann-Kleider, Donald P. Schneider, Mariana Vargas Magaña, M. Vivek, and Yucheng Zhang. The Completed SDSS-IV extended Baryon Oscillation Spectroscopic Survey: Large-scale Structure Catalogs for Cosmological Analysis. *Monthly Notices of the Royal Astronomical Society*, 498(2):2354–2371, September 2020. arXiv: 2007.09000.

[110] Anand Raichoor, Arnaud de Mattia, Ashley J. Ross, Cheng Zhao, Shadab Alam, Santiago Avila, Julian Bautista, Jonathan Brinkmann, Joel R. Brownstein, Etienne Burtin, Michael J. Chapman, Chia-Hsun Chuang, Johan Comparat, Kyle S. Dawson, Arjun Dey, Hélion du Mas des Bourboux, Jack Elvin-Poole, Violeta Gonzalez-Perez, Claudio Gorgoni, Jean-Paul Kneib, Hui Kong, Dustin Lang, John Moustakas, Adam D. Myers, Eva-Maria Müller, Seshadri Nadathur, Jeffrey A. Newman, Will J. Percival, Mehdi Rezaie, Graziano Rossi, Vanina Ruhlmann-Kleider, David J. Schlegel, Donald P. Schneider, Hee-Jong Seo, Amélie Tamone, Jeremy L. Tinker, Rita Tojeiro, M. Vivek, Christophe Yèche, and Gong-Bo Zhao. The completed SDSS-IV extended Baryon Oscillation Spectroscopic Survey: Large-scale Structure Catalogues and Measurement of the isotropic BAO between redshift 0.6 and 1.1 for the Emission Line Galaxy Sample. *Monthly Notices of the Royal Astronomical Society*, 500(3):3254–3274, December 2020. arXiv: 2007.09007.

[111] Brad W. Lyke, Alexandra N. Higley, J. N. McLane, Danielle P. Schurhammer, Adam D. Myers, Ashley J. Ross, Kyle Dawson, Solène Chabanier, Paul Martini, Nicolás G. Busca, Hélion du Mas des Bourboux, Mara Salvato, Alina Streblyanska, Pauline Zarrouk, Etienne Burtin, Scott F. Anderson, Julian Bautista, Dmitry Bizyaev, W. N. Brandt, Jonathan Brinkmann, Joel R. Brownstein, Johan Comparat, Paul Green, Axel de la Macorra, Andrea Muñoz Gutiérrez, Jiamin Hou, Jeffrey A. Newman, Nathalie Palanque-Delabrouille, Isabelle Pâris, Will J. Percival, Patrick Petitjean, James Rich, Graziano Rossi, Donald P. Schneider, Alexander

Smith, M. Vivek, and Benjamin Alan Weaver. The Sloan Digital Sky Survey Quasar Catalog: Sixteenth Data Release. *ApJS*, 250(1):8, August 2020. arXiv: 2007.09001.

[112] I. Pâris, P. Petitjean, E. Aubourg, A. D. Myers, A. Streblyanska, B. W. Lyke, S. F. Anderson, E. Armengaud, J. Bautista, M. R. Blanton, M. Blomqvist, J. Brinkmann, J. R. Brownstein, W. N. Brandt, E. Burtin, K. Dawson, S. de la Torre, A. Georgakakis, H. Gil-Marin, P. J. Green, P. B. Hall, J.-P. Kneib, S. M. LaMassa, J.-M. Le Goff, C. MacLeod, V. Mariappan, I. D. McGreer, A. Merloni, P. Noterdaeme, N. Palanque Delabrouille, W. J. Percival, A. J. Ross, G. Rossi, D. P. Schneider, H.-J. Seo, R. Tojeiro, B. A. Weaver, A.-M. Weijmans, C. Yèche, P. Zarrouk, and G.-B. Zhao. The Sloan Digital Sky Survey Quasar Catalog: Fourteenth Data Release. *A&A*, 613:A51, May 2018. arXiv: 1712.05029.

[113] Héctor Gil-Marín, Julián E. Bautista, Romain Paviot, Mariana Vargas-Magaña, Sylvain de la Torre, Sebastien Fromenteau, Shadab Alam, Santiago Ávila, Etienne Burtin, Chia-Hsun Chuang, Kyle S. Dawson, Jiamin Hou, Arnaud de Mattia, Faizan G. Mohammad, Eva-Maria Müller, Seshadri Nadathur, Richard Neveux, Will J. Percival, Anand Raichoor, Mehdi Rezaie, Ashley J. Ross, Graziano Rossi, Vanina Ruhlmann-Kleider, Alex Smith, Amélie Tamone, Jeremy L. Tinker, Rita Tojeiro, Yuting Wang, Gong-Bo Zhao, Cheng Zhao, Jonathan Brinkmann, Joel R. Brownstein, Peter D. Choi, Stephanie Escoffier, Axel de la Macorra, Jeongin Moon, Jeffrey A. Newman, Donald P. Schneider, Hee-Jong Seo, and Mariappan Vivek. The Completed SDSS-IV extended Baryon Oscillation Spectroscopic Survey: measurement of the BAO and growth rate of structure of the luminous red galaxy sample from the anisotropic power spectrum between redshifts 0.6 and 1.0. *Monthly Notices of the Royal Astronomical Society*, 498(2):2492–2531, September 2020. arXiv: 2007.08994.

[114] Julian E. Bautista, Mariana Vargas-Magaña, Kyle S. Dawson, Will J. Percival, Jonathan Brinkmann, Joel Brownstein, Benjamin Camacho, Johan Comparat, Hector Gil-Marín, Eva-Maria Mueller, Jeffrey A. Newman, Abhishek Prakash, Ashley J. Ross, Donald P. Schneider, Hee-Jong Seo, Jeremy Tinker, Rita Tojeiro, Zhongxu Zhai, and Gong-Bo Zhao. The SDSS-IV Extended Baryon Oscillation Spectroscopic Survey: Baryon Acoustic Oscillations at Redshift of 0.72 with the DR14 Luminous Red Galaxy Sample. *ApJ*, 863(1):110, August 2018.

[115] M. Icaza-Lizaola, M. Vargas-Magaña, S. Fromenteau, S. Alam, B. Camacho, H. Gil-Marin, R. Paviot, Ashley Ross, Donald P. Schneider, Jeremy Tinker, Yuting Wang, Cheng Zhao, Abhishek Prakash, G. Rossi, Gong-Bo Zhao, Irene Cruz-Gonzalez, and

Axel de la Macorra. The clustering of the SDSS-IV extended Baryon Oscillation Spectroscopic Survey DR14 LRG sample: structure growth rate measurement from the anisotropic LRG correlation function in the redshift range 0.6 < z < 1.0. *Monthly Notices of the Royal Astronomical Society*, 492(3):4189–4215, March 2020. arXiv: 1909.07742.

[116] Arnaud de Mattia, Vanina Ruhlmann-Kleider, Anand Raichoor, Ashley J. Ross, Amélie Tamone, Cheng Zhao, Shadab Alam, Santiago Avila, Etienne Burtin, Julian Bautista, Florian Beutler, Jonathan Brinkmann, Joel R. Brownstein, Michael J. Chapman, Chia-Hsun Chuang, Johan Comparat, Hélion du Mas des Bourboux, Kyle S. Dawson, Axel de la Macorra, Héctor Gil-Marín, Violeta Gonzalez-Perez, Claudio Gorgoni, Jiamin Hou, Hui Kong, Sicheng Lin, Seshadri Nadathur, Jeffrey A. Newman, Eva-Maria Mueller, Will J. Percival, Mehdi Rezaie, Graziano Rossi, Donald P. Schneider, Prabhakar Tiwari, M. Vivek, Yuting Wang, and Gong-Bo Zhao. The Completed SDSS-IV extended Baryon Oscillation Spectroscopic Survey: measurement of the BAO and growth rate of structure of the emission line galaxy sample from the anisotropic power spectrum between redshift 0.6 and 1.1. *arXiv:2007.09008 [astro-ph]*, July 2020. arXiv: 2007.09008.

[117] Amélie Tamone, Anand Raichoor, Cheng Zhao, Arnaud de Mattia, Claudio Gorgoni, Etienne Burtin, Vanina Ruhlmann-Kleider, Ashley J. Ross, Shadab Alam, Will J. Percival, Santiago Avila, Michael J. Chapman, Chia-Hsun Chuang, Johan Comparat, Kyle S. Dawson, Sylvain de la Torre, Hélion du Mas des Bourboux, Stephanie Escoffier, Violeta Gonzalez-Perez, Jiamin Hou, Jean-Paul Kneib, Faizan G. Mohammad, Eva-Maria Mueller, Romain Paviot, Graziano Rossi, Donald P. Schneider, Yuting Wang, and Gong-Bo Zhao. The Completed SDSS-IV extended Baryon Oscillation Spectroscopic Survey: Growth rate of structure measurement from anisotropic clustering analysis in configuration space between redshift 0.6 and 1.1 for the Emission Line Galaxy sample. *Monthly Notices of the Royal Astronomical Society*, 499(4):5527–5546, November 2020. arXiv: 2007.09009.

[118] Scott M. Croom, B. J. Boyle, T. Shanks, R. J. Smith, L. Miller, P. J. Outram, N. S. Loaring, F. Hoyle, and J. da Ângela. The 2dF QSO Redshift Survey - XIV. Structure and evolution from the two-point correlation function. *Monthly Notices of the Royal Astronomical Society*, 356(2):415–438, January 2005.

[119] Jiamin Hou, Ariel G. Sánchez, Ashley J. Ross, Alex Smith, Richard Neveux, Julian Bautista, Etienne Burtin, Cheng Zhao, Román Scoccimarro, Kyle S. Dawson,

Arnaud de Mattia, Axel de la Macorra, Hélion du Mas des Bourboux, Daniel J. Eisenstein, Héctor Gil-Marín, Brad W. Lyke, Faizan G. Mohammad, Eva-Maria Mueller, Will J. Percival, Mariana Vargas Magaña, Graziano Rossi, Pauline Zarrouk, Gong-Bo Zhao, Jonathan Brinkmann, Joel R. Brownstein, Chia-Hsun Chuang, Adam D. Myers, Jeffrey A. Newman, Donald P. Schneider, and M. Vivek. The Completed SDSS-IV extended Baryon Oscillation Spectroscopic Survey: BAO and RSD measurements from anisotropic clustering analysis of the Quasar Sample in configuration space between redshift 0.8 and 2.2. *arXiv:2007.08998 [astro-ph]*, July 2020. arXiv: 2007.08998.

[120] Metin Ata, Falk Baumgarten, Julian Bautista, Florian Beutler, Dmitry Bizyaev, Michael R. Blanton, Jonathan A. Blazek, Adam S. Bolton, Jonathan Brinkmann, Joel R. Brownstein, Etienne Burtin, Chia-Hsun Chuang, Johan Comparat, Kyle S. Dawson, Axel de la Macorra, Wei Du, Helion du Mas des Bourboux, Daniel J. Eisenstein, Hector Gil-Marin, Katie Grabowski, Julien Guy, Nick Hand, Shirley Ho, Timothy A. Hutchinson, Mikhail M. Ivanov, Francisco-Shu Kitaura, Jean-Paul Kneib, Pierre Laurent, Jean-Marc Le Goff, Joseph E. McEwen, Eva-Maria Mueller, Adam D. Myers, Jeffrey A. Newman, Nathalie Palanque-Delabrouille, Kaike Pan, Isabelle Paris, Marcos Pellejero-Ibanez, Will J. Percival, Patrick Petitjean, Francisco Prada, Abhishek Prakash, Sergio A. Rodriguez-Torres, Ashley J. Ross, Graziano Rossi, Rossana Ruggeri, Ariel G. Sanchez, Siddharth Satpathy, David J. Schlegel, Donald P. Schneider, Hee-Jong Seo, Anze Slosar, Alina Streblyanska, Jeremy L. Tinker, Rita Tojeiro, Mariana Vargas Magana, M. Vivek, Yuting Wang, Christophe Yeche, Liang Yu, Pauline Zarrouk, Cheng Zhao, Gong-Bo Zhao, and Fangzhou Zhu. The clustering of the SDSS-IV extended Baryon Oscillation Spectroscopic Survey DR14 quasar sample: First measurement of Baryon Acoustic Oscillations between redshift 0.8 and 2.2. *Monthly Notices of the Royal Astronomical Society*, 473(4):4773–4794, February 2018. arXiv: 1705.06373.

[121] Michael J. Drinkwater, Russell J. Jurek, Chris Blake, David Woods, Kevin A. Pimbblet, Karl Glazebrook, Rob Sharp, Michael B. Pracy, Sarah Brough, Matthew Colless, Warrick J. Couch, Scott M. Croom, Tamara M. Davis, Duncan Forbes, Karl Forster, David G. Gilbank, Michael Gladders, Ben Jelliffe, Nick Jones, I.-hui Li, Barry Madore, D. Christopher Martin, Gregory B. Poole, Todd Small, Emily Wisnioski, Ted Wyder, and H. K. C. Yee. The WiggleZ Dark Energy Survey: Survey Design and First Data Release. *Monthly Notices of the Royal Astronomical Society*, 401(3):1429–1452, January 2010. arXiv: 0911.4246.

[122] Eyal A. Kazin, Jun Koda, Chris Blake, Nikhil Padmanabhan, Sarah Brough, Matthew Colless, Carlos Contreras, Warrick Couch, Scott Croom, Darren J. Croton, Tamara M. Davis, Michael J. Drinkwater, Karl Forster, David Gilbank, Mike Gladders, Karl Glazebrook, Ben Jelliffe, Russell J. Jurek, I.-hui Li, Barry Madore, D. Christopher Martin, Kevin Pimbblet, Gregory B. Poole, Michael Pracy, Rob Sharp, Emily Wisnioski, David Woods, Ted K. Wyder, and H. K. C. Yee. The WiggleZ Dark Energy Survey: Improved Distance Measurements to z = 1 with Reconstruction of the Baryonic Acoustic Feature. *Monthly Notices of the Royal Astronomical Society*, 441(4):3524–3542, July 2014. arXiv: 1401.0358.

[123] Hume A. Feldman, Nick Kaiser, and John A. Peacock. Power Spectrum Analysis of Three-Dimensional Redshift Surveys. *ApJ*, 426:23, May 1994. arXiv: astro-ph/9304022.

[124] John Joseph M. Carrasco, Mark P. Hertzberg, and Leonardo Senatore. The effective field theory of cosmological large scale structures. *J. High Energ. Phys.*, 2012(9):82, September 2012.

[125] Daniel Baumann, Alberto Nicolis, Leonardo Senatore, and Matias Zaldarriaga. Cosmological non-linearities as an effective fluid. *J. Cosmol. Astropart. Phys.*, 2012(07):051–051, July 2012.

[126] Mikhail M. Ivanov, Evan McDonough, J. Colin Hill, Marko Simonović, Michael W. Toomey, Stephon Alexander, and Matias Zaldarriaga. Constraining Early Dark Energy with Large-Scale Structure. *Phys. Rev. D*, 102(10):103502, November 2020. arXiv: 2006.11235.

[127] Guido D'Amico, Jérôme Gleyzes, Nickolas Kokron, Dida Markovic, Leonardo Senatore, Pierre Zhang, Florian Beutler, and Héctor Gil-Marín. The Cosmological Analysis of the SDSS/BOSS data from the Effective Field Theory of Large-Scale Structure. *J. Cosmol. Astropart. Phys.*, 2020(05):005–005, May 2020. arXiv: 1909.05271.

[128] Shi-Fan Chen, Zvonimir Vlah, Emanuele Castorina, and Martin White. Redshift-space distortions in Lagrangian perturbation theory. *J. Cosmol. Astropart. Phys.*, 2021(03):100, March 2021.

[129] Nickolas Kokron, Joseph DeRose, Shi-Fan Chen, Martin White, and Risa H. Wechsler. The cosmology dependence of galaxy clustering and lensing from a hybrid N-body-perturbation theory model. *arXiv:2101.11014 [astro-ph]*, January 2021. arXiv: 2101.11014.

[130] Zhongxu Zhai, Jeremy L. Tinker, Matthew R. Becker, Joseph DeRose, Yao-Yuan Mao, Thomas McClintock, Sean McLaughlin, Eduardo Rozo, and Risa H. Wechsler. The Aemulus Project. III. Emulation of the Galaxy Correlation Function. *ApJ*, 874(1):95, March 2019.

[131] Beth A. Reid, Hee-Jong Seo, Alexie Leauthaud, Jeremy L. Tinker, and Martin White. A 2.5% measurement of the growth rate from small-scale redshift space clustering of SDSS-III CMASS galaxies. *Monthly Notices of the Royal Astronomical Society*, 444(1):476–502, October 2014. arXiv: 1404.3742.

[132] Johannes U. Lange, Andrew P. Hearin, Alexie Leauthaud, Frank C. van den Bosch, Hong Guo, and Joseph DeRose. Five-percent measurements of the growth rate from simulation-based modelling of redshift-space clustering in BOSS LOWZ. *arXiv:2101.12261 [astro-ph]*, January 2021. arXiv: 2101.12261.

[133] D. Spergel, N. Gehrels, J. Breckinridge, M. Donahue, A. Dressler, B. S. Gaudi, T. Greene, O. Guyon, C. Hirata, J. Kalirai, N. J. Kasdin, W. Moos, S. Perlmutter, M. Postman, B. Rauscher, J. Rhodes, Y. Wang, D. Weinberg, J. Centrella, W. Traub, C. Baltay, J. Colbert, D. Bennett, A. Kiessling, B. Macintosh, J. Merten, M. Mortonson, M. Penny, E. Rozo, D. Savransky, K. Stapelfeldt, Y. Zu, C. Baker, E. Cheng, D. Content, J. Dooley, M. Foote, R. Goullioud, K. Grady, C. Jackson, J. Kruk, M. Levine, M. Melton, C. Peddie, J. Ruffa, and S. Shaklan. Wide-field infrared survey telescope-astrophysics focused telescope assets wfirst-afta final report, 2013.

[134] R. Laureijs, J. Amiaux, S. Arduini, J. L. Augueres, J. Brinchmann, R. Cole, M. Cropper, C. Dabin, L. Duvet, A. Ealet, B. Garilli, P. Gondoin, L. Guzzo, J. Hoar, H. Hoekstra, R. Holmes, T. Kitching, T. Maciaszek, Y. Mellier, F. Pasian, W. Percival, J. Rhodes, G. Saavedra Criado, M. Sauvage, R. Scaramella, L. Valenziano, S. Warren, R. Bender, F. Castander, A. Cimatti, O. Le Fèvre, H. Kurki-Suonio, M. Levi, P. Lilje, G. Meylan, R. Nichol, K. Pedersen, V. Popa, R. Rebolo Lopez, H. W. Rix, H. Rottgering, W. Zeilinger, F. Grupp, P. Hudelot, R. Massey, M. Meneghetti, L. Miller, S. Paltani, S. Paulin-Henriksson, S. Pires, C. Saxton, T. Schrabback, G. Seidel, J. Walsh, N. Aghanim, L. Amendola, J. Bartlett, C. Baccigalupi, J. P. Beaulieu, K. Benabed, J. G. Cuby, D. Elbaz, P. Fosalba, G. Gavazzi, A. Helmi, I. Hook, M. Irwin, J. P. Kneib, M. Kunz, F. Mannucci, L. Moscardini, C. Tao, R. Teyssier, J. Weller, G. Zamorani, M. R. Zapatero Osorio, O. Boulade, J. J. Foumond, A. Di Giorgio, P. Guttridge, A. James, M. Kemp, J. Martignac, A. Spencer, D. Walton, T. Blümchen, C. Bonoli, F. Bortoletto, C. Cerna, L. Corcione, C. Fabron, K. Jahnke,

S. Ligori, F. Madrid, L. Martin, G. Morgante, T. Pamplona, E. Prieto, M. Riva, R. Toledo, M. Trifoglio, F. Zerbi, F. Abdalla, M. Douspis, C. Grenet, S. Borgani, R. Bouwens, F. Courbin, J. M. Delouis, P. Dubath, A. Fontana, M. Frailis, A. Grazian, J. Koppenhöfer, O. Mansutti, M. Melchior, M. Mignoli, J. Mohr, C. Neissner, K. Noddle, M. Poncet, M. Scodeggio, S. Serrano, N. Shane, J. L. Starck, C. Surace, A. Taylor, G. Verdoes-Kleijn, C. Vuerli, O. R. Williams, A. Zacchei, B. Altieri, I. Escudero Sanz, R. Kohley, T. Oosterbroek, P. Astier, D. Bacon, S. Bardelli, C. Baugh, F. Bellagamba, C. Benoist, D. Bianchi, A. Biviano, E. Branchini, C. Carbone, V. Cardone, D. Clements, S. Colombi, C. Conselice, G. Cresci, N. Deacon, J. Dunlop, C. Fedeli, F. Fontanot, P. Franzetti, C. Giocoli, J. Garcia-Bellido, J. Gow, A. Heavens, P. Hewett, C. Heymans, A. Holland, Z. Huang, O. Ilbert, B. Joachimi, E. Jennins, E. Kerins, A. Kiessling, D. Kirk, R. Kotak, O. Krause, O. Lahav, F. van Leeuwen, J. Lesgourgues, M. Lombardi, M. Magliocchetti, K. Maguire, E. Majerotto, R. Maoli, F. Marulli, S. Maurogordato, H. McCracken, R. McLure, A. Melchiorri, A. Merson, M. Moresco, M. Nonino, P. Norberg, J. Peacock, R. Pello, M. Penny, V. Pettorino, C. Di Porto, L. Pozzetti, C. Quercellini, M. Radovich, A. Rassat, N. Roche, S. Ronayette, E. Rossetti, B. Sartoris, P. Schneider, E. Semboloni, S. Serjeant, F. Simpson, C. Skordis, G. Smadja, S. Smartt, P. Spano, S. Spiro, M. Sullivan, A. Tilquin, R. Trotta, L. Verde, Y. Wang, G. Williger, G. Zhao, J. Zoubian, and E. Zucca. Euclid definition study report, 2011.

[135] Henry S. Grasshorn Gebhardt, Donghui Jeong, Humna Awan, Joanna S. Bridge, Robin Ciardullo, Daniel Farrow, Karl Gebhardt, Gary J. Hill, Eiichiro Komatsu, Mallory Molina, and et al. Unbiased cosmological parameter estimation from emission-line surveys with interlopers. *The Astrophysical Journal*, 876(1):32, Apr 2019.

[136] Yan Gong, Haitao Miao, Pengjie Zhang, and Xuelei Chen. Self-calibrating interloper bias in spectroscopic galaxy-clustering surveys. *The Astrophysical Journal*, 919(1):12, sep 2021.

[137] Anthony R. Pullen, Christopher M. Hirata, Olivier Doré, and Alvise Raccanelli. Interloper bias in future large-scale structure surveys. *Publ. Astron. Soc. Jpn*, 68(1):12, 02 2016.

[138] Elena Massara, Shirley Ho, Christopher M. Hirata, Joseph DeRose, Risa H. Wechsler, and Xiao Fang. Line confusion in spectroscopic surveys and its possible effects: Shifts in baryon acoustic oscillations position, 2020.

[139] Antony Lewis, Anthony Challinor, and Anthony Lasenby. Efficient computation of CMB anisotropies in closed FRW models. *ApJ*, 538(2):473–476, 08 2000.

[140] Zhongxu Zhai, Andrew Benson, Yun Wang, Gustavo Yepes, and Chia-Hsun Chuang. Prediction of Hα and [OIII] emission line galaxy number counts for future galaxy redshift surveys. *Mon. Not. Roy. Astron. Soc.*, 490(3):3667–3678, 2019.

[141] Nick Hand, Yu Feng, Florian Beutler, Yin Li, Chirag Modi, Uroš Seljak, and Zachary Slepian. nbodykit: An open-source, massively parallel toolkit for large-scale structure. *The Astronomical Journal*, 156(4):160, sep 2018.

[142] Anthony R. Pullen, Christopher M. Hirata, Olivier Doré, and Alvise Raccanelli. Interloper bias in future large-scale structure surveys. *Publications of the Astronomical Society of Japan*, 68(1):12, Dec 2015.

[143] R. E. Smith, J. A. Peacock, A. Jenkins, S. D. M. White, C. S. Frenk, F. R. Pearce, P. A. Thomas, G. Efstathiou, and H. M. P. Couchman. Stable clustering, the halo model and non-linear cosmological power spectra. *Monthly Notices of the Royal Astronomical Society*, 341(4):1311–1332, 06 2003.

[144] Ryuichi Takahashi, Masanori Sato, Takahiro Nishimichi, Atsushi Taruya, and Masamune Oguri. REVISING THE HALOFIT MODEL FOR THE NONLINEAR MATTER POWER SPECTRUM. *ApJ*, 761(2):152, 12 2012.

[145] Nikhil Padmanabhan and Martin White. Constraining anisotropic baryon oscillations. *Phys. Rev. D*, 77:123540, Jun 2008.

[146] Xiaoying Xu, Antonio J. Cuesta, Nikhil Padmanabhan, Daniel J. Eisenstein, and Cameron K. McBride. Measuring DA and h at z=0.35 from the SDSS DR7 LRGs using baryon acoustic oscillations. *Monthly Notices of the Royal Astronomical Society*, 431(3):2834–2860, mar 2013.

[147] Charles Alcock and Bohdan Paczyński. An evolution free test for non-zero cosmological constant. *Nature*, 281(5730):358–359, 10 2079.

[148] Zvonimir Vlah, Uroš Seljak, Man Yat Chu, and Yu Feng. Perturbation theory, effective field theory, and oscillations in the power spectrum. 2016(3):057–057.

[149] J. C. Jackson. A critique of rees's theory of primordial gravitational radiation. *Monthly Notices of the Royal Astronomical Society*, 156(1):1P–5P, 02 1972.

[150] Chris Blake, Sarah Brough, Matthew Colless, Carlos Contreras, Warrick Couch, Scott Croom, Tamara Davis, Michael J. Drinkwater, Karl Forster, David Gilbank, Mike Gladders, Karl Glazebrook, Ben Jelliffe, Russell J. Jurek, I-hui Li, Barry Madore,

D. Christopher Martin, Kevin Pimbblet, Gregory B. Poole, Michael Pracy, Rob Sharp, Emily Wisnioski, David Woods, Ted K. Wyder, and H. K. C. Yee. The WiggleZ dark energy survey: the growth rate of cosmic structure since redshift z=0.9. *Monthly Notices of the Royal Astronomical Society*, 415(3):2876–2891, 08 2011.

[151] Daniel Foreman-Mackey, David W. Hogg, Dustin Lang, and Jonathan Goodman. emcee: The MCMC hammer. *Publications of the Astronomical Society of the Pacific*, 125(925):306–312, 03 2013.

[152] Will J Percival, Oliver Friedrich, Elena Sellentin, and Alan Heavens. Matching Bayesian and frequentist coverage probabilities when using an approximate data covariance matrix. *Monthly Notices of the Royal Astronomical Society*, 510(3):3207–3221, 12 2021.

[153] Mariana Vargas Magaña, Shirley Ho, Xiaoying Xu, Ariel G. Sánchez, Ross O'Connell, Daniel J. Eisenstein, Antonio J. Cuesta, Will J. Percival, Ashley J. Ross, Eric Aubourg, Stéphanie Escoffier David Kirkby, Marc Manera, Donald P. Schneider, Jeremy L. Tinker, and Benjamin A. Weaver. SDSS-III baryon oscillation spectroscopic survey: Analysis of potential systematics in fitting of baryon acoustic feature, 12 2013.

[154] Joseph DeRose, Matthew R. Becker, and Risa H. Wechsler. Modeling Redshift-Space Clustering with Abundance Matching. *arXiv e-prints*, page arXiv:2105.12104, May 2021.

[155] Yosuke Kobayashi, Takahiro Nishimichi, Masahiro Takada, Ryuichi Takahashi, and Ken Osato. Accurate emulator for the redshift-space power spectrum of dark matter halos and its application to galaxy power spectrum. *Phys. Rev. D*, 102(6):063504, September 2020. arXiv: 2005.06122.

[156] Elena Massara, Shirley Ho, Christopher M. Hirata, Joseph DeRose, Risa H. Wechsler, and Xiao Fang. Line confusion in spectroscopic surveys and its possible effects: Shifts in Baryon Acoustic Oscillations position. *arXiv:2010.00047 [astro-ph]*, September 2020. arXiv: 2010.00047.

[157] Andreu Font-Ribera and Jordi Miralda-Escud. The effect of high column density systems on the measurement of the Lyman-α forest correlation function. *JCAP*, 2012(7):028, 06 2012.

[158] Lado Samushia, Will J. Percival, Luigi Guzzo, Yun Wang, Andrea Cimatti, Carlton Baugh, James E. Geach, Cedric Lacey, Elisabetta Majerotto, Pia Mukherjee, and

Alvaro Orsi. Effects of cosmological model assumptions on galaxy redshift survey measurements. *Monthly Notices of the Royal Astronomical Society*, pages no–no, October 2010. arXiv: 1006.0609.

APPENDICES

Appendix A

Marginalizing over dilation parameters

Our baseline, throughout this paper, when analyzing the $f\sigma_8$ constraint with RSD, is to fix the dilation parameters. In this section, we show that our conclusions remain unchanged if we instead marginalize over the dilation parameters. Considering the free parameters in the Fisher matrix in Eq. 2.1 to be $\{\alpha_\perp, \alpha_\parallel, \ln f\sigma_8, \ln b\sigma_8\}$, we can build a 4 by 4 Fisher matrix using the following derivatives ([158]):

$$\begin{aligned}
\frac{\partial \ln P}{\partial \alpha_\perp} &= -2 + 4f\sigma_8(z)\mu^2(1-\mu^2)/(b\sigma_8(z) + f\sigma_8(z)\mu^2) - (1-\mu^2)\frac{\partial \ln P}{\partial \ln(k)}\,, \\
\frac{\partial \ln P}{\partial \alpha_\parallel} &= -1 - 4f\sigma_8(z)\mu^2(1-\mu^2)/(b\sigma_8(z) + f\sigma_8(z)\mu^2) - \mu^2\frac{\partial \ln P}{\partial \ln(k)}\,, \\
\frac{\partial \ln P}{\partial \ln f\sigma_8} &= \frac{2\mu^2 f\sigma_8(z)}{b\sigma_8(z) + f\sigma_8(z)\mu^2}\,, \\
\frac{\partial \ln P}{\partial \ln b\sigma_8} &= \frac{2b\sigma_8(z)}{b\sigma_8(z) + f\sigma_8(z)\mu^2}\,.
\end{aligned} \tag{A.1}$$

Although we are fitting to the αs, and relying on the BAO signal to constrain these, we follow the standard approach and assume that reconstruction cannot be used, because we also wish to model the form of the clustering signal - something that is hard to do post-reconstruction. Thus, our errors on α will be larger than those in Table 2.2 and 2.3, where a standard reconstruction technique was applied to both Fisher prediction and the data. Assuming $k_{\rm max}^{\rm fid} = 0.1/D(z)\,h\,{\rm Mpc}^{-1}$, we predict errors for these free parameters. The fractional error for $f\sigma_8^{\rm mg.\,\alpha s}$ is reported in Table A.1 and Table A.2. Figure A.1 is analogous to Figure 2.4, except that it is calculated for $f\sigma_8^{\rm mg.\,\alpha s}$. As can be seen from this plot, the scatter around the Fisher to data ratio is larger compared to Figure 2.4, and therefore, so is the scatter around $k_{\rm max}^{\rm match}$.

We show contour plots for the data and Fisher matrices (with $k_{\rm max} = 0.09\,h\,{\rm Mpc}^{-1}$) for few representative samples, spanning a range in redshift and omitting some samples for clarity. We show BOSS DR12 Near (Figure A.2), eBOSS+CMASS LRG DR16 (Figure A.3), eBOSS Quasar DR16 (Figure A.4), WiggleZ Mid (right panel Figure A.5), and, eBOSS Quasar DR14 (Figure A.6), and eBOSS ELG (Figure A.7). The centres of these contours are set to the fiducial value for each parameter. If $b\sigma_8$ was not provided in the data covariance matrix, we omitted the $b\sigma_8$ contour for that survey.

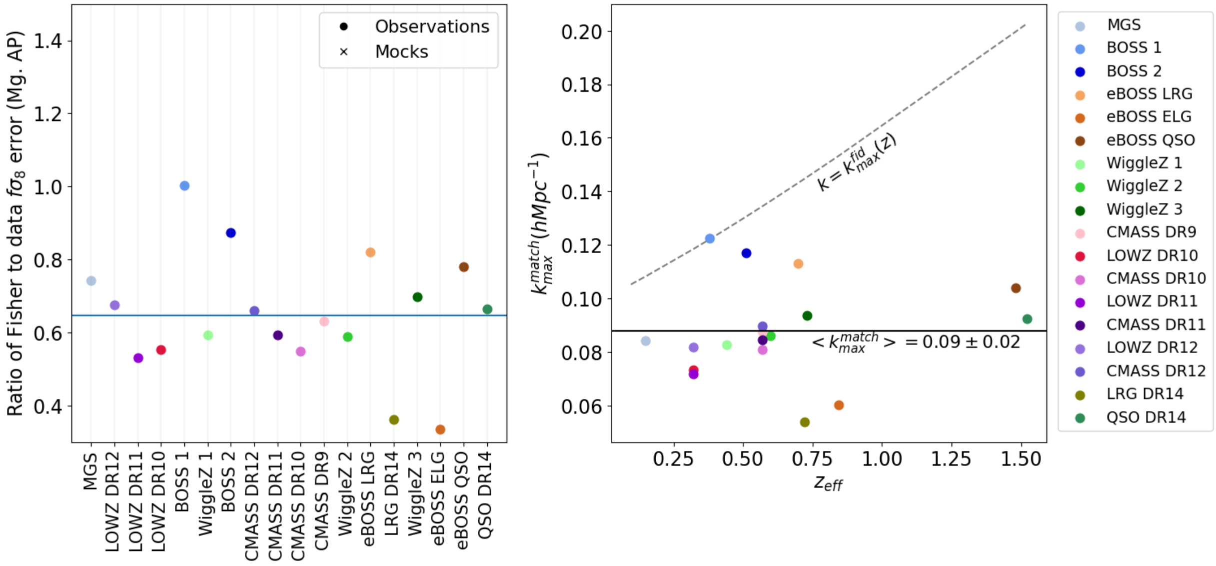

Figure A.1: *Left*: The difference between Fisher-based predicted $f\sigma_8$ error and observational $f\sigma_8^{\mathrm{mg.}\,\alpha s}$ error is plotted for each survey. *Right*: We have adjusted the $k_{\max}$ in order to make Fisher predictions match with the experiments. The dashed line represents the fiducial value of $k_{\max} = 0.1/D(z)\,h\,\mathrm{Mpc}^{-1}$. (Near, Mid, and Far redshift slices are shortened as 1, 2 and 3, respectively.)

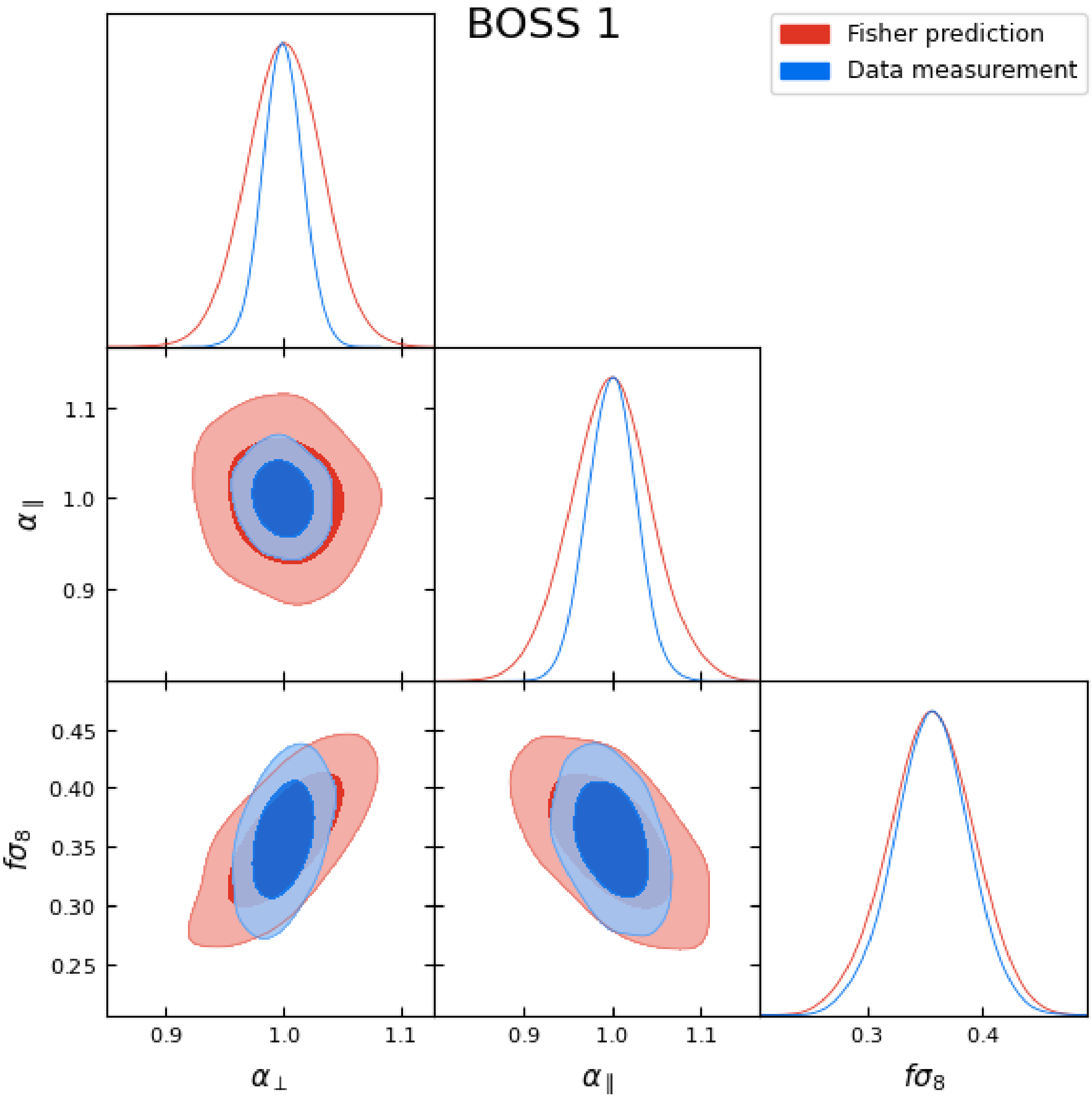

Figure A.2: Constraints on $\alpha_\perp$, $\alpha_\parallel$, and $f\sigma_8$. Red contours show 68 and 95 percent confidence regions for the Fisher analysis with $k_{\max} = 0.09\,h\,\mathrm{Mpc}^{-1}$ (this work). The full-shape consensus analysis of the BOSS Near DR12 sample is shown in blue (Alam et al. [64]).

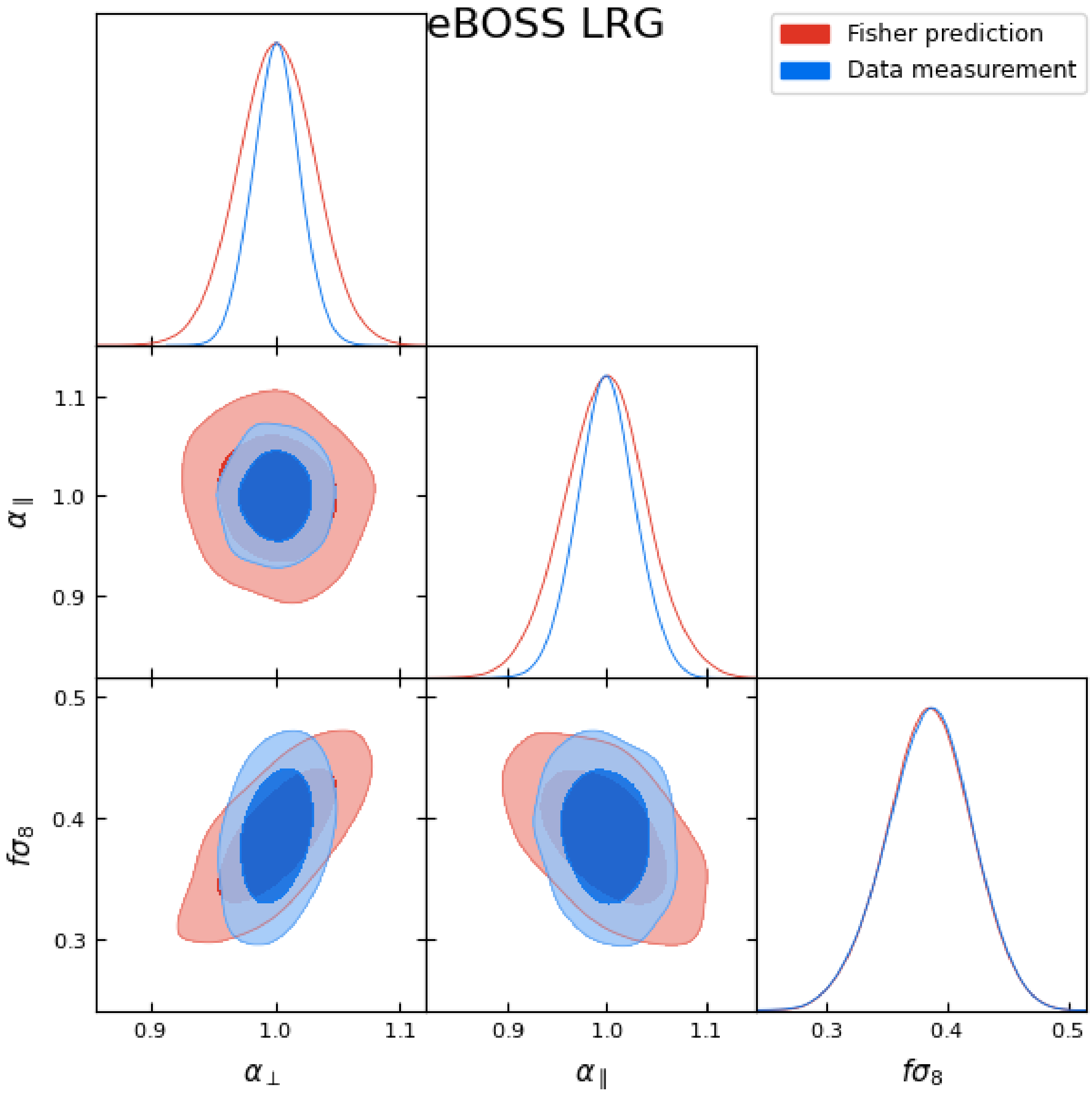

Figure A.3: Constraints on $\alpha_\perp$, $\alpha_\parallel$, and $f\sigma_8$. Red contours show 68 and 95 percent confidence regions for the Fisher analysis with $k_{\max} = 0.09\,h\,\mathrm{Mpc}^{-1}$ (this work). The full-shape RSD analysis for eBOSS LRG DR16 in configuration space analysis is shown in blue (Bautistia et al. [65]).

Table A.1: The fractional error of $f\sigma_8^{\mathrm{mg.\alpha s}}$ in percent and the k_{max} at which observed (O.) and Fisher (F.) errors match. In contrast to Table 2.2, the Fisher prediction errors are calculated after marginalizing over the dilation parameters (Mg.).

	6dFGS	MGS	BOSS		eBOSS			WiggleZ		
			Near	Mid	LRG$^+$	ELG	QSO	Near	Mid	Far
$f\sigma_8$(O.Mg.)	-	40.5	7.8	7.6	7.9	23.6	9.3	19.4	16.1	16.4
$f\sigma_8$(F.Mg.)	-	30.1	7.8	6.7	6.5	7.9	7.3	11.5	9.5	11.4
k_{max}(Match)	-	0.084	0.122	0.117	0.113	0.060	0.104	0.083	0.086	0.094

Table A.2: Same as Table A.1 but including intermediate data releases.

	BOSS	BOSS DR10		BOSS DR11		BOSS DR12		eBOSS DR14		eBOSS DR16	
	DR9	LZ	CM	LZ	CM	LZ	CM	LRG$^+$	QSO	LRG$^+$	QSO
$f\sigma_8$(O.Mg.)	14.6	23.3	12.8	20.8	9.9	15.7	8.6	29.2	16.4	7.9	9.3
$f\sigma_8$(F.Mg.)	9.2	12.9	7.0	11.1	5.9	10.6	5.7	10.5	10.9	6.5	7.3
k_{max}(Match)	0.087	0.073	0.081	0.072	0.085	0.082	0.090	0.054	0.093	0.113	0.104

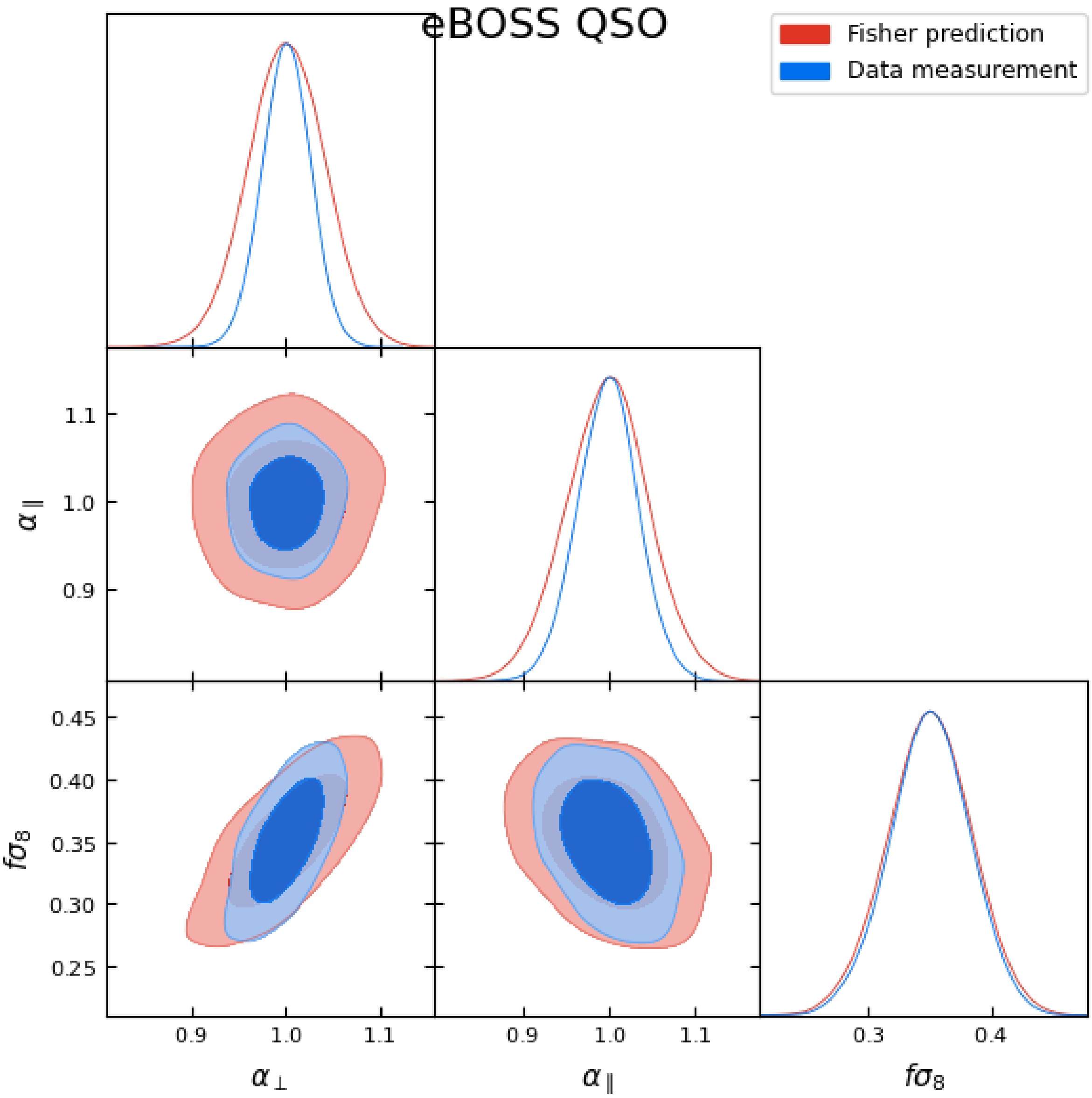

Figure A.4: Constraints on $\alpha_\perp$, $\alpha_\parallel$, and $f\sigma_8$. Red contours show 68 and 95 percent confidence regions for the Fisher analysis with $k_{\max} = 0.09\,h\,\mathrm{Mpc}^{-1}$ (this work). The full-shape RSD analysis of the eBOSS Quasar DR16 sample is shown in blue (Neveux et al. [66]).

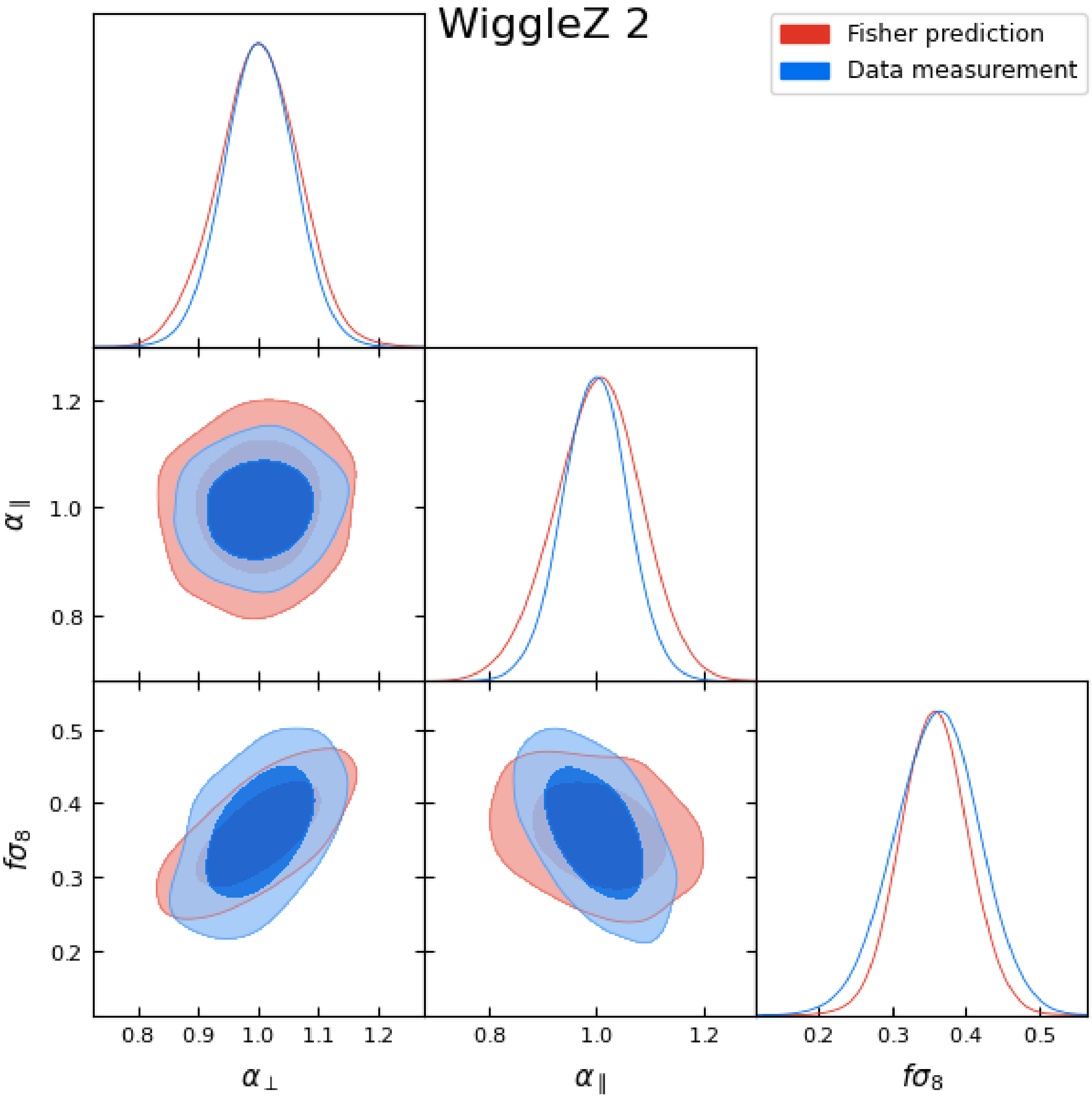

Figure A.5: Constraints on $\alpha_\perp$, $\alpha_\parallel$, and $f\sigma_8$. Red contours show 68 and 95 percent confidence regions for the Fisher analysis with $k_{\rm max} = 0.09\,h\,{\rm Mpc}^{-1}$ (this work). The joint fit to expansion and growth for WiggleZ Mid redshift slice is shown in blue. The covariance matrix was originally in $\{A, F, f\sigma_8\}$ but then we converted to $\alpha_\parallel$, $\alpha_\perp$ and $f\sigma_8$ (Blake et al. [67]).

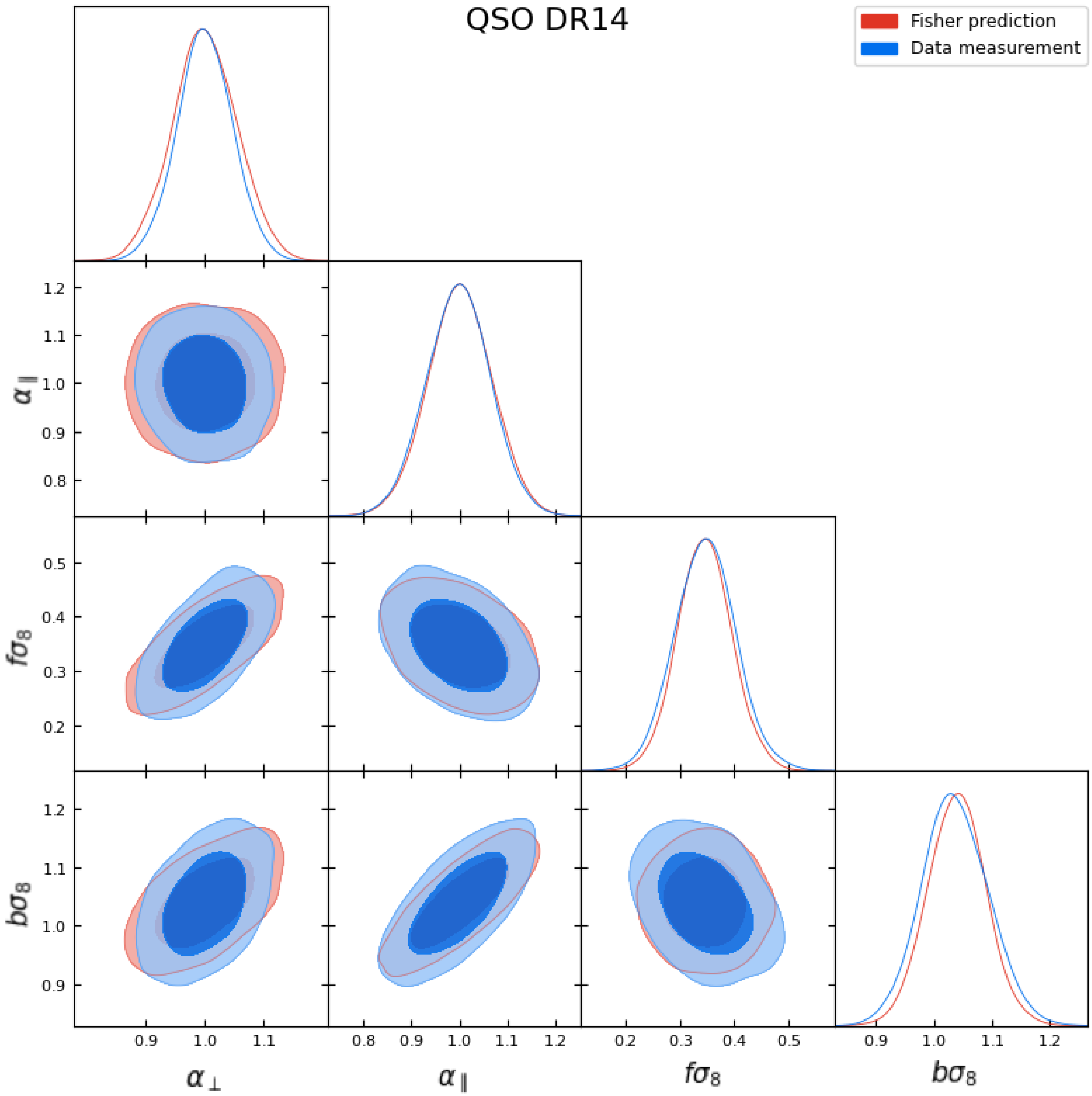

Figure A.6: Constraints on $\alpha_\perp$, $\alpha_\parallel$, $f\sigma_8$, and $b\sigma_8$. Red contours show 68 and 95 percent confidence regions for the Fisher analysis with $k_{\mathrm{max}} = 0.09\,h\,\mathrm{Mpc}^{-1}$ (this work), and the blue contours show confidence regions for eBOSS Quasar DR14 sample analysis from 5-parameter RSD modeling by Zarrouk et al. [75].

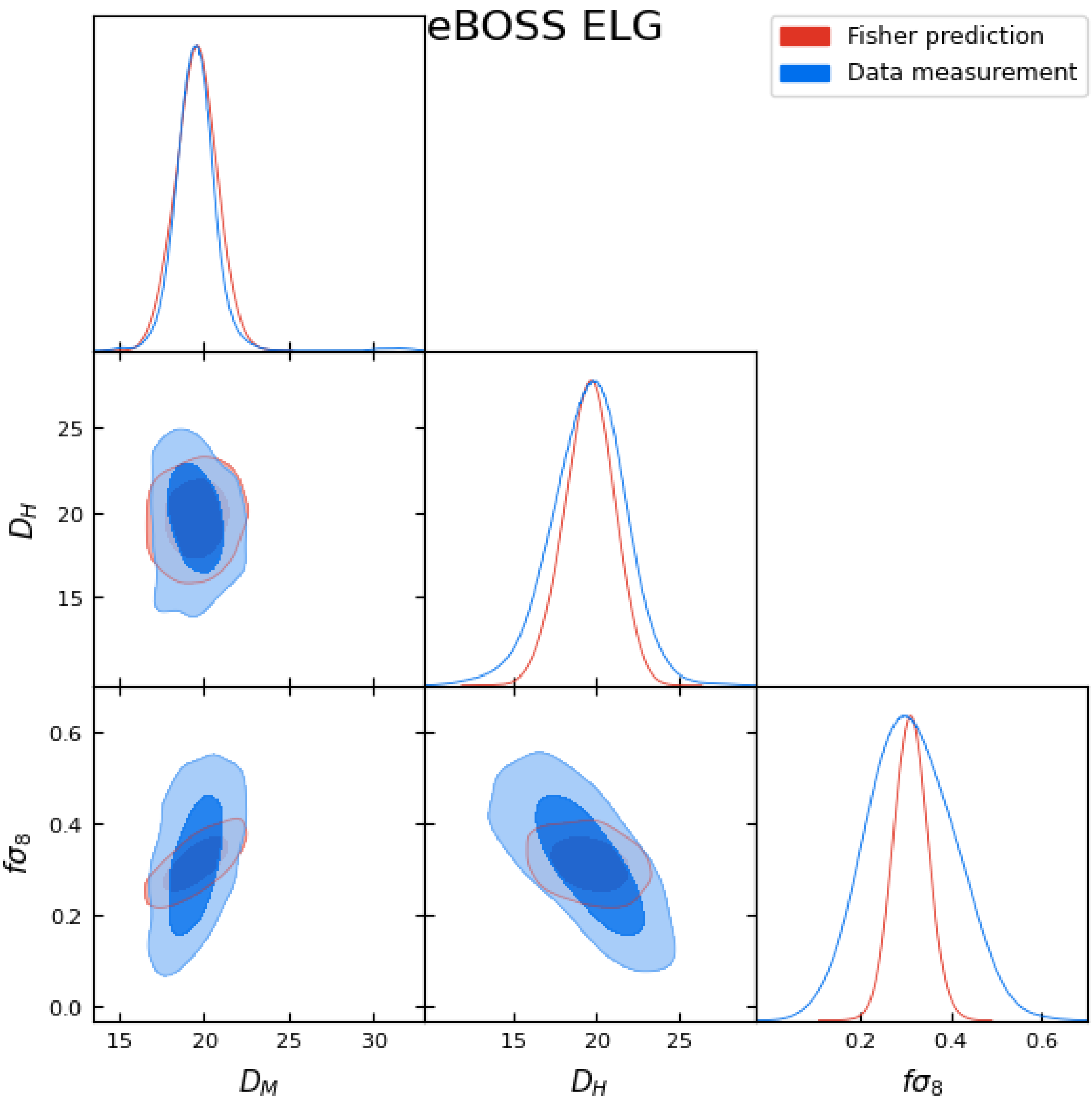

Figure A.7: Constraints on D_M, D_H, $f\sigma_8$. Red contours show 68 and 95 percent confidence regions for the Fisher analysis with $k_{\max} = 0.09\,h\,\mathrm{Mpc}^{-1}$ (this work), and the blue contours show confidence regions for eBOSS ELG sample [116]. Unlike other surveys, data and Fisher do not match very well in eBOSS ELG contour, as for this survey, we found that $k_{\max}^{\mathrm{match}} = 0.06\,h\,\mathrm{Mpc}^{-1}$, which is far from the average value: $k_{\max} = 0.09\,h\,\mathrm{Mpc}^{-1}$. For data, the grid of the relative probability has been used instead of the covariance matrix, as the ELG likelihood is not well-approximated as a Gaussian distribution.

Appendix B

Deriving the interloper-target cross-correlation from target-target auto-correlation

Assume that $\vec{x}$ is the observed comoving distance: for galaxies, this is the same as their true position, whereas, for interlopers, it is the wrong measured position. If the true position of interlopers is $\vec{y}$, then,

$$\vec{x} = \vec{y} - \vec{\Delta d} \tag{B.1}$$

We can write the correlation function between galaxies and interlopers at their observed distances in the Fourier space to further support Eq. 3.6

$$\begin{aligned}
&\xi_{\rm gi}(\vec{x_1} - \vec{x_2}) = \langle \delta_{\rm g}(\vec{x}_1)\delta_{\rm i}(\vec{x}_2)\rangle = \\
&\int \frac{d\vec{k}_1^3}{(2\pi)^3}\frac{d\vec{k}_2^3}{(2\pi)^3} e^{-i\vec{k}_1.\vec{x}_1} e^{-i\vec{k}_2.\vec{x}_2} \langle \delta_{\rm g}(\vec{k}_1)\delta_{\rm i}(\vec{q}_2(\vec{k}_2))\rangle = \\
&\frac{1}{\gamma_\perp^2\gamma_\parallel}\int \frac{d\vec{k}_1^3}{(2\pi)^3}\frac{d\vec{q}_2^3}{(2\pi)^3} e^{-i\vec{k}_1.\vec{x}_1} e^{-i\vec{q}_2.\vec{y}_2} \langle \delta_{\rm g}(\vec{k}_1)\delta_{\rm i}(\vec{q}_2)\rangle = \\
&\frac{1}{\gamma_\perp^2\gamma_\parallel}\int \frac{d\vec{k}_1^3}{(2\pi)^3}\frac{d\vec{q}_2^3}{(2\pi)^3} e^{-i\vec{k}_1.\vec{x}_1} e^{-i\vec{q}_2.\vec{y}_2} \gamma_\perp^2\gamma_\parallel P(k_1)\delta_D(\vec{q}_2 - \vec{k}_1) = \\
&\int \frac{d\vec{k}_1^3}{(2\pi)^3} e^{-i\vec{k}_1.(\vec{x}_1 - \vec{y}_2)} P(k_1) \\
&\xi_{\rm gi}(\vec{x_1} - \vec{y_2})\,.
\end{aligned} \tag{B.2}$$

Appendix C

Repeating the contaminated correlation function fitting in real space

In Fig. C.1 we show the results of our analysis of Chapter 3 in configuration space. The only difference between the redshift space and configuration space analysis is that the correlation function template does not include Kaiser and FOG. We find that our conclusions remain unchanged.

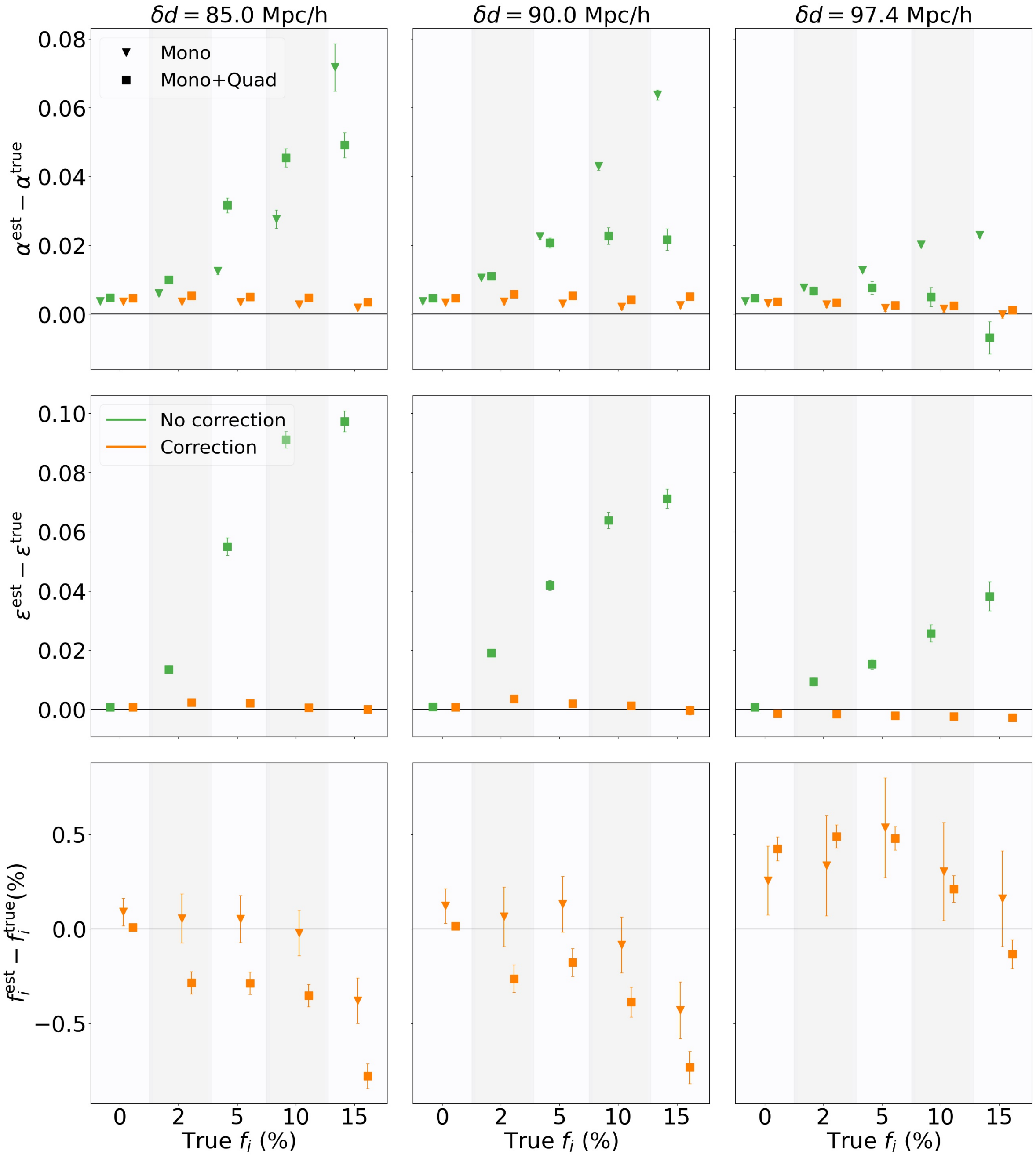

Figure C.1: Same as Figure 3.5, but in real space instead of redshift space.

Appendix D

Comparing the contaminated correlation function model with measurements

We have quantitatively presented the best-fit parameters in the text and interpreted the results (i.e., figure 3.5, section 3.6). In this appendix, I will present how the estimated moments of the correlation function compare with the data when we plug in the best-fit parameters from our MCMC code into our model. I selected the three following cases that are representative of all the cases we have considered in figure 3.5:

- Figure D.1: Uncontaminated, or $f_{\mathrm{i}} = 0$.
- Figure D.2: Catalogue contaminated by 15% interlopers, displaced by $\Delta d = 85\,h^{-1}$ Mpc.
- Figure D.3: Catalogue contaminated by 15% interlopers, displaced by $\Delta d = 97.5\,h^{-1}$ Mpc.

These figures illustrate how our model for the monopole and quadrupole is consistent with the data, regardless of the displacement or the fraction of interlopers.

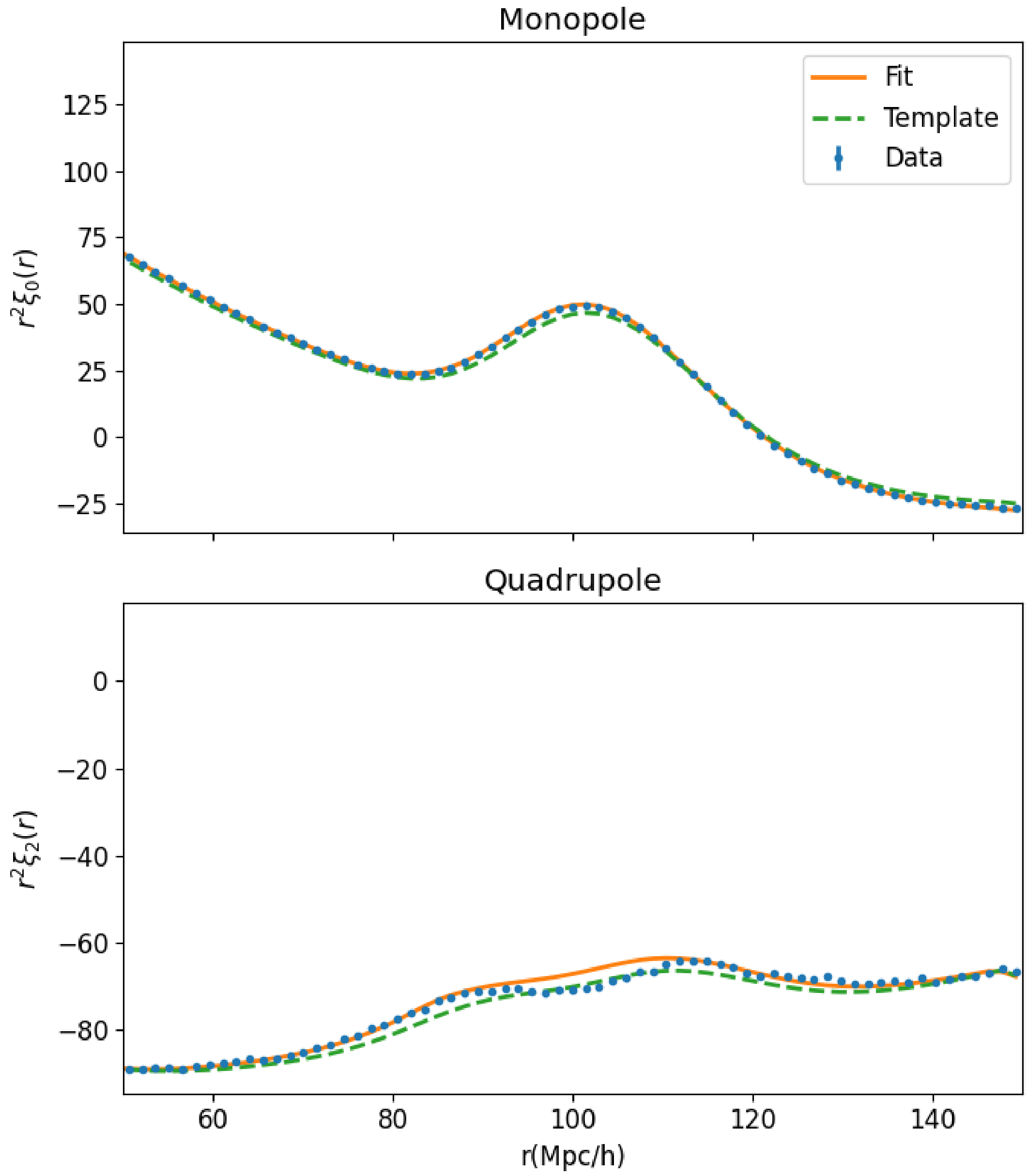

Figure D.1: The mean of 1000 uncontaminated mocks is shown with blue circles. The best-fit is shown in orange, and the template from CAMB linear is shown with dashed green line.

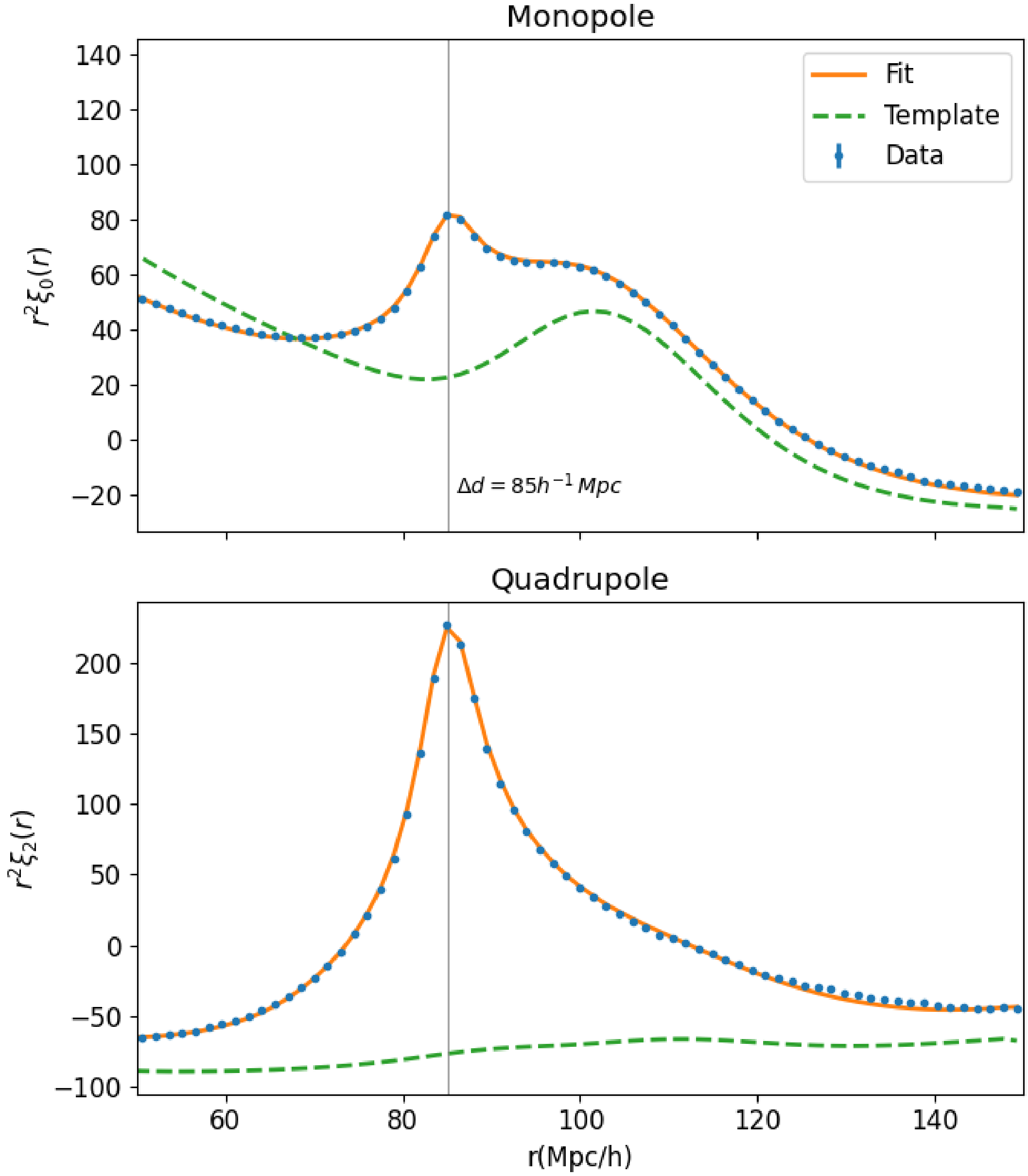

Figure D.2: The mean of 1000 mocks contaminated by 15% interlopers with a displacement of 85 h^{-1} Mpc is shown with blue circles. The best fit is shown in orange, and the template from CAMB linear is shown with a dashed green line.

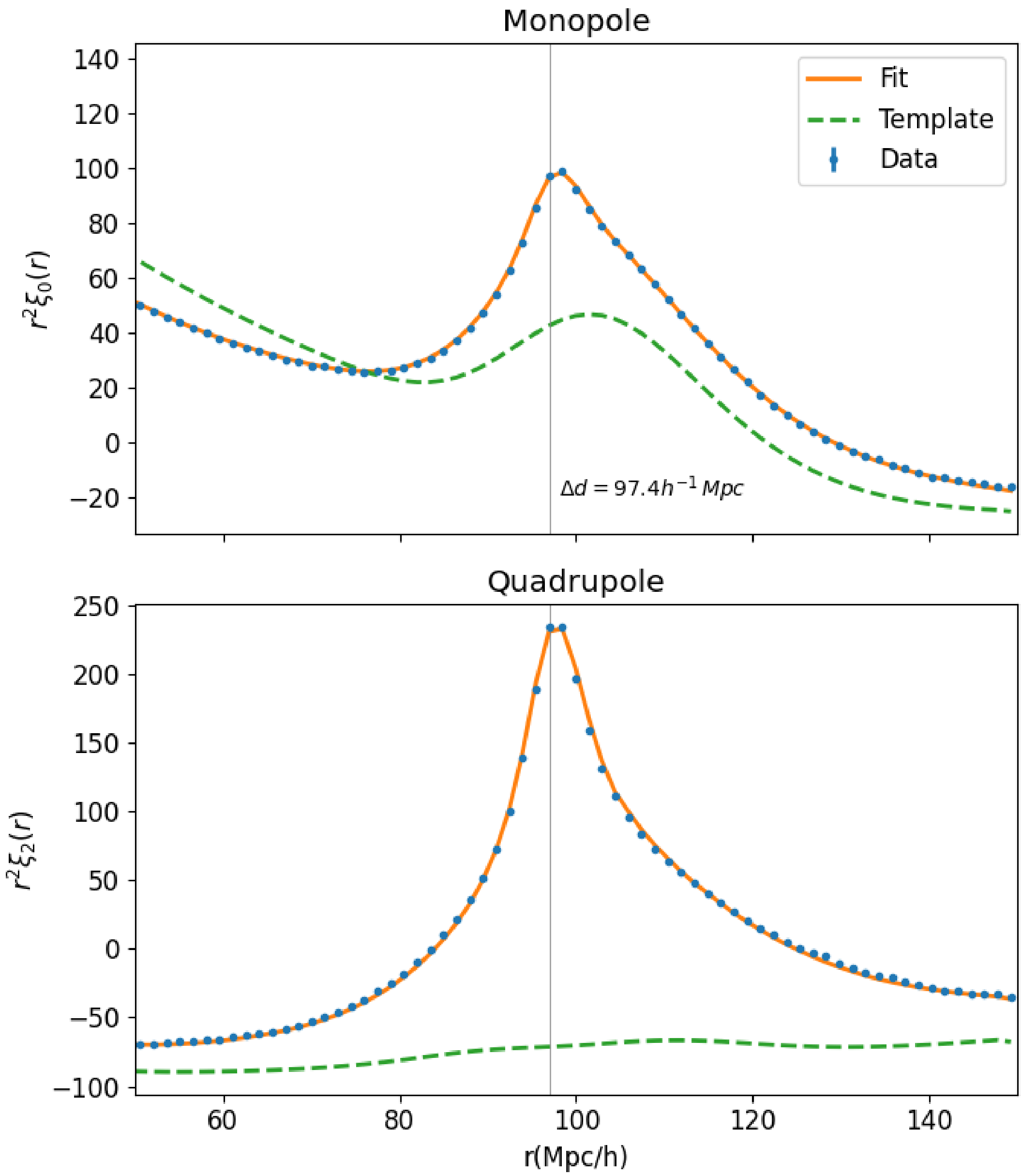

Figure D.3: Same as D.2, but the displacement is $97.4\,h^{-1}$ Mpc.